TURUN
YLIOPISTO
UNIVERSITY
OF TURKU

A NOVEL CONCEPT OF NON-METALLIC ORTHOPEDIC IMPLANTS FOR LOAD-BEARING APPLICATIONS

Artem Plyusnin

TURUN YLIOPISTON JULKAISUJA – ANNALES UNIVERSITATIS TURKUENSIS
SARJA – SER. D OSA – TOM. 1654 | MEDICA – ODONTOLOGICA | TURKU 2022

TURUN
YLIOPISTO
UNIVERSITY
OF TURKU

A NOVEL CONCEPT OF NON-METALLIC ORTHOPEDIC IMPLANTS FOR LOAD-BEARING APPLICATIONS

Artem Plyusnin

TURUN YLIOPISTON JULKAISUJA – ANNALES UNIVERSITATIS TURKUENSIS
SARJA – SER. D OSA – TOM. 1654 | MEDICA – ODONTOLOGICA | TURKU 2022

University of Turku

Faculty of Medicine
Institute of Dentistry, Biomaterials Science
Doctoral Programme in Clinical Research
Turku Clinical Biomaterials Centre
Biomaterials and Medical Device Research Program

Supervised by

PhD, Docent (Adjunct Professor),
Niko Moritz
Department of Biomaterials Science and
Turku Clinical Biomaterials Centre
Faculty of Medicine
University of Turku
Finland

PhD, DDS, Julia Kulkova
Department of Biomaterials Science and
Turku Clinical Biomaterials Centre
Faculty of Medicine
University of Turku
Finland

Reviewed by

Professor (Biomaterials and tissue
engineering), Jonathan Massera
Faculty of Medicine and
Health Technology
Tampere University
Finland

Associate Professor, Gianluca Turco
Department of Medicine
Surgery and Health Sciences
University of Trieste
Italy

Opponent

Adjunct Professor (Biomaterials
Science), Ilkka Kangasniemi
University of Turku
Finland

ISBN 978-951-29-8951-5 (Print)
ISBN 978-951-29-8952-2 (PDF)
ISSN 0355-9483 (Print)
ISSN 2343-3213 (Online)
Painosalama, Turku, Finland 2022

UNIVERSITY OF TURKU
Faculty of Medicine
Institute of Dentistry, Biomaterials Science
Turku Clinical Biomaterials Centre
Biomaterials and Medical Device Research Program
ARTEM PLYUSNIN: A novel concept of non-metallic orthopedic implants for load-bearing applications
Doctoral Dissertation, 270 pp.
Doctoral Programme in Clinical Research
August 2022

ABSTRACT

Metallic implants have remained the state of the art for skeletal reconstruction for over a hundred years. However, the excessive stiffness of metallic implants can lead to unphysiological direct bone healing and bone resorption in both humans and animals. Fiber reinforced composites (FRC) were proposed as alternative to metals in the "less rigid fixation" concept and were successfully approved in animal models and in clinical trials in humans as early as in 1970th and 1980th. However, the use of FRC implants is still limited due to such drawbacks as the lack of contourability, which is desirable in many applications, and high manufacturing costs.

The present dissertation addresses the limitations of FRC implants and suggests a novel concept of non-metallic load-bearing implants. The research further develops the "less rigid fixation" concept and complements it with the application of modern additive manufacturing and composite technologies, such as 3D printing and tailored fiber placement (TFP). The novel concept assumes that the design of the implants does not simply copy the existing conventional metallic counterparts but is initially aimed at the specified fabrication methods to reduce the costs and improve the tailorability and scalability for different clinical conditions and patients. The concept allows application of both biostable and bioresorbable polymeric materials, can be implemented in various designs and can be combined with bioactive agents to stimulate bone growth and decrease the rate of complications related to infections.

The dissertation includes four multidisciplinary studies in which the concept was described, and the basic aspects of that were investigated. Two different clinical problems, frequently occurred in veterinary practice, were addressed. Two prototype designs, an FRC fracture fixation plate, made by TFP and intended for the treatment of antebrachial fractures in toy-breed dogs, and a 3D-printed bioresorbable bioactive tibial tuberosity advancement implant for the treatment of cranial cruciate ligament disease in large dogs, were proposed based on the findings of the research. It is expected that the novel implants can improve the ossification and decrease the complications rate in animals. In addition, the present research serves as the first step towards the anticipated implementation of the novel concept in implants for humans.

KEYWORDS: fiber reinforced composites, bioactive glass, bioresorbable polymers, less rigid fixation, mechanical testing, fracture fixation, tibial tuberosity advancement

TURUN YLIOPISTO
Lääketieteellinen tiedekunta
Hammaslääketieteen laitos, Biomateriaalitiede
Biomateriaalitutkimusohjelma, Turun kliininen biomateriaalikeskus
ARTEM PLYUSNIN: Uudenlainen konsepti metallittomiksi ortopedisiksi implanteiksi kuormaa kantaviin sovelluksiin
Väitöskirja, 270 s.
Turun kliininen tohtoriohjelma
Elokuu 2022

TIIVISTELMÄ

Luuston korjauksessa on yli sadan vuoden ajan käytetty pääosin metallisia implantteja. Niiden jäykkyys voi kuitenkin johtaa epäfysiologiseen suoraan luunmuodostukseen ja luun resorptioon sekä ihmisillä että eläimillä. Kuitulujitettuja komposiittimateriaaleja (fiber reinforced composite, FRC) on 1970- ja 1980-luvuilta lähtien onnistuneesti kokeiltu eläinkokeissa ja kliinisissä kokeissa vähemmän jäykkänä vaihtoehtona metalleille. FRC-implanttien käyttö on toistaiseksi ollut rajallista, sillä valmistuksen jälkeen ne eivät ole muovattavissa, mikä olisi suotava ominaisuus monessa käytännön sovellutuksessa, ja niiden valmistus on kallista.

Tässä väitöskirjassa paneudutaan FRC-implanttien puutteisiin ja ehdotetaan uudenlaista konseptia metallittomiksi kuormaa kantaviksi implanteiksi. Tutkimuksessa kehitettiin vähemmän jäykkää luufiksaatiota moderneilla 3D-tulostus- ja räätälöity kuitusijoitus (tailored fiber placement, TFP) -tekniikoilla. Implantit on varta vasten valituille valmistustekniikoille suunniteltu, eivätkä pelkkiä kopioita metallisista vastineistaan. Tarkoituksena on vähentää valmistuksen kustannuksia ja parantaa implanttien muokattavuutta erilaisia kliinisiä tilanteita ja potilaita varten. Konsepti mahdollistaa sekä biohajoavien että biohajoamattomien implanttien valmistuksen eri muodoissa, ja siihen voidaan yhdistää bioaktiivisia yhdisteitä stimuloimaan luun kasvua ja vähentämään infektioista johtuvia komplikaatioita.

Väitöskirjan neljässä poikkitieteellisessä osatyössä konsepti kuvaillaan ja sen perusominaisuuksia tutkitaan. Implanttiprototyypit kehitettiin kahteen yleiseen eläinlääketieteelliseen kliiniseen ongelmaan: TFP-tekniikalla valmistettu FRC-fiksaatiolevy radiuksen ja ulnan murtumien hoitoon pienikokoisilla koirilla, ja isojen koirien polven eturistisidevaurioiden hoitoon tarkoitettu 3D-tulostettu bioaktiivinen ja bioresorboituva implantti sääriluun kyhmyn eteenpäin siirtämiseksi. Oletuksena on, että implantit parantavat luutumista ja vähentävät komplikaatioriskiä eläimillä. Lisäksi tämä tutkimus on ensimmäinen askel tämän uudenlaisen konseptin käyttöön ihmisillä.

AVAINSANAT: kuitulujitteiset komposiitit, bioaktiivinen lasi, bioresorboituvat polymeerit, vähemmän jäykkä fiksaatio, mekaaninen testaus, luunmurtumien hoito, sääriluun kyhmyn eteenpäin siirto

Table of Contents

Abbreviations **10**

List of Original Publications **12**

1 Introduction **13**

2 Review of the Literature **16**
2.1 Bone 16
2.1.1 Structure of bone 16
2.1.1.1 Bone composition 16
2.1.1.2 Bone tissue morphology and types 17
2.1.1.3 Bone cells 18
2.1.2 Healing patterns 19
2.2 Skeletal reconstructive biomaterials 21
2.2.1 Classification 21
2.2.2 Non-metallic skeletal reconstructive biomaterials 23
2.2.2.1 Biostable polymers 23
2.2.2.2 Bioresorbable polymers 25
2.2.2.3 Bioactive ceramics 28
2.2.2.4 Polymer-based composites 30
2.2.3 Clinical applications 32
2.3 Additive manufacturing 33
2.3.1 Tailored fiber placement 35
2.4 Experimental methods for characterization of skeletal reconstructive biomaterials 36
2.4.1 Animal models in orthopedic research 36
2.4.2 Methods of quantitative characterization of bone formation 38
2.4.2.1 Histomorphometry 38
2.4.2.2 Micro-CT 39
2.4.3 Mechanical testing of biomaterials for load-bearing applications 41
2.4.4 Finite element analysis 42
2.4.5 Instrumental methods of physical and chemical characterization of biomaterials 44

3 Aims **47**

4 Materials and Methods **48**

4.1 Clinical concept of the *in situ* contourable FRC fracture fixation plate (Studies I – III) ... 48
4.2 Study I ... 49
4.2.1 Stage 1 ... 50
4.2.1.1 Preparation of FRC specimens ... 50
4.2.1.2 Three-point bending test of FRC specimens ... 51
4.2.1.3 Modeling of the three-point bending test by FEA ... 52
4.2.2 Stage 2 ... 54
4.2.2.1 Preparation of FRC fracture fixation plates ... 54
4.2.2.2 Four-point bending test of fracture fixation plates ... 54
4.2.2.3 Modeling of the four-point bending test by FEA ... 55
4.2.2.4 Analysis of predicted and experimental results ... 55
4.2.2.5 Analysis of the effect of plate thickness and curvature on the stiffness ... 56
4.3 Study II ... 56
4.3.1 Stage 1 ... 57
4.3.1.1 Preparation of oligomer mixtures ... 57
4.3.1.2 Preparation of light-curable resins ... 57
4.3.1.3 Light curing protocol ... 57
4.3.1.4 Measurement of the degree of conversion ... 58
4.3.2 Stage 2 ... 59
4.3.2.1 Preparation of specimens for tensile test ... 59
4.3.2.2 Tensile test ... 59
4.3.2.3 Thermomechanical analysis ... 60
4.3.3 Stage 3 ... 61
4.3.3.1 Preparations ... 61
4.3.3.2 Dissolution test ... 61
4.3.3.3 Three-point bending test ... 61
4.3.4 Stage 4 ... 61
4.3.4.1 Preparation of specimens ... 61
4.3.4.2 Preparation of cells ... 62
4.3.4.3 Cell morphology test ... 63
4.3.4.4 Cell proliferation test ... 64
4.4 Study III ... 64
4.4.1 Stage 1 ... 64
4.4.1.1 Preparation of specimens ... 64
4.4.1.2 Three-point bending test ... 65
4.4.2 Stage 2 ... 66
4.4.2.1 Spatial optimization of the TFP reinforcement pattern ... 66
4.4.2.2 Preparation of plates ... 67
4.4.2.3 Preparation of bone specimens ... 68
4.4.2.4 Four-point bending test of plates ... 68
4.4.2.5 Four-point bending test of bone specimens ... 69
4.4.2.6 Torsional test of bone specimens ... 69

4.5 Clinical concept of the bioactive bioresorbable TTA implant (Study IV) 70
4.6 Study IV 71
4.6.1 Stage 1 72
4.6.1.1 Preparations 72
4.6.1.2 SBF immersion test 72
4.6.1.3 Analysis of ion concentrations in SBF 73
4.6.1.4 Analysis of CaP formation 73
4.6.2 Stage 2 74
4.6.2.1 Preparation of specimens and materials 74
4.6.2.2 Dissolution test 74
4.6.2.3 Compression test 75
4.6.2.4 Modeling of the compression test by FEA 75
4.6.2.5 Modeling of TTA implants by FEA 75
4.6.3 Stage 3 75
4.6.3.1 Preparation of the experimental implants 75
4.6.3.2 Dissolution test 75
4.6.3.3 Preparation of the control titanium implants 76
4.6.3.4 *In vivo* biocompatibility and osteointegration tests 76
4.6.3.5 Micro-CT analysis of rabbit femora 76
4.6.3.6 Histological analysis of rabbit femora 77
4.7 Statistical methods used in the research 77

5 Results 78
5.1 Study I 78
5.1.1 Stage 1 78
5.1.1.1 Three-point bending test of FRC specimens 78
5.1.1.2 Modeling of the three-point bending test by FEA 79
5.1.2 Stage 2 80
5.1.2.1 Four-point bending test of fracture fixation plates 80
5.1.2.2 Modeling of the four-point bending test by FEA 82
5.1.2.3 Analysis of the effect of plate thickness and curvature on the stiffness 83
5.2 Study II 84
5.2.1 Stage 1 84
5.2.1.1 Visual description of the synthesized polymers 84
5.2.1.2 FTIR and ^{1}H-NMR spectra of PLAMA 84
5.2.1.3 Degree of conversion 85
5.2.2 Stage 2 86
5.2.2.1 Tensile test 86
5.2.2.2 Thermomechanical analysis 88
5.2.3 Stage 3 89
5.2.3.1 Dissolution test 89
5.2.3.2 Three-point bending test 91
5.2.4 Stage 4 92

5.2.4.1 Cell morphology test 92
5.2.4.2 Cell proliferation test 93
5.3 Study III 96
5.3.1 Stage 1 96
5.3.1.1 Three-point bending test 96
5.3.2 Stage 2 97
5.3.2.1 Four-point bending test of plates 97
5.3.2.2 Four-point bending test of bone specimens .. 99
5.3.2.3 Torsional test of bone specimens 100
5.4 Study IV 102
5.4.1 Stage 1 102
5.4.1.1 Ion concentrations in SBF 102
5.4.1.2 CaP formation 103
5.4.2 Stage 2 104
5.4.2.1 Dissolution test 104
5.4.2.2 Compression test 104
5.4.2.3 Modeling of compression test by FEA 104
5.4.2.4 Modeling of TTA implants by FEA 105
5.4.3 Stage 3 105
5.4.3.1 Dissolution test 105
5.4.3.2 General results of the *in vivo* experiment 105
5.4.3.3 Micro-CT analysis of rabbit femora 105
5.4.3.4 Histological analysis of rabbit femora 107

6 Discussion 109
6.1 Study I 109
6.2 Study II 114
6.3 Study III 117
6.4 Study IV 121

7 Conclusions 124

Acknowledgements 125

References 127

Original Publications 147

Abbreviations

3D	three-dimensional
^{1}H-NMR	proton nuclear magnetic resonance
AM	additive manufacturing
ANOVA	analysis of variance
AW	apatite-wollastonite
BEI	back-scattered electron imaging
BCP	biphasic calcium phosphate
BG	bioactive glass
bisGMA	bisphenol-A-glycidyl methacrylate
CAD	computer-aided design
CaP	calcium phosphate
CFR	carbon-fiber reinforced
CNC	computer numerical control
CNT	carbon nanotube
CrCL	cranial cruciate ligament
CS	coordinate system
CTE	coefficient of thermal expansion
CQ	camphorquinone
DC	degree of conversion
DCP	dicalcium phosphate
DL	deep learning
DMAEMA	2-dimethylaminoethyl methacrylate
ECM	extracellular matrix
EDTA	ethylenediaminetetraacetic acid
FDM	fused deposition modeling
FE	finite element
FEA	finite element analysis
FG	flat glass
FRC	fiber-reinforced composite
FTIR	Fourier-transform infrared spectroscopy
GC	glass-ceramic

GFR	glass-fiber reinforced
HA	hydroxyapatite
HE	hematoxylin and eosin
IM	intramedullary
IR	infrared
micro-CT	micro-computed tomography
MMA	methyl methacrylate
N/A	not applicable
N/D	no data
PBS	phosphate buffered saline
PC	polycarbonate
PCL	polycaprolactone
PDLGA	poly (DL-lactide-co-glycolide)
PDXO	polydioxanone
PE	polyethylene
PEEK	polyether etherketone
PGA	polyglycolide
PGLA	poly (glycolide-co-lactide)
PLA	polylactide
PLAMA	polylactic acid functionalized with dimethacrylate
PLDL	poly (LL-/DL-) lactide
PMMA	polymethyl methacrylate
PP	polypropylene
PPP	porous poly(para-phenylene)
PTFE	polytetrafluoroethylene
ROI	region of interest
RT	room temperature
SBF	simulated body fluid
SD	standard deviation
SLA	stereolithography
SLS	selective laser sintering
TCP	tricalcium phosphate
TEGDMA	triethylene glycol dimethacrylate
TFP	tailored fiber placement
TMA	thermomechanical analysis
TTA	tibial tuberosity advancement
UHMWPE	ultra-high-molecular-weight polyethylene
UTS	ultimate tensile strength
VK	von Kossa
VOI	volume of interest

List of Original Publications

This dissertation is based on the following original publications, which are referred to in the text by their Roman numerals:

I Liesmäki O.*, Plyusnin A.*, Kulkova J., Lassila L.V.J., Vallittu P.K., Moritz N. (* equal contribution). Biostable glass fibre-reinforced dimethacrylate-based composites as potential candidates for fracture fixation plates in toy-breed dogs: mechanical testing and finite element analysis. *Journal of the Mechanical Behavior of Biomedical Materials*, 2019; 96: 172 – 185.

II Plyusnin A., He J., Elschner C., Nakamura M., Kulkova J., Spickenheuer A., Scheffler C., Lassila L., Moritz N. A polymer for application as a matrix phase in a concept of in situ curable bioresorbable bioactive load-bearing continuous fiber reinforced composite fracture fixation plates. *Molecules*, 2021; 26: 1256.

III Moritz N., Liesmäki O., Plyusnin A., Keränen P., Kulkova J. Load-bearing composite fracture-fixation devices with tailored fibre placement for the treatment of antebrachial fractures in toy-breed dogs. *Manuscript.*

IV Plyusnin A., Kulkova J., Arthurs G., Jalava N., Uppstu P., Moritz N. Biological Response to an Experimental Implant for Tibial Tuberosity Advancement in Dogs: A Pre-Clinical Study. *Research in Veterinary Science*, 2020; 128: 183 – 196.

1 Introduction

Metals are one of the main groups of construction materials in many fields of human activity due to their exceptional strength. In medicine metallic implants have remained the state of the art for skeletal reconstruction for over a hundred years (Uhthoff et al., 2006). However, the high mechanical properties of metals counterintuitevily determine the disadvantages of metals for orthopedic applications. The stiffness and strength of metallic implants are significantly higher than those of bone, which results in undesirable redistribution of the loads between the implant and the underlying bone called “stress-shielding”. In turn, this can lead to osteopenia in the treated bone (Akeson et al., 1975; Uhthoff et al., 2006; Uhthoff and Dubuc, 1971). Moreover, when using rigid metallic implants, there takes place direct bone healing instead of more natural indirect healing by formation of callus (McKibbin, 1978; Tayton et al., 1982). Direct healing takes sufficient time and can end up with reoccurred fracture after plate removal (Becker et al., 2012; Uhthoff et al., 2006).

A concept of “less-rigid” fixation was proposed to reduce the outlined adverse effects (Akeson et al., 1976, 1975; McKibbin, 1978; Tayton and Bradley, 1983; Woo et al., 1983). It assumed that for successful fracture healing, a fixation device should, on the device level, have stiffness comparable to the stiffness of a bone. This would provide adequate stability and simultaneously allow for some amount of micromotions in the fracture site to promote natural ossification. Two main directions to reduce the overall stiffness of the fixation implant were suggested: 1. to reduce the cross-section of a device for instance by making it hollow, or 2. to use less stiff materials, such as FRC (Woo et al., 1983). Apparently, the clinical demand in less-rigid fixation is especially emphasized in the patient groups having decreased mineral density in bones, such as elderly people (Hollevoet et al., 2011; Hollevoet and Verdonk, 2003; Pemberton et al., 1994), or in pediatric and adolescent patients with immature skeleton (Kelly et al., 2013; May et al., 2013; Osborn et al., 2018). In the veterinary practice, small pets are more prone to stress-shielding and consequent osteopenia (Harasen, 2003; Manchi et al., 2017; Piras et al., 2011).

Since the time when less-rigid fixation concept was described, the proof of concept for FRC devices for musculoskeletal reconstruction has been successfully established for carbon-fibers reinforced epoxy or PEEK-based (Pemberton et al.,

1994; Tayton et al., 1982) and, in a later period, glass-fiber reinforced acrylic-based (Aitasalo et al., 2014; Moritz et al., 2014; Piitulainen et al., 2017, 2015; Tuusa et al., 2008, 2007; Vallittu, 2017; Zhao et al., 2009) composites in both animal models and clinical applications in humans. In general, FRC showed a good biocompatibility, tailorability in terms of structural mechanical properties and promising bone healing rate. The strength of composite implants reinforced with continuous fibers can achieve comparable values to their metallic counterparts, while fatigue resistance can be even higher than in metals (Evans and Gregson, 1998; Scholz et al., 2011). In addition, use of radiolucent non-metallic FRC implants is beneficial from the point of the follow-up imaging or radiotherapy (Boriani et al., 2018; Laux et al., 2018). However, a fundamental obstacle for wider clinical applications of FRC with continuous fibers is the lack of contourability of such devices (Boriani et al., 2018; Laux et al., 2018; Pemberton et al., 1994) which is, on the contrary, the great advantage of metals due to their ductility (Lin et al., 2016).

The present dissertation addresses the outlined limitations of state-of-the-art FRC implants and suggests a complex solution, a novel concept of non-metallic load-bearing implants. The concept further develops the idea of the "less rigid fixation" and complements it with the application of modern additive manufacturing and composite technologies, such as three-dimensional (3D) printing and tailored fiber placement [TFP; (Mattheij et al., 1998)]. These technologies allow for creation of mechanically and spatially optimized structures, provide high degree of automation, customization and tailorability and minimize the production costs and wastes.

The novel concept assumes that the design of the implants does not simply copy the existing conventional metallic counterparts but is initially aimed at the specified fabrication methods to reduce the costs and improve the tailorability and scalability for different clinical conditions and patients. The concept allows for application of both biostable and bioresorbable polymeric materials, can be implemented in various designs and can be combined with bioactive agents to stimulate bone growth and to decrease the rate of complications related to infections. In the fully bioresorbable implementation, the proposed implants are expected to allow for gradual rearrangement of loads from the implant back to the underlying bone, while the material of the implant is dissolved, and the fractured bone is healed. Moreover, it is expected that the products of the implant dissolution would be eventually excreted from the body, thus eliminating the need for an additional surgery to remove the implant after healing of the bone.

The dissertation includes four multidisciplinary studies in which the concept was described, and the basic aspects of that were investigated. Two different clinical problems, frequently occurred in veterinary practice, were addressed to propose, on one hand, novel solutions for the treatment of those problems and to be considered as a part of pre-clinical investigations on the way towards applications of the novel

concept in humans, on the other hand. Thus, the research resulted in the designs of two prototype implants. The first one was the prototype of the *in situ* contourable FRC fracture fixation plate for the treatment of antebrachial fractures in toy-breed dogs. In these animals, having the body weight below 5 kg, the frequency of that type of fractures and the risk of related complications is exceptionally high (Harasen, 2003; Manchi et al., 2017; Piras et al., 2011). In humans, plates of similar design and size can be used, for instance, in maxillofacial reconstruction. The second prototype implant design was the 3D-printed bioresorbable bioactive tibial tuberosity advancement (TTA) implant for the treatment of cranial cruciate ligament disease. This pathological condition is more typical for medium-to-large breeds of dogs (Hayashi et al., 2004; Johnson et al., 1994). In humans, similar devices could be further developed to a bioactive implant for filling large bone defects. In addition, it is expected that a combination of the proposed plate and implant for filling bone defect could be used in both animals and humans.

2 Review of the Literature

2.1 Bone

2.1.1 Structure of bone

Bone, or osseous tissue is a type of specialized connective tissue which plays a vital role in biomechanics and metabolism of vertebrate animals. Bone is often referred to as a natural nanocomposite material consisting of the organic protein phase and inorganic mineral phase. In turn, the composite phases include minerals, collagen, bone cells, water, noncollagenous proteins, lipids, blood vessels and nerves (Cowin, 2001; Meskinfam, 2017). Bone is the main constituent forming a skeleton and thus determines the body shape, mechanically protects inner organs and provides mobility. These functions, in turn, determine the unique structure of bone tissues providing highly efficient strength-to-mass ratio; at the same time the bone density, along with mechanical properties, depends on the concrete location in the body and specific loads occurring there (Frost, 2003). In case of injury, the bone tissue possesses the unique capabilities of self-regenerating or self-remodeling almost to its initial condition; these capabilities retain to some extent throughout the all lifetime of the organism (McKibbin, 1978). Bone has an important role in the turnover of Ca and P ions in the organism (Meskinfam, 2017).

2.1.1.1 Bone composition

As a composite structure, the bone comprises the organic phase (~30…35 % of bone mass) and the mineral phase (~65…70 %), as well as cells and water (Cowin, 2001; Poitout, 2016).

The organic phase comprises collagen (~90 %) in form of fibers. The other 10 % consist of diverse noncollagenous proteins, including osteocalcin, osteonectin, osteopontin, and bone sialoprotein (Cowin, 2001).

The mineral phase predominantly comprises hydroxyapatite (HA), $Ca_{10}(PO_4)_6(OH)_2$. The crystals of HA in forms of needles, plates and rods are embedded in the organic part of the bone by bonding to the collagen fibers (Cowin, 2001; Meskinfam, 2017). Other minerals are incorporated into the lattice of HA

crystals or absorbed onto their surface. The crystals of HA are the vital component providing the exceptional mechanical properties of the bone (Cowin, 2001).

2.1.1.2 Bone tissue morphology and types

Morphologically, bone tissue is divided into two main types – cortical, or compact bone, or cortex (~80 % of skeletal mass) and trabecular, or cancellous, or spongy bone (~20 % of skeletal mass) (Cowin, 2001). A long bone, such as tibia or femur, is a hollow cylinder, called shaft or diaphysis, with rounded ends (epiphyses) having slightly larger diameter than the diaphysis. The epiphyses connect to the diaphysis with the conical parts called metaphyses. The diaphysis mostly comprises cortical bone, while the metaphyses and epiphyses consist of trabecular bone covered with a thin layer of cortical bone (Figure 1).

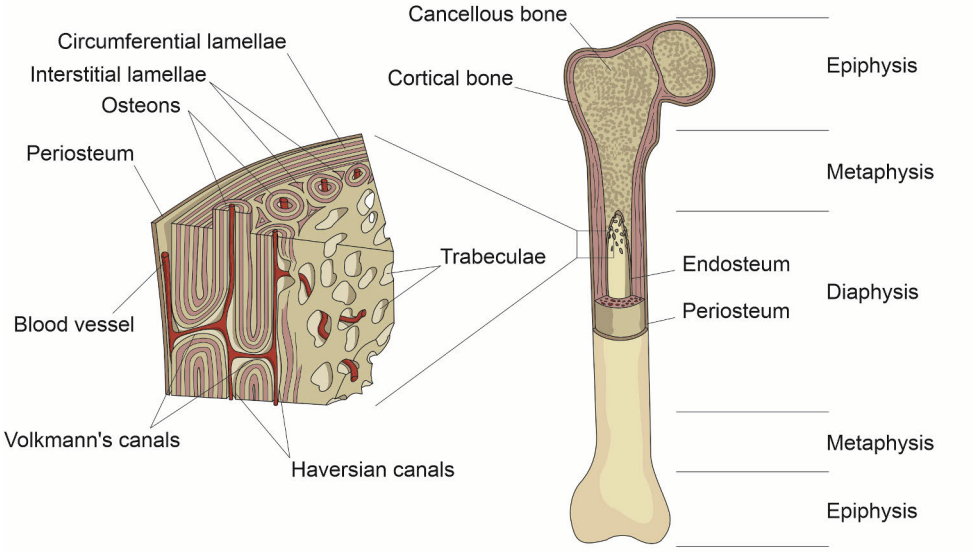

Figure 1. Bone structure. Inspired by: ID 229320955 © VectorMine Dreamstime.com.

The main function of cortical bone is mechanical; it is hard and dense (porosity ~10 %), compared to trabecular bone. In the embryo and early period of organism's life (up to the age of 2…3 years for human) (Cowin, 2001), cortical bone is of woven (primary) type. Woven bone comprises interwoven collagen fibers and randomly distributed osteocytes. Unlike that, lamellar (secondary) bone, which replaces woven bone over time, is a highly organized structure. It consists of unit layers (lamellae) resembling plywood. In turn, a lamella contains unidirectionally oriented collagen fibers, however in adjacent lamellae those directions can differ up to 90 ° (Cowin, 2001). Lamellae usually form one of the three typical structures: an osteon – a

hollow channel (Haversian canal) surrounded by concentric rings of lamellae and containing blood vessels and nerves in its center; circumferential lamellae – concentric lamellae surrounding the whole shaft (cylindrical part) of a long bone; interstitial lamellae – the remainders of former circumferential or concentric lamellae filling the gaps between the osteons. The lamellae in osteons contain small cavities (lacunae) connected by canaliculi. In turn, the Haversian canals are connected by Volkmann's canals, going transversely to them, with the periosteum. Periosteum is a membrane covering the outer surface of bone and comprising a layer of fibrous tissue and an inner layer of undifferentiated cells. It provides blood supply to the bone and forms the bone during the growth or healing of fracture (Cowin, 2001; Meskinfam, 2017). In turn, the inner surface of the hollow diaphysis is covered with endosteum, a membrane of osteoclasts, osteoblasts and bone lining cells (Cowin, 2001).

Trabecular bone is a highly porous (up to 90 %) and more considerably vascularized, compared to cortex, tissue. The structural unit of this type of tissue is a trabecula, formed by hemiosteons or interstitial lamellae. Trabecular bone has significantly lower mechanical properties than cortical bone. It is mostly found in the ends of long bones and contains bone marrow, which plays a key role in the production of blood cells. The porous structure of trabecular bone is aligned with the predominant loads acting in the bone (Cowin, 2001; Meskinfam, 2017).

2.1.1.3 Bone cells

Five main types of cells are distinguished in the cellular component of the bone tissue: osteoblasts, osteocytes, osteoclasts, bone-lining cells and osteoprogenitor cells. The balance between all types of cells is crucial for the healthy bone remodeling.

Osteoblasts and osteocytes play crucial role in the bone formation, remodeling and mineralization. Osteoblasts are differentiated from the precursors found on the periosteum and the endosteum and in the bone marrow (Cowin, 2001). The osteoblasts form the unmineralized bone matrix and can generate osteocytes, while osteocytes have three functions: 1. to maintain the mineral balance; 2. to detect microdamage; 3. to identify and react to the strain distribution in bone thus providing the control over remodeling in response to the loads acting on the bone. Osteocytes are found inside the bone matrix, unlike osteoblasts and osteoclasts (Cowin, 2001; Meskinfam, 2017).

The osteoclasts are the largest of specific bone cells. In bone remodeling, osteoclasts are responsible for resorption of both organic and mineral components of the bone tissue (Cowin, 2001; Meskinfam, 2017). They are usually found in the cavities on the surface of bone (Cowin, 2001).

Bone-lining cells regulate the turnover of minerals in the bone. In addition, they react to hormones which produce specific proteins activating osteoclasts (Meskinfam, 2017). These cells are found on the bone surface (Cowin, 2001).

Osteoprogenitor, or precursor cells are mesenchymal cells, which divide and differentiate into specific bone cells (Cowin, 2001; Meskinfam, 2017).

2.1.2 Healing patterns

At normal conditions, the normal state of the bone is homeostasis, while slow turnover of bone tissues is provided by balanced amounts of osteoblasts and osteoclasts (McKibbin, 1978). If a fracture occurs, it starts a complex mechanism of bone healing. However, different conditions accompanying the bone healing lead to considerable differences in that process (McKibbin, 1978; Woo et al., 1983).

Table 1. Stages of indirect bone healing.

Stage	Description	Duration
Inflammatory stage	Formation of hematoma in the fracture site; the hematoma fills the gap between the bone fragments and serves as a scaffold for cellular and molecular activity	7…10 days
Formation of cartilage (soft callus)	Transition of hematoma to granulation tissue; removal of necrotic bone by osteoclasts; cartilage overlying the fracture gap is being formed by angiogenesis with contributions from periosteum and soft tissues	2…3 weeks
Calcification of soft cartilage (hard callus)	Recruitment of osteoprogenitor cells from periosteum and endosteum; vascularization of calcified tissues; formation of woven bone	3…4 months
Removal of cartilage	Calcified cartilage is being resorbed by chondroclasts; further formation of woven bone which replaces the resorbed cartilage tissue	3…4 months
Bone remodeling	Formation of lamellar bone from woven bone	Months to years

Data combined from (Einhorn, 1998; McKibbin, 1978).

In the intact bone the rate of the tissue turnover depends on the loads, acting on the bone, and the subsequent strains occurring in the tissues (Frost, 2003; Perren, 2002). Normal strain, needed for the balanced bone turnover, is usually reported to be not greater than 2 % (Perren, 2002). The conventional option for the treatment of fractures in the last few decades has been the application of metallic devices (Uhthoff et al., 2006). For instance, in a fracture of a long bone fixed with a metallic plate, the

strains in the fracture site remain within the aforementioned range (Perren, 2002). Moreover, the ends of the bone are often compressed towards each other to eliminate a gap. Thus, the biological and biomechanical conditions remain generally the same as at normal bone homeostasis (Perren, 2002). The healing process occurring in such conditions is usually referred to as direct or primary healing (McKibbin, 1978; Woo et al., 1983). It is characterized by direct growing of osteons at the ends of fractured bone fragments towards each other, which provides pathways for blood vessels in Haversian canals (Einhorn, 1998; McKibbin, 1978). Importantly, the periosteum remains uninvolved in this process (Einhorn, 1998; McKibbin, 1978). In fact, this pattern is rather unnatural for the bone, and often takes significant time, while the bone in the fracture site becomes more fragile (Einhorn, 1998; McKibbin, 1978; Woo et al., 1983).

As opposite to direct healing, indirect or secondary healing is a more natural process, involving several successive stages (Table 1, Figure 2), including tissue differentiation, resorption of the necrotic surfaces of the bone fragments and union of those fragments by formation of callus (McKibbin, 1978; Perren, 2002). The initiation of indirect healing requires higher strains at the fracture site compared to normal bone remodeling [2…5 % (Perren, 2002)]. The advantages of indirect over direct healing in terms of the time frames and better clinical outcomes were well described in the literature in the 70s and 80s (Akeson et al., 1976, 1975; McKibbin, 1978; Tayton et al., 1982; Tayton and Bradley, 1983; Uhthoff and Dubuc, 1971; Woo et al., 1983). In those works, a concept of “less-rigid” internal fixation, stimulating the indirect healing, was proposed and explained. Healing process, observed in those studies, was associated with formation of callus and decreased

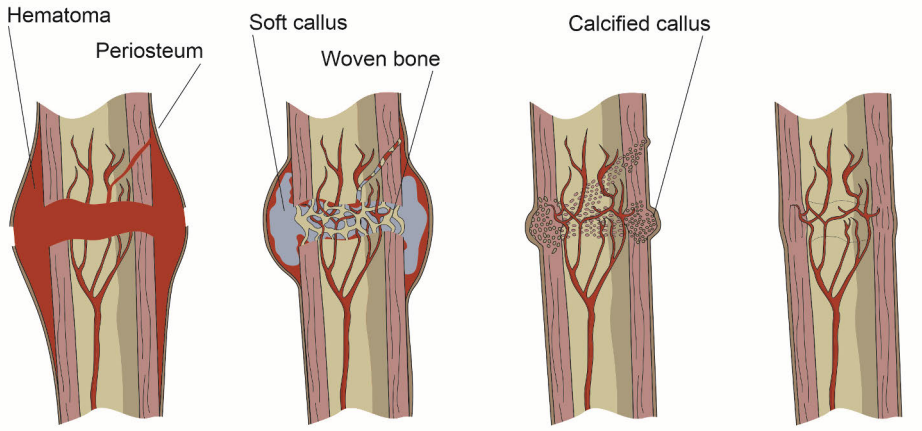

Figure 2. Indirect bone healing from formation of hematoma to bone remodeling (from left to right). Inspired by a figure from: (Pountos and Giannoudis, 2018).

healing time. Indirect bone healing has been reported in multiple studies on the FRC implants (Kettunen et al., 1999a; Pemberton et al., 1994; Tayton et al., 1982).

2.2 Skeletal reconstructive biomaterials

2.2.1 Classification

In general terms, biomaterial is a material that has been engineered to interact with biological systems to treat, augment or replace functions of that systems (Migonney, 2014); consequently, one can derive from that definition that skeletal reconstructive biomaterials serve to treat orthopedic injuries, augment or replace lost or damaged parts of skeleton. All biomaterials have a fundamental property, biocompatibility, which denotes that the biomaterial must not induce any undesirable response from the host biological material (Migonney, 2014; Navarro et al., 2008).

As a separate direction in research, biomaterials have been actively studied since the middle of the 20th century (Migonney, 2014; Navarro et al., 2008). According to Navarro and colleagues, three generations of biomaterials can be distinguished, which, however, are rather conceptual generations than generations in chronological sense (Navarro et al., 2008).

First generation, bioinert or biostable materials – materials which ideally must not elicit any response from the host and should maintain their initial chemical and physical properties, structure and mass during all time of their exploitation (Bandopadhyay et al., 2019; Dumitriu, 2002; Navarro et al., 2008). This generation included all types of materials – metals, ceramics and polymers (Table 2). Bioinert composites based on those materials, like epoxy or PEEK reinforced with carbon fibers, are also referred to as biomaterials of the first generation (Navarro et al., 2008).

Second generation is represented by bioresorbable and bioactive materials (Table 2). As opposite to bioinert ones, these materials by definition actively interact with the host. Namely, bioactive materials should stimulate the desirable response from the host cells (Bandopadhyay et al., 2019; Navarro et al., 2008), which in terms of orthopedic biomaterials is usually associated with mineralization of the damaged bone and binding between its surface and the implant (Hench, 2006; Navarro et al., 2008) by formation of the layer of HA in the implant-bone interface. This type of bond is called bioactive fixation. The type of bioactivity, which stands for capability of attachment, migration, proliferation, differentiation of osteoprogenitor cells and deposition of extracellular matrix (ECM) in the bone defect, serving the steps towards formation of new bone, is called oseoconductivity. The ability of a material to directly induce formation of bone is called osteoinductivity. Bioactive glasses

(BG) are considered osteoinductive, while less biologically active glass ceramics or calcium phosphate ceramics are osteoconductive (Yu et al., 2015).

In turn, bioresorbable materials are intended to be degraded into simpler compounds and/or elements due to the reactions with the host and be eventually excreted from the host with normal metabolic processes (Bandopadhyay et al., 2019; Dumitriu, 2002; Navarro et al., 2008).

Table 2. Classification of biomaterials.

Class of materials	**Examples**		
	Metals	**Ceramics**	**Polymers**
Biostable (bioinert) materials	Stainless steel Titanium alloys Cobalt-chromium alloys	Alumina Zirconia	Silicone rubber Epoxy Acrylic resins Polyethylene (PE) Polymethyl methacrylate (PMMA) Polyether ether ketone (PEEK)
Bioactive materials		Bioactive glasses (BG) Hydroxyapatite (HA) Apatite-wollastonite (AW)	
Bioresorbable materials	Magnesium alloys Zink alloys Iron alloys		Polylactide (PLA) Polyglycolide (PGA) Polycaprolactone (PCL) Chitosan Cellulose Hyaluronic acid

Data combined from: (Bandopadhyay et al., 2019; Chen et al., 2018; Dumitriu, 2002; Navarro et al., 2008; Su et al., 2021).

Third generation, functional biomaterials, comprises the materials capable of stimulating specific cellular response on the molecular level (Hench and Polak, 2002; Navarro et al., 2008). This group combines the bioactivity and bioresorbability, as well as a specially designed structure together and is used for tissue engineering – regeneration or repair of tissues or whole organs (Bandopadhyay et al., 2019; Hench and Polak, 2002; Navarro et al., 2008). The composition and structure of these materials are aimed at mimicking the ECM to control the attachment, differentiation and growth of cells (Bandopadhyay et al., 2019). They can also be complemented with growth factors, cytokines and other specific

biomolecules and subjected to specific physical stimuli such as mechanical loading (Yu et al., 2015).

2.2.2 Non-metallic skeletal reconstructive biomaterials

2.2.2.1 Biostable polymers

Biostable polymers used in orthopedics include both thermoplastics and thermosets. Thermoplastics are polymers which possess a possibility to be melted and then revert to the solid state after cooling down. Thermosets are polymers which polymerize irreversibly due to formation of covalent bonds (crosslinks; Figure 3A) between the molecules, unlike thermoplastics whose molecules form weak van der Waals bonds between each other. Generally, thermosets have higher chemical and physical stability, higher mechanical properties. In thermoplastics, molecular chains can align parallel to each other, forming so called crystalline areas (Figure 3B). As a rule, the higher the degree of crystallinity in a polymer is, the higher the mechanical properties are (Brinson and Brinson, 2015).

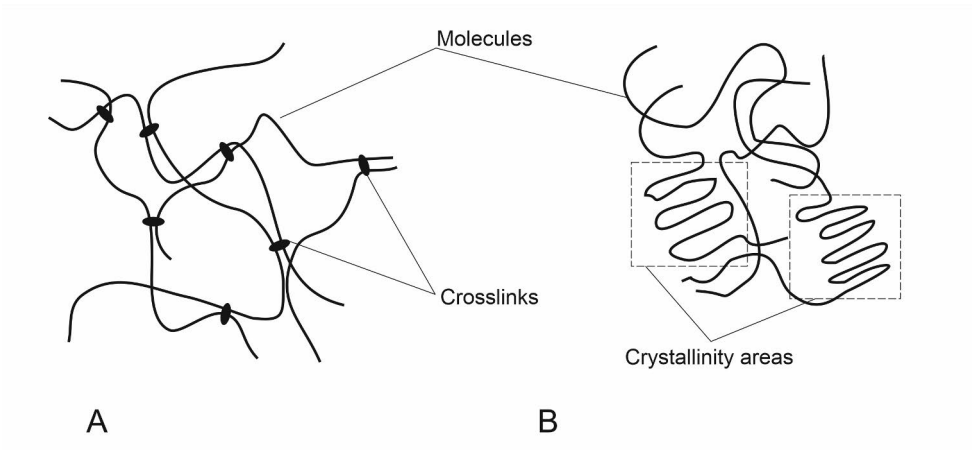

Figure 3. Schematic representation of thermoplastic (A) and thermoset (B) polymers. Inspired by a figure from: (Brinson and Brinson, 2015).

One of the most widely used biostable polymers nowadays is the family of polyaryl ether ketone (PAEK) polymers. Among them, polyether ether ketone (PEEK) and polyether ketone ketone (PEKK) are the most well-studied (Alqurashi et al., 2021; Kurtz, 2019; Yuan et al., 2018) with the former one commercially used in load-bearing orthopedic devices (Boriani et al., 2018; Zoccali et al., 2016). Both materials are semi-crystalline thermoplastics with exceptional biocompatibility and biostability, good mechanical (Table 3) and fatigue properties (Alqurashi et al.,

2021; Kurtz, 2019; Yuan et al., 2018). Despite extremely high, if compared with other engineering polymers, melting temperature, PEEK is considered as a promising material in 3D printing (Garcia-Leiner et al., 2019). On the other hand, the glass transition temperature is also quite high (Table 3), which provides stability of mechanical properties in a wide range of environmental temperature. The main concern regarding use of PEEK in orthopedics is its incapability of osteointegration due to its exceptional bioinertness and hydrophobicity; however, this can be compensated by surface treatment, for instance with titanium, titanium alloys or bioactive ceramics (Barkarmo et al., 2013; Hasegawa et al., 2020; Torstrick et al., 2018; Yuan et al., 2018).

Self-polymerizing PMMA is a thermoplastic polymer widely employed in orthopedics as bone cement, being polymerized *in situ*. It provides a good mechanical fixation and has in general good biocompatibility. Cast PMMA is used for non-load-bearing bone reconstruction such as cranioplasty (Huang et al., 2015; Unterhofer et al., 2017). Also, PMMA is suitable for 3D printing (Espalin et al., 2010; Kotz et al., 2020) However, PMMA possesses a few disadvantages. As a bioinert material, it is capable of forming only morphological fixation to bone; residual acrylic monomers can still leach from the bulk of PMMA, as well as debris produced by mechanical wearing, and invoke adverse reactions such as allergic skin reaction, inflammation or osteolysis (Chiu et al., 2006; Choppadandi et al., 2019; Gautschi et al., 2010; Glant et al., 1993; Moreau et al., 1998; Quinn et al., 1992); in the case of *in situ* polymerization, the reaction occurs at high temperature which may result in thermal necrosis of surrounding tissues. Also, shrinkage up to 7 % takes place after cooling down of the polymerized PMMA leading to potential loosening of an implant fixed with PMMA bone cement (Poitout, 2016).

Among thermoset polymers, bisphenol-A-glycidyl methacrylate (bisGMA) is of particular interest for the present research. This polymer is used in dental practice for decades, often in combination with other co-polymers: triethyleneglycol dimethacrylate (TEGDMA) and/or urethane dimethacrylate (UEDMA) (Asmussen and Peutzfeldt, 1998; Furuse et al., 2011). Photoinitiation system is added to dental resins to achieve curing *in situ* by light irradiation (Emami and Söderholm, 2005). The main drawbacks of bisGMA-based polymers in terms of biological safety are residual monomers leaching from the bulk of polymer (Tuusa et al., 2005; Vallittu et al., 1995). These leaching methacrylate monomers are cytotoxic and can cause local or systematic reactions as explained above for PMMA; in dental applications, additional adverse effects such as contact dermatitis in both patients and personal routinely working with acrylic materials have been reported (Kanerva et al., 1997; Prajapati et al., 2013). In addition, concerns have been shown regarding the release of bisphenol-A from bisGMA-based polymers (Eliades et al., 2011). However, the degree of the adverse effects induced by bisGMA-based materials depends on the

efficiency of curing (Gioka et al., 2005); the same dependency is possible with respect to mechanical properties of light-curable polymers (Anastasio et al., 2019; Emami and Söderholm, 2005).

Table 3. Properties of some biostable polymers.

Material	Glass transition point [°C]	Melting point [°C]	Tensile modulus [GPa]	Tensile strength [MPa]	Density [g/cm^3]
PEEK	143…158	334…350	3.5…5.0	75…101	1.26…1.4
PEKK	154…171	363…386	3.5…5.1	90…115	1.28…1.31
PMMA	104…105	105…160	3.0…4.8	48…78	1.16…1.20
BisGMA/TEGDMA (60/40 %)	371, 472	Thermoset	1.8…10.8	52	1.23

[1] Value for pure bisGMA.
[2] Value for pure TEGDMA.
Data combined from: (Alqurashi et al., 2021; Asmussen and Peutzfeldt, 1998; Kurtz, 2019; Sideridou et al., 2004, 2003; Wagner et al., 2020; Wypych, 2016).

2.2.2.2 Bioresorbable polymers

Bioresorbable polymers may have different mechanisms of degradation, including photo-, thermal-, mechanically and chemically induced ones. The latter one is the most important for biomedical applications. In turn, chemical degradation is usually explained by hydrolysis (passive degradation) but can also be catalyzed by enzymes (active degradation); oxidation may take place as well (Woodard and Grunlan, 2018). The erosion of the polymer which follows the hydrolytic degradation can be either surface or bulk erosion. At surface erosion, the degradation is limited to the material-environment interface, while at bulk erosion it occurs within the whole volume of the polymer (Tamada and Langer, 1993).

The most well-known and widely used group of bioresorbable polymers for biomedical applications are aliphatic polyesters (Albertsson and Varma, 2002; Henton et al., 2005; Scott, 2002). These are synthetic thermoplastic linear polymers. They are hydrophobic (Coulembier et al., 2006; Elsawy et al., 2017) solid materials at normal conditions with different degree of crystallinity. The degradation of polyesters occurs due to the cleavage of bonds between the repeating units. This process is significantly faster in amorphous regions since these are more permeable for water and substances catalyzing the degradation. Therefore, the degradation of crystalline polyesters is associated with further increase of the degree of crystallinity

(Chye Joachim Loo et al., 2005). This also explains the catastrophic failure which may occur even at very low mass losses due to "disconnection" of crystalline regions from each other previously connected by amorphous zones (Scott, 2002). The degradation rate of polyesters is higher in both acidic and base environments than in neutral environment. Thus, bulk degradation is more typical for them due to autocatalysis induced by accumulation of acidic products of degradation in the vicinity and within the mass of the polymer (Dumitriu, 2002; Elsawy et al., 2017).

Polylactic acid, or polylactide (PLA) has two different isomeric forms of its repeating units, L,L- and D,D- lactides. Also, a meso-lactide (D,L) does exist. The amount of each of those isomers affects the chemical and physical properties of PLA. Homopolymers comprise exclusively L,L- or D,D- isomers, while so called "stereocomplex" comprises both types of molecules. These differences substantially affect the physical properties of the PLA (Table 4). In general, L,L-homopolymer has the highest mechanical strength and low elongation at break and therefore is more applicable for orthopedics from the mechanics point of view, however its dissolution rate is low, which is associated with a higher crystallinity (30…40 % for L,L- and 60…70 % for D,D-isomer) in homopolymers (Coulembier et al., 2006; Dumitriu, 2002; Scott, 2002). On the contrary, D,D-/L,L-copolymers, as well as a polymer of D,L-meso-lactide, can be completely amorphous and hence have lower mechanical strength, but higher elongation at break and faster dissolution speed (Coulembier et al., 2006; Dumitriu, 2002). During degradation in the body, PLA is decomposed into lactic acid which is further dissolved to carbon dioxide and water (Maurus and Kaeding, 2004).

Polyglycolic acid, or polyglycolide (PGA) has the degree of crystallinity within the range 45…55 % and differs from PLA by one CH-group in the repeating units. It is less hydrophobic than PLA, thus has a significantly faster degradation rate (Scott, 2002), however has higher mechanical properties (Table 4). Co-polymer of PLA and PGA, poly(lactide-co-glycolide), is therefore often used to obtain relatively high mechanical properties and, at the same time, slower degradation rate than in pure PGA (Maurus and Kaeding, 2004; Nair and Laurencin, 2007; Scott, 2002). The product of degradation of PGA is glycolic acid, further broken down into glycine, which is either excreted with urine or decomposed into water and carbon dioxide (Maurus and Kaeding, 2004).

Other aliphatic polyesters, used in medical practice, are for instance polycaprolactone (PCL) and polydioxanone (PDXO; Table 4).

The remarkable property of polyesters to form self-reinforced structure has been thoroughly researched (Majola et al., 1992; Niiranen et al., 2004; Törmälä, 1992; Vainionpää et al., 1987). This is obtained by different mechanical processes, for instance drawing, shearing, rolling, which lead to formation of groups of oriented molecular chains within the polymer bulk (Törmälä, 1992). In addition to *in vivo*

model studies, self-reinforced polyesters were investigated also in clinical human and veterinary trials (Pihlajamäki et al., 1992; Saikku-Bäckström et al., 2005).

The adverse effects of the use of polyesters are generally the same in all of them. Although the final products of decomposition of polyesters are natural to the metabolic processes, the first step of polyester degradation are monomer acidic molecules. They decrease the local pH value, thus inducing local foreign body reactions, non-infectious inflammations, which might result in such a serious complication as osteolysis (Barber and Dockery, 2006; Böstman and Pihlajamäki, 2000; Meyer et al., 2012; Ramot et al., 2016). The probability of the undesirable reactions is proportional to the degradation rate; hence, PGA more likely causes the adverse reactions than PLA (Ramot et al., 2016).

Beside the synthetic polymers like aliphatic polyesters, naturally derived polymers as cellulose and chitosan are extensively studied for biomedical applications (Table 4).

Table 4. Properties of some bioresorbable polymers.

Material	Glass transition point [°C]	Melting point [°C]	Tensile modulus [GPa]	Tensile strength [MPa]	Density [g/cm^3]	Strength retention [months]	Mass retention [months]
P(L,L)LA	54…65	159…190	1.2…4.8	28…82	1.21…1.29	6	>12
P(D,D)LA	54…65	159…190	1.9	N/A	1.21…1.29	N/D	N/D
P(L,L/D,D)LA	50…60	230	1.9	27…41	1.21…1.29	1…2	12…16
PGA	34…53	210…230	6.1…12.8	61…72	1.46…1.74	1…2	6…12
PCL	-72…-60	57…65	0.2…1.4	7.6…58	1.07…1.20	N/D	24…48
PDXO	-36…0	110	0.3…1.5	6.3…48.3	1.34…1.38	1…2	6…12
Chitosan	140…150	N/D	3.5…7 MPa	0.75	N/D	N/D	N/D
Cellulose	N/D	N/D	9.7	240.5	N/D	N/D	N/D

Data combined from (Albertsson and Varma, 2002; Coulembier et al., 2006; Dong et al., 2004; Engelberg and Kohn, 1990; Liu et al., 2020; Maurus and Kaeding, 2004; Nair and Laurencin, 2007; Wypych, 2016).

2.2.2.3 Bioactive ceramics

Ceramics is generally defined as "the art and science of making and using solid articles which have as their essential component, and are composed in large part of, inorganic nonmetallic materials" (Kingery et al., 1976) or "synthesized inorganic, solid, crystalline materials, excluding metals" (Yamamuro, 2016). A ceramic material, capable of chemically bonding with the bone tissue, is considered bioactive (Yamamuro, 2016). Bioactive ceramics include bioactive glasses (BG), ceramics and glass-ceramics (GC). Bioactive ceramics form a layer of HA on their surface, which is equivalent to the main constituent of the mineral phase of bone tissue, both structurally and chemically. Owing to that, the HA layer bonds with collagen fibers, and hence – with the bone. The mechanical strength of this bonding, called bioactive bonding, is exceptionally high, and can be up to 15…40 times stronger than purely morphological fixation like, for instance, between alumina and bone (Hench and Kokubo, 1998). It was shown experimentally, that when a bioactive bonding is developed in the bone-implant interface, it might be more likely that pulling apart the bone and the implant will result in breakage of either of the two than in breakage of the interface (Nakamura et al., 1985). To measure the bioactivity of materials, a special index of bioactivity I_B was suggested (Hench and Kokubo, 1998):

$$I_B = 100/t_{0.5bb} \quad (1)$$

where $t_{0.5bb}$ is a reciprocal of the half of the time needed for bonding with the bone.

Silicate BG are the derivatives of the plain silicate glasses, *i.e.*, the ones having SiO_2-CaO-Na_2O base. After implantation into the host, BG starts chemical reactions with the body fluids, releasing Na^+ and Ca^{2+} ions and eventually forming a HA layer on its surface, which is preceded by an intermediate Si-rich layer (Rahaman et al., 2011). BG are also known for the capability of inhibiting the growth of pathogenic bacteria (Allan et al., 2001; Drago et al., 2018). Mechanical properties of BG are relatively low (Table 5).

The first composition of BG was suggested by Hench in the beginning of 1970th (Hench, 2006; Hench et al., 1971). It was eventually called Bioglass® 45S5 and approved for clinical applications. Further research showed bioactivity for other glass compositions as well (De Aza et al., 2007). However, the original Bioglass® 45S5 has become the most popular one due to the optimal combination of bioactivity and dissolution rate and the highest bone bonding strength (Jones, 2013; Rahaman et al., 2011; Yamamuro, 2016). Bioglass® 45S5 is considered both osteoconductive and osteoinductive (Rahaman et al., 2011). Moreover, it has been shown that this composition can bond to soft tissues provided that the interface between the soft tissues and bone is immobilized (Wilson et al., 1981).

Another clinically approved composition, S53P4, was developed in 1980th by the group of researchers working at the University of Turku and Åbo Akademi University in Turku, Finland. This glass has lower bioactivity than 45S5 and is often referred to as osteostimulative instead of osteoinductive, but, on the other hand, is named by some researchers as the most effective against pathogenic microorganisms (Hulsen et al., 2017; Ylänen, 2008).

In some BG compositions, boron trioxide can completely substitute SiO_2, which leads to faster dissolution and higher activity. Such glasses are referred to as borate glasses. Despite some concerns regarding the potential toxicity of boron, this type of glasses is considered as a promising one by some researchers (Rahaman et al., 2011).

Phosphate-based glasses, in which the silicon base is replaced with P_2O_5, are fast-soluble and can be effectively drawn in fibers, however their bioactivity is disputable. Thus, fibers of phosphate glasses has been suggested as the reinforcement for completely bioresorbable devices (Colquhoun and Tanner, 2015; Jones, 2013).

Bioactive glass-ceramics (GC) are obtained by a special thermal treatment of BG. Unlike single phase glasses, GC are multi-phase materials. GC have higher mechanical properties, but lower bioactivity index (Hench and Kokubo, 1998). A few commercial GC are available (Table 5).

Table 5. Properties of some bioactive ceramics.

Material	Young modulus [GPa]	Bending strength [MPa]	Fracture toughness [MPa·m$^{1/2}$]	Bioactivity index	Density [g/cm^3]
Bioglass® 45S5	35.0…140.0	40…42	N/D	12.5	1.8…2.9
Bioactive glass S53P4	N/D	N/D	N/D	3.8	N/D
Cerabone®	118.0…120.0	215…220	2.0	3.2…6.0	3.07
Ceravital®	100.0…160.0	100…150	N/D	5.6	N/D
Bioverit®	70.0…90.0	100…180	0.5…1.0	<8.0	2.8
Biosilicate®	70.0…80.0	120…210	N/D	>8.0	N/A
HA	35.0…117.0	115…200	1.0	3.1	3.16
TCP	33.0…120.0	140…154	N/D	N/D	3.07

Data combined from: (Crovace et al., 2016; Hench and Kokubo, 1998; Migonney, 2014; Yamamuro, 2016).

Pure synthetic HA, as well as some other CaP ceramics have been used to replace or augment bone tissue. CaP ceramics possess a good biocompatibility, they are non-

toxic, induce no fibrous tissue formation nor inflammation in the tissues (Migonney, 2014). A few types of CaP ceramics, such as dicalcium phosphate (DCP), α- and β- tricalcium phosphate (TCP) have been used in orthopedic implants and tissue engineering scaffolds. A combination of TCP and HA is also used, called biphasic calcium phosphate (BCP) (Bouler et al., 2017; Migonney, 2014; Poitout, 2016). The osteoinductivity of CaP ceramics is disputable, although they are definitely osteoconductive (Bouler et al., 2017). The mechanical properties are in between of those of BG and GC (Table 5).

2.2.2.4 Polymer-based composites

Composites are materials comprising "two or more separate materials combined in a structural unit" to achieve "desirable properties that cannot be achieved by any of the constituent materials acting alone", while the constituents can be metals, polymers or ceramics (Gibson, 2016). Composites comprise the main phase, matrix, and the dispersed phase, or filler which is embedded in the matrix. The dispersed phase whose main function is increasing mechanical performance is referred to as the reinforcement phase. In orthopedics, composites are widely used to modify not only mechanical, but also chemical, biological properties or any combination of those (Ratner et al., 2012).

Pure polymeric materials often have insufficient mechanical properties to withstand required loads. In that case, their stiffness and strength are often increased by reinforcing the polymeric matrix with, for instance carbon or glass, fibers (fiber reinforced composites, FRC). The fibers can be continuous, *i.e.*, they go through the whole implant uninterruptedly in one of directions. FRC reinforced in one direction are called unidirectionally reinforced (UD); they are highly anisotropic, *i.e.*, their stiffness and strength are different in different directions. In some circumstances it can be undesirable; thus, multiple layers of fibers placed in different directions (usually at angles 0 °, 45 ° and 90 ° with respect to the main axis of the device) are used to form a laminate (Gibson, 2016). Another way to reduce anisotropy is to use randomly oriented chopped fibers, micro- or nanoparticles. However, the mechanical properties of such composites are lower than in UD FRC with the same filler material and matrix-to-filler mass or volume ratio (Gibson, 2016).

As mechanical reinforcement, carbon fibers have been used in FRC orthopedic devices the most extensively (Ratner et al., 2012). Ones of the first clinically evaluated load-bearing fracture fixation plates with continuous fibers had epoxy matrix (Pemberton et al., 1994; Tayton et al., 1982). However, in the following years PEEK became a much more popular matrix material. Moreover, PEEK/carbon FRC are currently the only commercially available load-bearing fracture fixation devices (Boriani et al., 2018; Steinberg et al., 2013; Zoccali et al., 2016). Notably, the

commercially available plates are reinforced with randomly oriented short fiber, which is economically more affordable than continuous FRC and can be manufactured, for instance, by injection molding (Gibson, 2016; Liao et al., 2020). Also, the elastic properties of short-fiber reinforced PEEK are closer to the bone's properties, while the stiffness of continuous fiber-reinforced PEEK is, in fact, comparable to that of metals (Table 6). PEEK reinforced with short carbon fibers have been also studied as potential material for replacing UHMWPE in bearing surface in joint implants, which showed that PEEK/carbon composites suit hip prostheses but should not be used in knee joint prostheses (Brockett et al., 2017; Wang et al., 1998).

Conventional bioinert glass, such as E- or S-glass, fibers have been used in the reinforcement of acrylic-based composites adapted from dental practice. Those bisGMA-based composites have been tested in animals and successfully clinically applied in human cranioplasty (Aitasalo et al., 2014; Piitulainen et al., 2017, 2015; Tuusa et al., 2008, 2007). The proof of concept for load-bearing orthopedic applications of such composites has also been demonstrated (Moritz et al., 2014; Zhao et al., 2009). All these cases dealt with continuous fibers or fabric sheets of those.

In fully degradable composites, natural fibers predominantly consisting of cellulose might have some potential (Jaszkiewicz et al., 2013; Kandola et al., 2020; Sanivada et al., 2020). Fibers drawn from silicate-based (Eichhorn et al., 2021; Lehtonen et al., 2013a, 2013b) and phosphate-based BG have also been studied with aliphatic polyester matrices (Colquhoun and Tanner, 2015). In such composites, BG fibers may serve as both reinforcement and bioactive filler promoting osteointegration and decreasing the adverse effects of polyester degradation.

Table 6. Properties of some composite materials.

Matrix	Filler	Elastic modulus [GPa]	Tensile strength [MPa]
PEEK	Short carbon fibers	7.4…24.0	101…214
PEEK	Continuous carbon fibers	70.0…150.0	900…2000
PEEK	HA	4.3…15.4	43.76…64.71
PLA	Silicate BG fibers	5.4…24.4	136.2…771
bisGMA/TEGDMA	E-glass fibers	17.0…32.2	802…923

Data combined from: (Abdulmajeed et al., 2011; Lehtonen et al., 2013a; Liao et al., 2020; Moritz et al., 2014).

Composites of polymers and micro- or nanoparticles of HA or other bioactive ceramics have also been extensively studied (Boccaccini and Maquet, 2003; Hoppe et al., 2013; Manzoor et al., 2021). In such composites, the filler mostly serves as a bioactive component since it increases stiffness inconsiderably, while strength can even decrease. Nanofillers of carbon origin, such as carbon nanotubes (CNT) or graphene have been studied with different polymeric matrices (Alam et al., 2020; Bai et al., 2020; Díez-Pascual et al., 2010, 2009; Liao et al., 2018; Wang et al., 2019). Metallic particles may serve a composite filler as well (Antoniac et al., 2019; Cifuentes et al., 2017).

2.2.3 Clinical applications

Limb fractures are ones of the most common injuries in both humans and animals (Johnson et al., 1994; Zhang, 2012). Those are often treated by fixation of bone with plates, intramedullary (IM) nails, wires and screws. While the metals remain the *de facto* gold standard in such applications, representing the concept of rigid fixation and absolute stability in the fracture (Uhthoff et al., 2006; Zhang, 2012), an alternative less-rigid fixation concept, providing relative stability in the fracture, relies on more flexible FRC fixation. To the author's knowledge, PEEK/short carbon fibers composition is the only commercially available option for FRC devices, for example, plates for the treatment of humeral or radial (Steinberg et al., 2013) fractures; IM nails for femoral (Zoccali et al., 2016) or tibial (Steinberg et al., 2013) fractures; spine cages or fixation systems for the treatment of vertebral diseases and injuries (Boriani et al., 2018; Kersten et al., 2015). In the latter ones, unreinforced PEEK is also used (Hasegawa et al., 2020; Torstrick et al., 2018).

Non-metallic biomaterials are used in cranioplasty as well as in orthopedics. For instance, cranial implants made of PMMA (Huang et al., 2015; Peltola et al., 2012; Unterhofer et al., 2017), bioactive ceramics (Brie et al., 2013; Henderson and Sinha, 2020; Staffa et al., 2012), PE (Lin et al., 2012) and acrylic-based composites reinforced with bioinert E-glass fibers (Aitasalo et al., 2014; Piitulainen et al., 2015) have been reported. A proof of concept for acrylic-based composites reinforced with bioinert E-glass fibers have been established for load-bearing orthopedic applications (Moritz et al., 2014; Zhao et al., 2009).

Maxillofacial applications are the ones in which bioresorbable implants of PLA, PGA and different modifications and co-polymers of those are relatively often used under conditions which can be considered at least partially load-bearing. Plates and screws of aliphatic polyesters, including composites with bioactive ceramic filler, have been proposed, commercialized and successfully clinically used (Gutwald et al., 2002; Kanno et al., 2018). Bioresorbable metals, such as magnesium, might be considered as alternatives in these applications (Naujokat et al., 2017). Also,

polyester or polyester-based composites have been clinically studied in some relatively low-loaded orthopedic devices, such as screws, pins in joint-related operations (Böstman and Pihlajamäki, 2000; Uchida et al., 2015) or plates in clavicle or metacarpal fractures (Osborn et al., 2018; Sakai et al., 2012). In veterinary, bioresorbable plate fixation was successfully employed in clinical trials (Saikku-Bäckström et al., 2005) and can be of interest for the routine fixation of limb fractures in small animals like toy-breed dogs especially susceptible to osteopenia due to stress-shielding in the rigid fixation (Harasen, 2003; Manchi et al., 2017; Piras et al., 2011). Prototypes of bioresorbable implants for tibial tuberosity advancement (TTA) in dogs to treat cranial cruciate ligament (CrCL) disease have also been proposed and studied clinically, however with contradictory outcomes (Bander et al., 2018; Barnhart et al., 2016).

Due to intrinsic brittleness, bulk BG is not employed as load-bearing devices (Yamamuro, 2016). The most typical application of BG in orthopedics is filling bone voids with BG particles, “as is” or in a putty-like form being incorporated into a binder (Lindfors et al., 2008; Stoor and Frantzen, 2017; van Gestel et al., 2019). CaP ceramics are also used in bone grafting as particles or in scaffolds, including polymer-based composite scaffolds (Rahaman et al., 2011; Zhou et al., 2012). Glass-ceramics has a better toughness, and thus has found some applications as stand-alone implants when the loads are virtually absent or confined to compression. These are, for instance, vertebral prostheses, intervertebral spacers, iliac crest prostheses, laminoplasty spacers (Yamamuro, 2016). CaP ceramics, mostly HA, are used as a bioactive coating to stimulate bone growth and improve the osteointegration of metallic implants, such as stems of joint prostheses (Surmenev et al., 2014).

2.3 Additive manufacturing

Additive manufacturing (AM) technologies, also known as 3D printing and rapid prototyping are those in which an object is formed by selective joining of material layer-by-layer, as opposite to subtractive processes like milling or turning, forming processes like forging, or solidification of bulk of material like casting (Li and Webster, 2018). The unique advantages of AM are the economical effectiveness due to the high degree of automation, low to zero production wastes, virtually constant costs per production unit irrespective of the batch size, and the possibility to produce highly geometrically sophisticated parts which is impossible with conventional technologies (Li and Webster, 2018). 3D printing technologies are evolving rapidly, especially in the last decade after expiration of patents for concrete AM techniques (Antoniac et al., 2019). At the same time, the prices for 3D printers and materials for them are constantly decreasing. In orthopedics, AM technologies may take the advantage of computed tomography (CT) 3D reconstruction of parts of the skeleton

which need to be treated to design patient-specific, perfectly fitting devices (Cronskär et al., 2015). Correspondingly, these printers deal with different types of materials, including metals, polymers, ceramics and composites (Table 7).

Modified fused deposition modeling (FDM) process has been used for fabrication of prototype FRC fracture fixation plates with continuous reinforcing fibers (Kabiri et al., 2021). Standard FDM process allows printing composite objects, for instance scaffolds, with a filament containing bioactive micro- or nanoparticle fillers (Antoniac et al., 2019; Distler et al., 2020; Manzoor et al., 2021). Some materials ready for 3D printing are approved for clinical applications and available commercially, for instance, PEEK powder (Tan et al., 2005), polyester filaments (Mohseni et al., 2018). In some studies, medical-grade materials in other forms, for instance powder (Distler et al., 2020; Manzoor et al., 2021) or granules (Antoniac et al., 2019), have been used for further fabrication of the form appropriate for 3D printing, *e.g.* FDM filament.

Table 7. AM technologies.

Group of technologies	Examples of technology	Applicable materials
Powder bed fusion methods	Electron beam melting (EBM)	Titanium-alloy powder
	Selective laser sintering (SLS)	PEEK powder
Vat polymerization methods	Stereolithography (SLA)	Bioastable or bioresorbable photo-crosslinkable resins
Material extrusion methods	Fused deposition modeling (FDM)	PLA, PGA, PMMA, PEEK
	Paste extrusion	CaP paste
Binder jetting methods	Inkjet printing	CaP ceramic powder and phosphoric acid or polyvinyl alcohol solution as the binder

Data combined from: (Castilho et al., 2017, 2014; Cronskär et al., 2015; Espalin et al., 2010; Grijpma et al., 2005; Kotz et al., 2020; Tan et al., 2005, 2003; Wang et al., 2017; Xu et al., 2021; Yang et al., 2008).

In the field of orthopedic devices, AM technologies have found multiple different applications. Beside the extensive cadaveric and *ex vivo* studies of orthopedic devices (Kabiri et al., 2021; Timercan et al., 2019), 3D printing has been employed clinically in both humans and animals for manufacturing of the whole implants (Castilho et al., 2017, 2014; Choy et al., 2017; Cronskär et al., 2015; Phan et al., 2016; Xu et al., 2021; Zheng et al., 2019), custom patient-specific surgical tools, for instance osteotomy or bone drilling guides (Chen et al., 2015; Xu et al., 2021), molds or other instrumentation needed for a conventional fabrication of

implants (Aitasalo et al., 2014; Peltola et al., 2012), models of the parts of the body, for instance skulls and other bones, to fit or contour the implant against them before the implantation (Peltola et al., 2012; Unterhofer et al., 2017; Zheng et al., 2019).

3D printing is considered as highly appropriate fabrication method for tissue engineering applications (Bose et al., 2013; Tappa and Jammalamadaka, 2018). For instance, fully polymeric (Bodnárová et al., 2019; Gregor et al., 2017), composite polymer/ceramic (Distler et al., 2020; Elhattab et al., 2021; Tan et al., 2005, 2003) and fully ceramic scaffolds (Wang et al., 2017; Yang et al., 2008) have been reported in the literature.

Despite all advantages of AM technologies, there is still a number of limitations in application of those. One of the main drawbacks is lower mechanical properties compared with cast or machine-processed counterparts, as well as some anisotropy in those properties (Wong and Hernandez, 2012). Specifically in biomedical applications, standardization of the design and manufacturing processes of customized devices and other regulatory aspects need significant further development. Also, design of orthopedic devices requires high engineering skills which the medical staff rarely possesses (Phan et al., 2016).

2.3.1 Tailored fiber placement

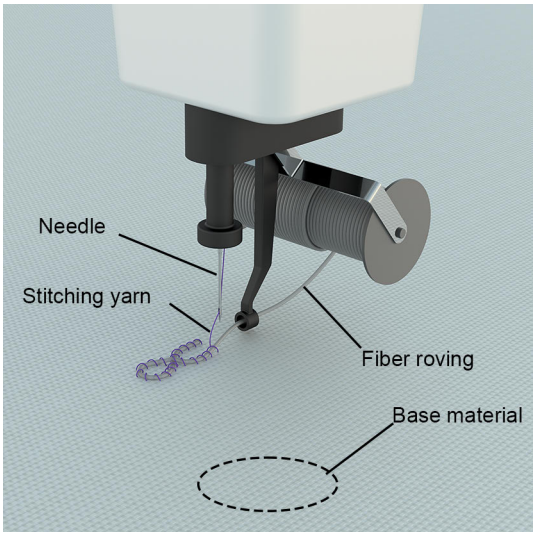

Figure 4. 3D render of a stitching part of a machine for tailored fiber placement.

Tailored fiber placement (TFP) is a textile composite technique in which the continuous reinforcing fiber roving is placed onto the base material following a predefined pattern and stitched to that base material with a yarn (Figure 4). The base material can be, for example, a textile sheet, paper or polymer film. The fiber roving can be placed uninterruptedly and layerwise, which allows to consider TFP as one of the AM technologies (Rihaczek et al., 2020). TFP was developed in Leibniz Institute of polymer research Dresden, Germany, in the 1990th (Mattheij et al., 1998). Among the advantages of TFP over conventional composite layup manufacturing are, for instance, considerably less production wastes, the possibility to adapt the reinforcement

pattern to the expected loads and create sophisticated, biologically inspired patterns. It also allows bypassing the areas in which the holes for fixation screws are needed, thus, on one hand, avoiding drilling the composite through fibers, and on the other hand, providing additional local reinforcement. TFP structures can use both thermosets and thermoplastics as the matrix phase. The resulting structures can be produced by multiple methods depending on the matrix material, including, for example, hot press molding for thermoplastics or moldless vacuum bag resin infusion for thermosets (Gliesche et al., 2003; Mattheij et al., 1998; Rihaczek et al., 2020; Spickenheuer et al., 2008).

2.4 Experimental methods for characterization of skeletal reconstructive biomaterials

2.4.1 Animal models in orthopedic research

Animal models provide important information on the pathological conditions leading to the development of a disease and on the processes accompanying the treatment which is being evaluated. Thus, animal models are the bridge connecting the *in vitro* experiments, such as cell adhesion or proliferation tests, and clinical trials.

According to the contemporary research ethics, employment of animals in the research must be thoroughly grounded. Selection of animals, research questions and a research protocol must be explained in detail. The study design should be approved by the local ethics committee (Migonney, 2014). Nowadays, the rule of "Three R's" introduced in the end of 1950th (Schuppli and Fraser, 2005) is *de facto* the set of the main principles which must be followed. "Three R's" stand for: 1. replace: *in vivo* experiments should be performed only if *in vitro* tests cannot give the adequate answer to the research questions; 2. reduce: the number of animals should be reduced to the minimum providing adequate statistics; 3. refine: animal pain, suffering and distress during the surgical manipulations and the follow-up period should be minimized by proper selection and application of analgesia and anesthesia. The animal experiments should be performed by specially trained personnel (Migonney, 2014).

In the development of orthopedic biomaterials and devices made of those, small animal models, such as mouse, rat or rabbit, are often used due to the ethical, economical and statistical reasons in such studies as biocompatibility and biofunctionality (bioactivity and dissolution behavior) of the materials. Large animals, like goat, sheep, mini-pig, are used in experiments addressing the biomechanics of orthopedics devices as a whole, usually pre-clinical studies or "proof of concept" experiments, in which real clinical settings are reflected

(Migonney, 2014; Narayan, 2019). In addition to kinematics, anatomy and physiology, it is necessary to consider age, sex, genetic and immunological status of the model animals (Migonney, 2014). In the orthopedic research, four bone defect models exist: calvarial defect, segmental (long bone) defect, partial cortical defect and cancellous bone defect (Wagner et al., 2020). It is important to create a "critical size defect", *i.e.* a bony defect which will not heal without intervention (Spicer et al., 2012). The size of such defects varies significantly depending on the species (Wagner et al., 2020).

The biocompatibility and biofunctionality experiments often assume the initial implantation of specimens ectopically (subcutaneously or intramuscularly) (Quinn et al., 1992; Zimina et al., 2020). On later stages of material research, material specimens or functional prototypes of orthopedic devices can be implanted into defects in the tissue of interest, for example calvarial defects (Lee et al., 2019; Spicer et al., 2012; Tuusa et al., 2008), condyle, *i.e.* cancellous bone defects (Daculsi et al., 2011; van der Meulen et al., 2009, 2006), partial cortical defect (Zhao et al., 2009), segmental defects (Kim et al., 2014; Mohseni et al., 2018). Injection of particles imitating wear debris in the joint is another possible experimental setting (Sobajima et al., 2020; Utzschneider et al., 2010).

In earlier studies, such animals as non-human primates (Andersson et al., 1982), dogs (Akeson et al., 1975; Uhthoff and Dubuc, 1971) and cats (Spencer et al., 1990) were used in *in vivo* orthopedics-related experiments, however in the recent two decades this practice has been largely discontinued due to the ethics reasons (Migonney, 2014). In more recent studies, human-size devices have been tested in large animals, for example fracture fixation plates or IM nails (den Boer et al., 1999), spinal implants and fixation (Kandziora et al., 2002; Li et al., 2014; Schwartz et al., 2008). Methods of grafting large bone defects have been investigated, for instance, in sheep metatarsal bone (Viateau et al., 2004) or goat iliac bone (Kruyt et al., 2004).

However, all animal models have significant limitations. For instance, all mammalians excepting primates are quadrupeds, and even in quadruped species there are significant differences in the kinematics and load distribution within the skeleton. Animals are unable to control loads and motion post-operatively. The type and the rate of bone healing is species dependent. For example, haversian osteonal remodeling in cortical bone, present in such mammalians as rabbits, dogs, sheep and primates including humans, normally is not present in rodents. Mechanical properties of bone are highly dependent on the motion kinematics, body mass, loads and geometry. Small-size tissue engineering scaffolds used in rodent models are clinically irrelevant since the access of the cells in the center of the scaffold to the nutrients in the surrounding tissues of the host is significantly easier than it could have been in the human-size scaffold. The impact of some growth factors can be species dependent. Thus, extrapolation of the results of the animal model study to

the actual patients, be it humans or another animal species, should always be done very carefully (Migonney, 2014).

2.4.2 Methods of quantitative characterization of bone formation

2.4.2.1 Histomorphometry

In orthopedic research, histomorphometry is a widely used method for qualitative analysis of the bone tissue morphology and quantitative analysis of metabolic activity and bone growth (Aksoy et al., 2020). Although more modern non-invasive 3D imaging technologies, like CT, provide correct information about the quantitative parameters of bone with less efforts for specimen preparation, the advantage of histomorphometry is the possibility to obtain the detailed information on the activity of bone cells (Aksoy et al., 2020; Compston et al., 2018). While in humans application of bone histomorphometry is limited mostly to studying pathologies due to the invasiveness, in animal models it is commonly used to assess the results of experiments after euthanasia (Allen and Burr, 2014).

The object for histomorphometry most often is cancellous bone, the amount and morphological features of which are assessed by the measurement, for instance, of bone area, trabecular thickness, trabecular number (Aksoy et al., 2020). However, cortical bone parameters, such as perimeters of periosteum and endosteum, can also be measured (Allen and Burr, 2014). Multiple histological sections can be used for estimation of 3D morphological parameters. However, this is based on assumptions that sampling has been done evenly, sections are unbiased and the bone structure is isotropic (Compston et al., 2018). Chemical staining of histological sections is used to distinguish different structural aspects of bone in optical or fluorescence microscopy.

In rats, histomorphometry is usually focused on proximal tibia, while in mice – on the distal femur (Allen and Burr, 2014; Erben and Glösmann, 2019). In both species, lumbar vertebra can also be studied. The choice of the bone for histomorphometry sampling is the high amount of cancellous bone in that bone (Allen and Burr, 2014).

Histomorphometry is used for characterization of such pathological conditions in human patients and animal models as osteoporosis and osteopenia (Tivesten et al., 2004), osteomalacia (Bhan et al., 2018), Paget disease (Seitz et al., 2009). It is also often used, for instance, in the analysis of implant osteointegration (Li et al., 2014; Schwartz et al., 2008; Yuan et al., 2018). Histomorphometry is frequently applied in combination with non-invasive characterization methods, like micro-CT (Lee et al., 2019; Li et al., 2014; Tivesten et al., 2004).

Qualitative assessment of the bone formation can be done by discrimination between lamellar and woven bone. Polarized light microscopy allows for detection of collagen fibers orientation (Allen and Burr, 2014). By staining of osteoids with von Kossa, van Gieson, toluidine blue, Goldner's trichrome or solochrome cyanin stains, static parameters, like area, perimeter and seam width, can be measured (Aksoy et al., 2020; Compston et al., 2018).

Application of *in vivo* fluorochrome labeling with tetracycline compounds, such as demeclocycline or oxytetracycline, can be used to evaluate the consequences of medication or surgical intervention over time (Compston et al., 2018). These methods are also referred to as dynamic histomorphometry (Aksoy et al., 2020). Administration of tetracycline leaves visible marks between mineralized and unmineralized bone at different time points, which allows for calculation of the rate and magnitude of mineralization (Allen and Burr, 2014).

Bone formation and resorption can be assessed by detection of osteoblasts and osteoclasts on the bone surfaces. Goldner's trichrome, von Kossa, McNeal's or hematoxylin and eosin stains are used to identify osteoblasts. The number, surface area, shape of osteoblasts allows for determination of their metabolic state and activity rate (Aksoy et al., 2020). The activity of osteoclasts, *i.e.*, the resorption rate, is evaluated by the measurement of eroded surfaces or erosion depth. Eroded surfaces are determined morphologically, as scalloped holes in cortical bone or divots in trabeculae walls, and thus can be done with most stains. However, TRAP stain is used more frequently in such studies. In human's biopsies and large animal specimens, identification of eroded surfaces is easier than in small animals (Allen and Burr, 2014).

The complexity of the preparation of specimens, high cost and time expenses are the main limitations for application of histomorphometry. Also, it requires high-skilled personnel and is prone to biases due to subjective character of morphological assessment (Aksoy et al., 2020).

2.4.2.2 Micro-CT

Micro-computed tomography (micro-CT) is widely applied in orthopedics-related research for bone morphometry. It can be used for both clinical biopsy samples and animal model samples analyses (Salmon, 2020). Since micro-CT is nondestructive, small animals like rodents can be studied alive (Rosenhain et al., 2018). The physical principles lying behind the micro-CT ideally match the purposes of the architectural representation and analysis of the bone tissue. The projection of mineralized bone tissue has apparent contrast with surrounding soft tissues or empty cavities in the bone when that is irradiated with X-rays (Rosenhain et al., 2018). Nevertheless, the quality of imaging and segmentation of less-dense tissues, for instance cartilage, can

be improved by means of contrast agents (Salmon, 2020). Special software allows for 3D reconstruction of a micro-CT sample by discretization of the series of projections of rotating sample into voxels – units of space with uniform density, represented by a corresponding shade in the grayscale. The resolution of contemporary micro-CT is usually within the range 0.25…200 μm, with scanning time from few seconds to few hours (Cengiz et al., 2018; Clark and Badea, 2021).

Morphometry of bone micro-CT data is generally based on the identification of the volume of interest (VOI) within the obtained 3D model; segmentation of VOI into zones with density being within some predefined ranges; quantitative analysis of different zones. The quantitative analysis includes, for example: measurement of bone volume; calculation of bone volume to total VOI or bone surface to bone volume ratio; measurement of trabeculae thicknesses; finding the structure orientation angle and anisotropy degree (Salmon, 2020).

By comparison of morphometrical parameters in experimental and control groups, micro-CT scans allow for identification of different pathogenic bone conditions or assessment of efficacy of treatment of those conditions in animal models (Salmon, 2020). Such conditions can be, for instance, osteoporosis (Tivesten et al., 2004), arthritis (Quan et al., 2016), tumors (Kassen et al., 2016), osteogenesis imperfecta (Kohler et al., 2021). Evaluation of bone defect healing and osteointegration of implants (Daculsi et al., 2011; Li et al., 2014; Yuan et al., 2018), changes induced by physical loads (van der Meulen et al., 2009, 2006) in animal models are also possible.

When a low radiation dose is used, a long-time follow-up imaging of alive small animal models is possible. This conforms the requirements of the Three R's and, at the same time, produces valuable information for the progression of the model over time (Rosenhain et al., 2018).

Even the most recent micro-CT scanners are susceptible to such image imperfections, as noise and artifacts; in some cases, the available resolution is insufficient. For example, high-resolution images cannot be obtained at low dose irradiation (Salmon, 2020). Nowadays, the deep learning (DL) technologies based on artificial neural networks can be employed to improve the quality of CT scans by denoising, artifact removal and restoration of missing projections (Chen et al., 2017; Han and Ye, 2018; Nauwynck et al., 2020; Shen et al., 2019). In addition, the DL technologies can help in structuring, systematization and analysis of the scans, for instance, for organ segmentation, including bones (Rosenhain et al., 2018), analysis of bone tissues volumes (Asgharzadeh et al., 2020), finding anisotropy directions in trabecular bone (Xiao et al., 2021), predicting mechanical damage or lesions in bone (Ferizi et al., 2019; Shen et al., 2021). Obviously, the development of DL algorithms is continuing, and these will find more applications in the future. It is a common point that DL can significantly reduce the time of analysis and eliminate

misinterpretations due to the tiredness, loss of concentration and personal cognitive biases (Reznikov et al., 2020).

2.4.3 Mechanical testing of biomaterials for load-bearing applications

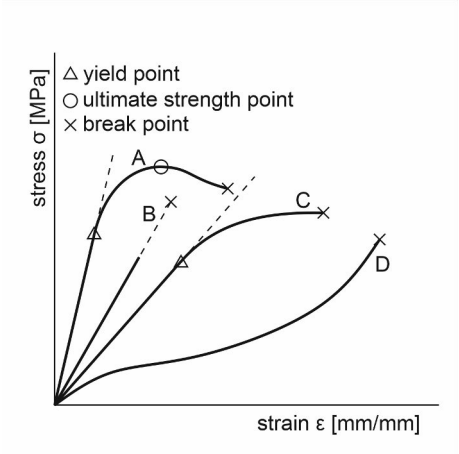

Figure 5. Common types of materials by the shape of their engineering stress-strain curve: A – elasto-plastic ductile material with strain hardening and necking (*e.g.*, metal); B – elastic brittle material (*e.g.*, ceramics); C – elasto-plastic material (*e.g.*, hard polymer); D – hyperelastic material (*e.g.*, rubber). Curves are not in the same scale.

Mechanical tests are aimed at the acquisition of intrinsic mechanical properties of biomaterials, which, in turn, define the structural properties of an orthopedic device and should be taken into consideration in the design. In most of the tests, material specimens are subjected to the controlled loading measured by, for instance, a load cell, and the changes in the shape of the specimen are measured, for instance, with extensometers, strain gages or optical measurement systems. Many of mechanical tests are destructive. The basic data obtained in the testing is often represented by a load-displacement curve, from which various other parameters are then derived. First of all, the load-displacement curve, which is specific for a specific type and specific dimensions of the specimen, is converted into the stress-strain curve (Figure 5) which often can be considered virtually shape- and dimensions-independent. Materials can be tested in various loading modes, for example, uniaxial tension, uniaxial compression, biaxial tension, torsion, shear, three-point bending and four-point bending. Anisotropic materials, such as FRC, ideally should be tested in each direction separately. Many of the mechanical tests are standardized by the International Organization for Standardization (ISO) or the American Society for Testing and Materials (ASTM). Physically equivalent mechanical properties, obtained in different loading modes, should not be directly compared. The mechanical properties can be used in modeling of the structural response of devices made of those materials, for instance, by FEA. To achieve more precise results in modeling, the properties used should be obtained in the loading mode corresponding to the loads expected in the device (Roeder, 2013).

Elastic parameters obtained in the tensile test are considered as the most fundamental ones among other loading modes. These parameters can be used as a general conservative estimation of the mechanical properties of a material, although compression parameters, especially in brittle materials like ceramics, can be significantly higher (Roeder, 2013).

Three-point and four-point bending are widely used in the assessment of load-bearing orthopedic biomaterials due to their simplicity (Manteghi et al., 2017). The elastic properties obtained from the stress-strain curve of three-point bending test are called flexural, or bending modulus and flexural, or bending strength. They are typically higher in three-point bending than in four-point bending, and the latter are higher than equivalent characteristics obtained in pure tension. The flexural properties should be used preferably in cases when similar loading state is expected in a device (Roeder, 2013). A more advanced three-point bending test can be used in the fracture analysis to obtain fracture toughness in shear (ASTM D7905/D7905M-19).

Testing of orthopedic devices as a whole to evaluate their structural properties is also common. There are multiple specified ASTM and ISO standards for testing different types of implants, for example, fracture fixation plates ISO 9585:1990, total hip prostheses ASTM F1280-13, IM devices ASTM F1264-16. Non-standardized procedures have also been published. Testing of whole devices often assumes the creation of specific environmental conditions, such as elevated temperature, sterilization, testing in liquid or after immersion in liquid (Ferguson et al., 2006; Lassila et al., 2002), testing on cadaveric (Etchepareborde et al., 2014) or synthetic (Rowe-Guthrie et al., 2015; Wu et al., 2019) bones. Bending test is often used in the cyclic loading analysis aimed at the assessment of the fatigue performance of orthopedic devices (Lin et al., 2016; Sod et al., 2005).

2.4.4 Finite element analysis

In the design of load-bearing devices, prediction of the load limits and failure mode is crucial. One of the methods to estimate the mechanical behavior of an implant is finite element analysis (FEA). It is based on the discretization of the whole device into multiple finite elements to calculate the internal forces, stresses, strains present in each of those elements and the displacements of those in space, and then derive the overall reaction forces, displacements and other parameters by integration over the whole volume of the device or its structural part (Figure 6). Depending on the required physical parameters, available input material data, complexity of the geometry and kinematics of the device, different degree of simplification of the FEA model can be accepted. For instance, the simulation can be done for one-dimensional beam elements, two-dimensional triangle or square elements or three-dimensional

(3D) tetrahedron, hexahedron or wage elements (Kluess et al., 2010; Sacks et al., 2012).

The FEA model applied in orthopedics related research can solve different types of problems, for instance, a static (Bagheri et al., 2014), impact (Abdel-Wahab and Silberschmidt, 2011) or fatigue (Hambli et al., 2016) problems. Coupled multiphysics problems, such as thermomechanical analysis can be performed, for instance to estimate residual stresses in bone cement (Pérez et al., 2009) or heating due to the friction in a hip prosthesis (Rocchi et al., 2007). Different types of material constitutive models have been used in the analyses of skeletal reconstruction devices, however simple elastic model is prevalent for metals, polymers and ceramics (Bagheri et al., 2014; Castilho et al., 2017; Feerick et al., 2013; Kabiri et al., 2021). Many FEA software packages allow writing user subroutines to extend the capabilities of the basic software. User subroutines have been used, for example, to introduce custom failure criteria or modeling of progressive damage or crack propagation in materials (Feerick et al., 2013).

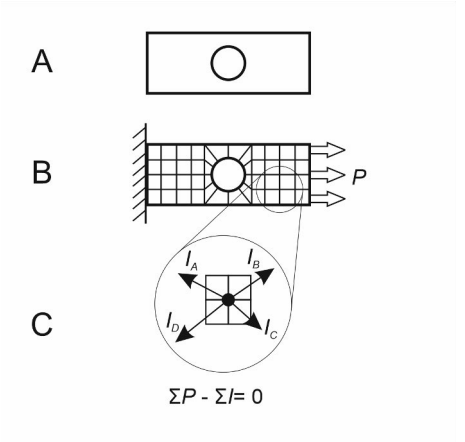

Figure 6. Simplified representation of the finite element analysis: geometrical modeling (A); meshing and defining boundary conditions (B); finding internal forces ($I_A \ldots I_D$) at mesh nodes; solving external (P) and internal (I) forces equilibrium equation (C).

Modeling of bone in some analyses is also needed. Selection of a material model for a biological tissue is challenging due to their inhomogeneity in structure and mechanical properties, and there is no standard approach to modeling of the bone, which is naturally highly anisotropic. Such material models as isotropic linear elastic (Bagheri et al., 2014; Castilho et al., 2017), transversely isotropic linear elastic (Feerick et al., 2013), orthotropic linear elastic (Wu et al., 2017) have been reported. Beside mechanical stresses and strains, some biological properties in tissues can be modeled by means of user subroutines, for instance, bone damage or crack propagation (Feerick et al., 2013), bone mineral density and remodeling in bone due to mechanical stimuli (Doblaré et al., 2002; Lacroix and Prendergast, 2002).

FEA often takes the advantage of such 3D imaging techniques, as micro-CT or CT. This allows for precise geometric representation of the host tissues, first of all bones, in the model (Kabiri et al., 2021; Wu et al., 2017). Some biometrical data, such as coordinates of muscle-to-bone attachment, loads created in those muscles

during normal functioning, can be obtained by direct measurements or from the literature (Castilho et al., 2017; Wu et al., 2017). The material parameters can be taken from the literature (Castilho et al., 2017). However mechanical testing of exactly that material which is used in the device of interest usually provides more precise results due to high scattering of the most mechanical parameters found in the literature, as was shown in the sections above, for instance, for PEEK (3500…5000 MPa for tensile modulus, 75…101 MPa for tensile strength).

The results of FEA of orthopedic load-bearing devices are difficult to be extrapolated due to the high inconsistency in such factors, as the geometry or physiological conditions affecting the kinematics, loads and mechanical parameters of biological tissues among patients. On the other hand, FEA can help in the development of a patient-specific device based on the concrete patient's data. In the design of mass production devices, FEA can help, for example, to compare the mechanical performance with varying input data, or at least simulate conditions which cannot be obtained clinically due to, for example, ethics reasons (Kluess et al., 2010).

2.4.5 Instrumental methods of physical and chemical characterization of biomaterials

Beside the mechanical properties, numerous other physical and chemical properties of biomaterials are routinely evaluated in biomaterials research.

Thermomechanical analysis (TMA) is used to evaluate the change of the length or volume of the specimen of viscoelastic material, such as polymer, as a function of temperature or time, being mechanically loaded at atmospheric pressure. The graph of the change of the length or volume is called expansion curve. The two most notable parameters, defined in TMA, are linear coefficient of thermal expansion (CTE) – the fractional change in dimensions per degree in temperature change, and the glass transition temperature (T_g) – the point of the transition of the viscoelastic material from the glassy state to the rubbery state. TMA has been applied in orthopedic and dental biomaterials research (Melnikov et al., 2009; Sideridou et al., 2004). The glass transition point corresponds the intersection of linear approximations of the glassy and rubbery portions of the expansion curve. The specimen can be loaded statically (static TMA) or dynamically (dynamic TMA). The load can also be negligibly small and applied solely to establish a contact between the probe and the specimen, which is also referred to as thermodilatometry. TMA allows measurements not only of specimens but also whole structural parts provided that they fit the working space of the apparatus (Bair et al., 2009).

Scanning electron microscopy (SEM) is a microscopic technique in which the image of the surface of a sample is formed by scanning with a focused energetic

electron beam. It allows imaging surface morphology which is unresolvable for optical microscopy. Primary electrons, emitted by an electron gun, interact with atoms in the sample surface, invoking emission of secondary electrons and various signals from the surface and the top 1…5 μm of the material. Also, high-energy electrons are reflected, and electromagnetic radiation is emitted. Detection of the secondary, low-energy electrons can be used to obtain high-resolution images with well-defined 3D appearance. It is used, for instance, in the *in vitro* cell-seeding experiments (Wang et al., 2009; K. Zhang et al., 2010). Detection of the backscattered (reflected) high-energy electrons allows for distinguishing areas with different chemical compositions. Backscattered electron imaging (BEI) is widely used in analysis of biomaterials, for example, to differentiate the implant material from the bone (Bandyopadhyay-Ghosh et al., 2010; Daculsi et al., 2011), characterize cross-section or surface of the implant (Kusakabe et al., 2004; Variola et al., 2008). SEM is often equipped with an energy-dispersive X-ray spectroscopy (EDS) detectors used for elemental analysis. EDS is based on the measurement of the quantity and energy of the X-rays induced by electrons reaching and penetrating the specimen surface. The disadvantage of the SEM/EDS is the complex pre-treatment of non-conductive specimens, such as polymers, which need to be coated with, for example, gold or carbon. Also, the specimens should be dehydrated (Wang and Chu, 2013).

Infrared (IR) spectroscopy is frequently applied to identify the chemical compounds and their compositions. It is based on the difference in the absorption of IR radiation by different chemical functional groups at different frequencies. It allows for non-destructive evaluation in solid specimens, as well as in gases and liquids. The spectra are formed by IR beam reflecting or passing from or through a specimen. Reflection, absorption or transmission intensity against wavelength or frequency can be plotted. The most widely used IR instrument is the Fourier-transform IR (FTIR) spectrometer due to its high signal-to-noise ratio (Omidi et al., 2017). Beside the chemicals identification (Elhattab et al., 2021; Kumar et al., 2017), FTIR is often employed to measure degree of conversion (DC) in thermosets, for instance, dental resins (He et al., 2014; Tuusa et al., 2005).

Nuclear magnetic resonance (NMR) spectroscopy is a nondestructive method for evaluation of chemical structures, conformations and dynamics of molecules (Antony et al., 2017; Choppadandi et al., 2019; Kunze et al., 2003). In this method, a sample is placed into electromagnetic field to induce the energy difference between the two spins of specific atoms, for instance ^{1}H; then the sample is subjected to a radio frequency (RF) pulse; the absorption of different wavelengths by the sample is detected by the RF transmitter to form a spectrum, thus forming a full spectrum (Omidi et al., 2017).

Inductively coupled plasma-optical emission spectroscopy (ICP-OES) is based on the detection of the electromagnetic radiation emitted from atoms and ions excited by inductively coupled plasma. In turn, inductively coupled plasma is obtained from the argon torch placed into electromagnetic field. ICP-OES allows for qualitative and quantitative assessment of the presence of different ions and atoms in the sample by the detection of the wavelength and intensity of the radiation emitted by them (Grinberg and Rodriguez, 2019). It is widely used in biomedical research for the ion analysis of solutions, for example, to estimate the activity of bioactive ceramics (Eichhorn et al., 2021; Lehtonen et al., 2013b).

3 Aims

The general goal of the present PhD thesis was to address the main issues related to the practical use of the so called “less rigid fixation” and to suggest a novel concept of non-metallic load-bearing implants intended for use in both animals and humans. To investigate the feasibility of the concept, the following sub-goals were set:

1. To determine the range of possible mechanical properties which can be achieved for small FRC fracture fixation devices with different types of reinforcement and biostable polymeric matrix and evaluate the possibilities of FEA in the design of such devices (Study I).

2. To determine basic physical, chemical and biological properties of a light-curable bioresorbable polymer as a candidate for use as the composite matrix in the *in situ* contourable FRC fracture fixation plate as one of the implementations of the novel implant concept (Study II).

3. To investigate the feasibility of the *in situ* contourable FRC fracture fixation plate and applicability of TFP technique for manufacturing of the reinforcement phase for such devices (Study III).

4. To evaluate *in vitro* and *in vivo* the dissolution behavior, mechanical properties, biological compatibility and efficiency of the combination of candidate materials for the bioactive bioresorbable TTA implant (Study IV).

4 Materials and Methods

4.1 Clinical concept of the *in situ* contourable FRC fracture fixation plate (Studies I – III)

The *in situ* contourable fracture fixation plate has been proposed to alleviate the lack of contourability of the state-of-the-art FRC plates. The suggested plate consists of the three main components: the reinforcement; the polymeric matrix; the shell (Figure 7).

The reinforcement phase should be made of bioresorbable fibers, such as BG fibers (Eichhorn et al., 2021; Lehtonen et al., 2013a, 2013b), by means of TFP technology. Use of TFP would allow for spatial and stress optimization of the reinforcement pattern while bypassing the holes for fixation screws thus eliminating the need for drilling the holes through the fibers (Gliesche et al., 2003; Spickenheuer et al., 2008). In addition, the preforms made by TFP can keep the shape close to the final shape of the device without the external support, which allows for preparation of the reinforcement well in advance and storing it without impregnation into the matrix.

The matrix should be made of a light-curable bioresorbable polymer which could be solidified by irradiation from the standard dental light-curing devices.

The shell is made of a fast-resorbing polymer, for instance oxidized cellulose-based materials. The role of the shell is to seal the reinforcement TFP preform, pre-impregnated in the matrix thus providing the possibility to conveniently handle the flexible pre-preg implant *in situ*.

Before the final hardening, the preform sealed in the shell is put onto the bone, contoured against its shape and pre-fixed with screws. Thereafter, the shell is filled with the uncured matrix polymer thus resulting in the pre-preg. The pre-preg is cured with a hand light curing device, and the screws are tightened.

The concept of such a plate is flexible and can be tailored to various applications in both animals and humans. In the present thesis, an implementation of the concept plate as mini fracture fixation plate for the treatment of the antebrachial fractures in toy-breed dogs was evaluated.

Preliminary investigation of FRC fracture fixation plates of the intended dimensions were done in Study I of the present thesis (Liesmäki et al., 2019). The

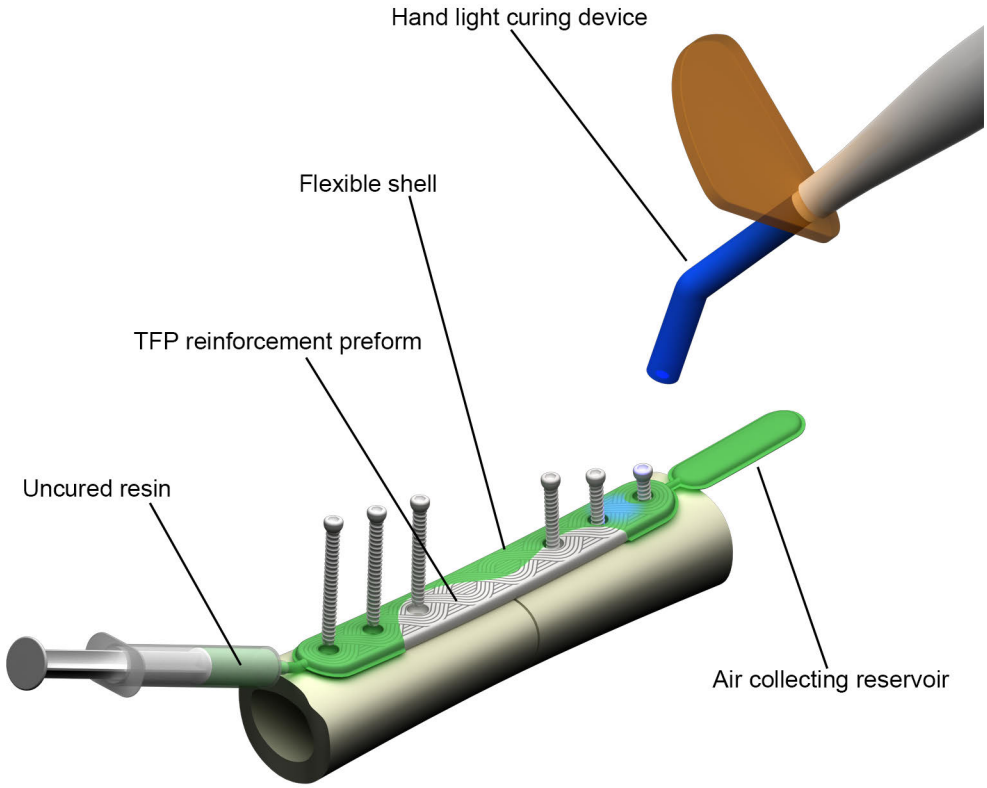

Figure 7. 3D rendering of the *in situ* contourable fracture fixation plate. Image modified from Study II.

theoretical aspects of the concept and the candidate polymer for the matrix phase were investigated in Study II (Plyusnin et al., 2021). The prototype design of the TFP-made reinforcement phase, as well as prototypes of the whole fracture fixation plate in biostable variant were developed and investigated in Study III (manuscript submitted).

4.2 Study I

A possible implementation of the novel implant concept as biostable fracture fixation plates for small animals was examined. The study included two Stages (Table 8). In the first Stage, the materials were tested mechanically in three-point bending as rectangular specimens. The mechanical test was modeled in the first FE analysis stage. In the second Stage, mini plates for small pet animals such as toy-breed dogs,

were prepared from those FRC and tested in four-point bending test. The test of plates was modeled in the second FE analysis.

Table 8. Groups of specimens used in Study I.

Group name	Matrix material	Material of reinforcement	Type of reinforcement	Used in Stage	
				1	2
GFR-BisGMA/unidir	bisGMA	E-glass	Unidirectional continuous fibers	+	+
GFR-BisGMA/sleeving	bisGMA	E-glass	Braided bi-axial sleeving	+	+
GFR-BisGMA/sheet	bisGMA	E-glass	Non-woven sheet	+	+
GFR-BisGMA/short	bisGMA	E-glass	Chopped random-oriented fibers	+	+
CFR-PEEK	PEEK	Carbon	Chopped random-oriented fibers	+	+
SS	Stainless steel	N/A	N/A	-	+

Modified from Study I.

4.2.1 Stage 1

4.2.1.1 Preparation of FRC specimens

The specimens were parallelepipeds with the dimensions 65 × 10 × 3.3 mm. The reinforcement glass fiber structure corresponding to a group (Table 8) was pre-impregnated in unpolymerized bisGMA/TEGDMA oligomer mixture (Table 9) in an aluminum-foil wrapping for one hour in a heat cabinet (BE600, Memmert GmbH + Co.KG, Germany) at 39 °C. Next, the pre-preg was put in a mold made of lab putty. The remaining empty space in the mold was filled with bisGMA/TEGDMA, and the mold was placed in a vacuum oven (VO400, Memmert GmbH + Co.KG, Germany) at 10 mbar, 25 °C for 38 min (approximately 8 min to achieve the target pressure and 30 min at stationary conditions) to remove air bubbles from the oligomer mixture. Then the pre-preg was pre-cured in the mold with a hand light curing device (Elipar S10, 3M ESPE, Germany) for two minutes. The pre-cured specimen was further moved to a vacuum light chamber (Visio Beta vario, 3M ESPE) at the standard program #00 (15 min, RT, 1 mbar) and in a light

oven (Targis Power TP1, Ivoclar AG, Liechtenstein) at the standard program #1 (25 min in total, maximum temperature 104 °C) to finalize the curing process. Specimens of CFR-PEEK were milled out of a bulk of material with a histological saw. The wavelength range of curing devices was 430 – 480 nm.

Table 9. Materials used in Study I.

Material	Type of material	Product name	Manufacturer
BisGMA	Co-monomer	N/D	Röhm Chemische Fabrik GmbH, Germany
TEGDMA	Co-monomer	N/D	Aldrich Chemie GmbH, Germany
CQ	Photoinitiator	N/D	Sigma-Aldrich GmbH, Switzerland
DMAEMA	Cross-linking activator	N/D	Fluka Chemie GmbH, Switzerland
E-glass	Continuous fibers	R338-2400	Ahlstrom Glassfibre Oy, Finland
E-glass	Non-woven sheet	GFT-56G10-80	Ahlstrom Glassfibre Oy, Finland
E-glass	Braided bi-axial sleeving	F22L50X	A&P Technology, Inc., USA
E-glass	Braided bi-axial sleeving	D29L25X	A&P Technology, Inc., USA
CFR-PEEK	Biocompatible polymeric composite	PEEK-OPTIMA Reinforced	Invibio Ltd., United Kingdom
Stainless steel 317L	Biocompatible metal alloy	N/D	Veterinary Orthopaedics Ltd, Hong Kong

Modified from Study I.

4.2.1.2 Three-point bending test of FRC specimens

Three-point bending test was conducted following the ASTM D790-00 standard (Figure 8A). The loading speed was 1 mm/min. A universal testing machine LR30K Plus and a computer software Nexygen (both – Lloyd Instruments Ltd., UK) were used to record the load-displacement curve (Figure 9), from which the stress-strain curve was drawn using the following relations at a moment of time:

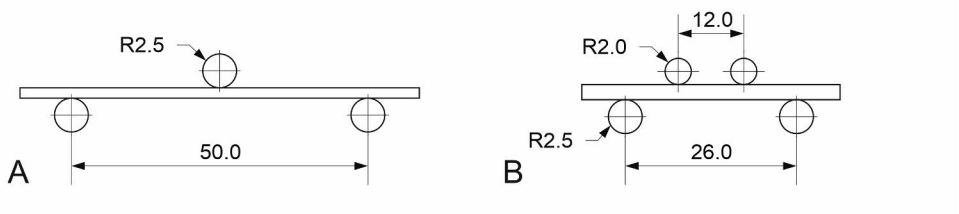

Figure 8. Geometrical dimensions of the experimental setups used in Study I: three-point bending of rectangular specimens (A) and four-point bending of plates (B).

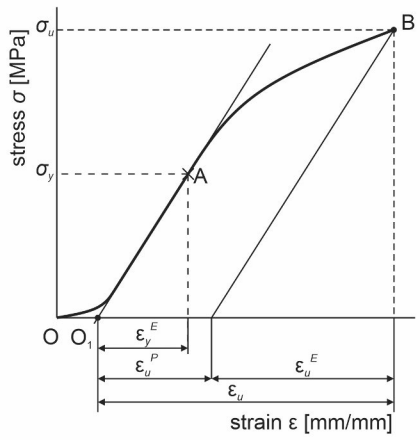

Figure 9. A typical stress-strain plot used for determination of mechanical properties of a composite. *O* is the initial and O_1 is the corrected zero point, A is the yield point, B is the break point, σ_y is the yield strength, σ_u is the strength at break, ε_u^E is the elastic strain at break, ε_y^E is the elastic strain and ε_u^P is the plastic strain at the ultimate flexural strength.

$$\sigma_f = \frac{3 \cdot F \cdot L}{2 \cdot b \cdot d^2} \quad (2)$$

$$\varepsilon_f = \frac{6 \cdot \delta \cdot d}{L^2} \quad (3)$$

where σ_f is flexural stress [MPa], F is the load [N], L is the span between the supporting rollers [mm], b is the width of a specimen [mm], d is the thickness of a specimen [mm], ε_f is strain [mm/mm], δ is the displacement of the loading roller [mm]. Correspondingly, from the stress-strain curve the mechanical parameters of materials were derived: ultimate strength σ_u [MPa] and strain ε_u [mm/mm], measured at the break point, and the flexural modulus [GPa], which was calculated by the formula:

$$E_f = \frac{\Delta\sigma_f}{\Delta\varepsilon_f} \quad (4)$$

i.e. a slope of the linear part of the stress-strain curve.

4.2.1.3 Modeling of the three-point bending test by FEA

The three-point bending test was modeled in FEA software package Abaqus (Dassault Systèmes SIMULIA Corp., France/USA). The dimensions of the experimental setup replicated the actual dimensions. The materials were modeled as homogenized isotropic materials. The inelastic response was modeled using classical

metal plasticity (Bergstrom, 2015). The data for the plastic table were derived from the three-point bending test curves (Figure 9) as follows:

$$\varepsilon = \varepsilon^E + \varepsilon^P \tag{5}$$

where the total strain ε [mm/mm] was decomposed into elastic ε^E and plastic ε^P parts. The onset of the inelastic response was determined graphically at the yield point with the corresponding strength σ_y and strain ε_y.

The supporting and loading rollers were modeled as rigid bodies. Symmetry in two planes was used to simplify the geometrical representation (Figure 10A). The interface between the specimens and loading and supporting rollers was modeled as hard, frictionless contact. The analysis was conducted as static general problem.

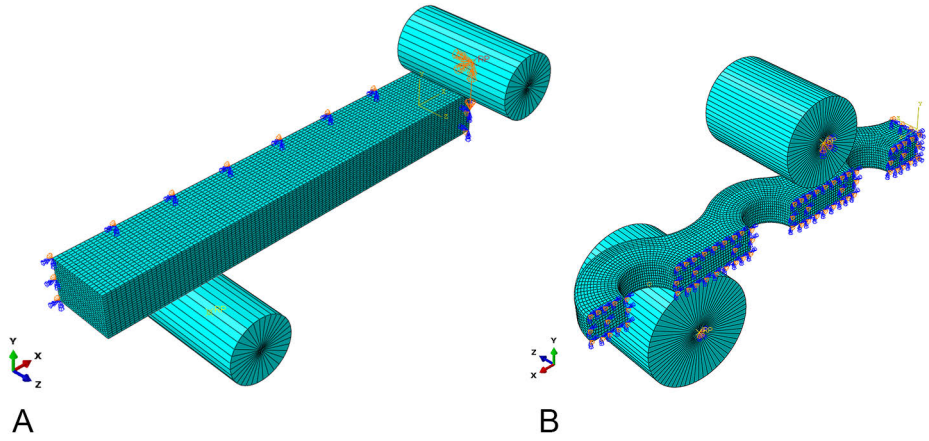

Figure 10. One-quarter finite element models of composite specimen (A) and fracture fixation plate (B) investigated in Study I. Not in the same scale.

4.2.2 Stage 2

4.2.2.1 Preparation of FRC fracture fixation plates

Specimens in Stage 2 replicated a shape of commercially available veterinary stainless-steel fracture fixation mini plate (Figure 11A). In groups GFR/unidir, GFR/sleeving and GFR/short the design was slightly simplified due to technological limitations (Figure 11B). The plates were cut out of pieces of FRC which in turn were prepared following the protocol described in section 4.2.1.1 (Table 4), whereas CFR-PEEK plates were made out of a commercially available piece. Milling machine with computer numerical control (CNC) was used to cut plates.

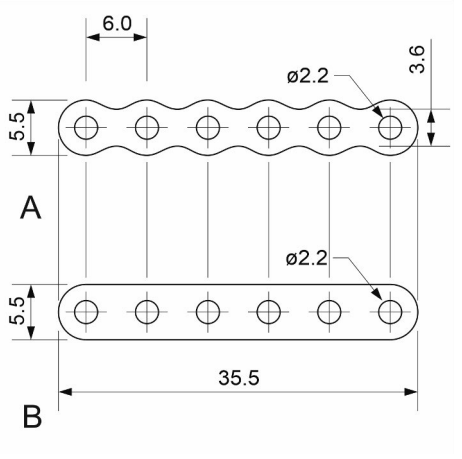

Figure 11. Fracture fixation plates used in Study I: design 1 (A) and design 2 (B). Dimensions in mm.

4.2.2.2 Four-point bending test of fracture fixation plates

The four-point bending tests were carried out on the LR30K Plus machine following the standard ISO 9585-1990 adapted to the dimensions of the experimental setup and available laboratory conditions. The loading speed was 1 mm/min. From the load-displacement curve (Figure 12), quantitative parameters characterizing the plates were derived as follows:

$$E_s = \frac{(2 \cdot h + 3 \cdot k) \cdot S \cdot h^2}{12} \quad (6)$$

where E_s is the equivalent bending stiffness [N·m^2], h is the span between a loading roller and a supporting roller [m], k is the span between loading rollers [m], S is the slope of the linear part of the load-displacement curve [N/m]. The slope, in turn, was defined as follows:

$$S = \frac{\Delta F}{\Delta \delta} \quad (7)$$

where ΔF is the growth of the load and $\Delta \delta$ is the growth of the displacement on the curve segment in question.

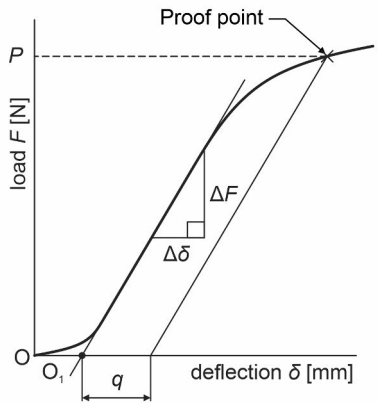

Figure 12. Determination of the maximum load in the four-point bending test in case of substantial plastic deformation. *O* is the initial zero point, *O1* is the corrected zero point, *P* is the load at the proof point, *q* is the offset.

The equivalent bending strength R [N·m] was calculated depending on the behavior of the specimen:

$$R = 0.4 \cdot F_{max} \cdot h \quad (8)$$

- in the cases when no significant inelastic response was observed, where F_{max} is the maximum load at failure [N]:

$$R=0.5 \cdot P \cdot h \quad (9)$$

- in the cases when inelastic response was visibly remarkable, where P is the load at the proof point [N].

The offset q [m] of the proof point (Figure 12) was calculated according to the equation:

$$q = 0.02 \cdot (2 \cdot h + k) \quad (10)$$

4.2.2.3 Modeling of the four-point bending test by FEA

The virtual experimental setup geometrically repeated the actual laboratory setup with acceptable geometrical simplifications. The general FE model conditions were the same as described in section 4.2.1.3 (Figure 10B), and stainless steel was added to the materials as elastic-plastic model. The plastic table of the material was taken from that reported for the analogous alloy (Losertová et al., 2016). The simulations were done for the plates of both designs. Also, both nominal thickness (1.5 mm) and actual thickness averaged within a group were analyzed.

4.2.2.4 Analysis of predicted and experimental results

Non-parametric Spearman rank-order correlation analysis (two-tailed) was applied to assess the correlation between the predicted numerical values and the corresponding measurements obtained in the mechanical test. The significance level was accepted as $P = 0.05$.

4.2.2.5 Analysis of the effect of plate thickness and curvature on the stiffness

A series of additional simulations was conducted to evaluate the effect which might be imposed by variations in the thickness of actual plates, as well as by adding the curvature to the cross-section. The same FE experimental setup was used as described in section 4.2.2.3, while the plate models were simplified. The thickness of the plates varied within the range 1.3…2.0 mm with a step 0.05 mm for both flat and transversely curved plates.

4.3 Study II

The study consisted of four Stages (Table 10). In Stage 1 the synthesis and photopolymerization protocols were created for the novel polymer named PLAMA (polylactide functionalized with dimethacrylate) in two versions with different molecular masses (500 and 1000), and degree of conversion of those was measured by means of FTIR. In Stage 2 basic physical properties were acquired in tensile testing and thermomechanical analysis. Bioresorbability of PLAMA was analyzed in Stage 3 by measuring mass losses and change in pH value of SBF in which specimens of PLAMA were immersed and by investigation of the changes of the mechanical properties of the specimens in three-point bending test after the immersion. The biocompatibility assessment was done in Stage 4 by morphological analysis and proliferation (by WST-8 assay) tests of osteoblast-like cells.

Table 10. Groups of specimens used in Study II.

Group name	Description	Used in stages			
		1	2	3	4
bisGMA	Control biostable light-curable polymer bisGMA/TEGDMA	+	+	-	-
PLAMA-500	Experimental bioresorbable light-curable polymer	+	+	+	+
PLAMA-1000	Experimental bioresorbable light-curable polymer	+	+	+	+
PLDL	Control bioresorbable thermoplastic polymer	-	+	-	+
SS	Control biocompatible metal alloy	-	-	-	+

Modified from Study II.

4.3.1 Stage 1

4.3.1.1 Preparation of oligomer mixtures

The synthesis protocol for both modifications of PLAMA was in general identical. Commercially available PLA diols (Table 11) with corresponding molecular masses (500 for PLAMA-500 and 1000 for PLAMA-1000). Then 2-isocyanatoethyl methacrylate and di-*n*-butyltin dilaurate were added to the mixtures, which were subsequently stirred to acquire homogeneous liquids. To decrease viscosity, the mixtures were diluted with acetone and heated to 45 °C. The process was controlled by FTIR spectroscopy (Vector 33, Bruker Corp.) until the absorbance peak of the -NCO group (2270 cm^{-1}) disappeared. The acetone was removed by vacuum distillation to obtain colorless liquids. FTIR and ^{1}H-NMR (Avance AV 400 MHz, Bruker Corp) spectroscopies were used to achieve the molecular structure of PLAMA (Figure 13).

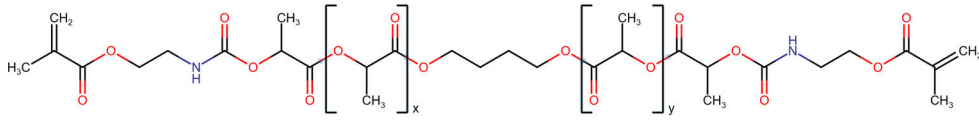

Figure 13. Chemical structure of PLAMA.

4.3.1.2 Preparation of light-curable resins

To obtain the ability to get PLAMA solidified under light irradiation, the prepared oligomer mixtures were blended with ethyleneglycol dimethacrylate. The photoinitiation system was provided by camphorquinone (CQ) and 2-dimethylaminoethyl methacrylate (DMAEMA). The prepared resins were heated to 45 °C and stirred to acquire homogeneity.

4.3.1.3 Light curing protocol

Due to the same photoinitiating components as in the bisGMA/TEGDMA mixtures used in other studies of this thesis, the curing protocol for PLAMA repeated that described in section 4.2.1.1.

Table 11. Materials used in Study II.

Material	Type of material	Additional information	Product name	Manufacturer
PLA diol	Aliphatic diols	Average molecular mass 500	PLA205B	Shenzhen eSUN Industrial Co., Ltd, China
PLA diol	Aliphatic diols	Average molecular mass 1000	PLA210B	Shenzhen eSUN Industrial Co., Ltd, China
2-isocyanatoethyl methacrylate	Cross-linker		I1111	Tokyo Chemical Industry Co., Ltd., Japan
Di-n-butyltin dilaurate	Catalyst		D0303	Tokyo Chemical Industry Co., Ltd., Japan
Acetone	Solvent		N/D	N/A
BisGMA	Co-polymer		N/D	Röhm Chemische Fabrik GmbH, Germany
TEGDMA	Co-polymer		261548	Aldrich Chemie GmbH, Germany
CQ	Photoinitiator		124893	Sigma-Aldrich Corp, USA
DMAEMA	Cross-linking activator		N/D	Fluka Chemie GmbH, Switzerland
Poly (LL-/DL-) lactyde (70/30 %)	Biocompatible thermoplast	Pellets	Purasorb® PLDL 7028	Corbion N.V., the Netherlands
Stainless steel 316L	Biocompatible metal alloy	Fracture fixation plate for humans	N/D	Synthes AG, Switzerland
Cyanoacrylate	Adhesive		CC-33A	Kyowa Electronic Instruments Co., Ltd.

4.3.1.4 Measurement of the degree of conversion

Specimens for measurement of DC were prepared by pouring liquid unpolymerized resin into a through cylindrical cutout with the diameter 6 mm made in a 3 mm-thick piece of lab putty placed on the attenuated total reflection detector of a FTIR instrument (Frontier, PerkinElmer, Inc., USA). The spectrum was measured in the liquid resin, after which it was fully cured following the standard protocol described

in section 4.2.1.1. The solidified specimens were repeatedly measured in 24 h, 72 h, seven days and 28 days after curing. DC was calculated by the formula (He et al., 2014):

$$DC(t) = \left[\frac{1-(A_{C=C}/A_{C=O})_t}{1-(A_{C=C}/A_{C=O})_0}\right] \quad (11)$$

where *DC(t)* is the degree of conversion as a function of time; $A_{C=C}$ and $A_{C=O}$ are the aliphatic (1636 cm^{-1}) and carbonyl (1720 cm^{-1}) peaks of the spectrum.

4.3.2 Stage 2

4.3.2.1 Preparation of specimens for tensile test

Specimens in all groups had the shape and dimensions of the type 1BA with thickness 3 mm according to the standard ISO 527-2:1993 (Figure 14). The final shape was obtained by CNC milling out of billets prepared in different ways depending on the type of material with the flat surfaces dry-polished with sandpaper ISO P2000. The billets in groups PLAMA-500, PLAMA-1000 and bisGMA were made by vacuum molding in PTFE mold with subsequent light curing according to the protocol given in section 4.2.1.1. The billets in group PLDL were vacuum molded in silicone mold out of PLDL pellets in vacuum oven at 200 °C and 10 mbar.

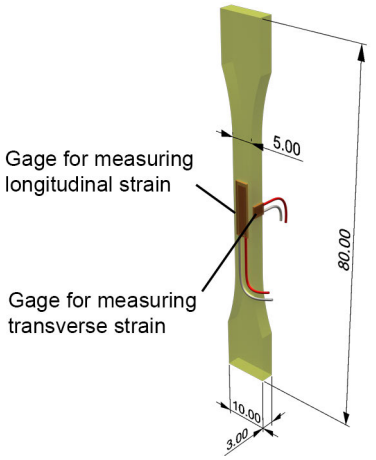

Figure 14. Specimens for tensile test used in Study II.

4.3.2.2 Tensile test

The tests were carried out according to the standard ISO 527-1:1993. The specimens were dried for 72 h in a vacuum oven (10 mbar, RT), after which two strain gages were glued (Table 11) to both flat surfaces of each specimen: a high-elongation gage in longitudinal direction on one side and a normal gage in transverse direction on the opposite side (KFEL-5-120-C1L3M3R and KFGS-02-120-C1-11L3M2R, correspondingly, both – Kyowa Electronic Instruments Co., Ltd.; Figure 14). Then the specimens were kept an hour in a desiccator before the test.

The universal testing machine LR30K Plus was employed for testing. The specimens were fixed in vertical direction; a load cell with maximum load 2500 N was used (XLC-2500-A1, Lloyd Instruments Ltd.). The specimens were pre-loaded up to 1 N and then loaded at the speed 1 mm/min until break. The data from the gages were obtained with a special interface (PCD-300A, Kyowa Electronic Instruments Co., Ltd.). The load-displacement curve and the strain-time curve were obtained. From those, engineering stress-vs-strain graphs were drawn using relations:

$$\sigma = \frac{F}{A} \tag{12}$$

where σ is the stress, F is the load and A is the cross-section of the testing specimen, and

$$\epsilon = \frac{\Delta L_0}{L_0} \tag{13}$$

where ε is strain, ΔL_0 is the elongation and L_0 is the initial length of the gage. The ultimate tensile strength (UTS) was to be determined as the highest point on the curve, which could coincide with the break point.

From the curves, the material parameters were also derived as follows:

$$E = \frac{\Delta\sigma}{\Delta\epsilon} \tag{14}$$

where E is the tensile modulus, $\Delta\sigma$ is the increase in stress and $\Delta\varepsilon$ is increase in strain in the beginning of the stress-strain curve (ε = 0.0025…0.0050), and

$$\mu = -\frac{\epsilon_t}{\epsilon} \tag{15}$$

where μ is the Poisson's ratio and ε_t is the strain in transverse direction.

4.3.2.3 Thermomechanical analysis

Specimens were prepared as parallelepipeds with the dimensions approximately 5 × 5 × 3 mm with the two largest facets dry-polished (sandpaper ISO P2000). Before the measurement, the specimens were kept in a vacuum oven (four hours, 50 °C, 50 mbar).

The measurements of the changes of the thickness of specimens were made on the thermomechanical analyzer Q400 (TA Instruments, USA) in two modes: single-cyclic TMA, when a specimen pre-loaded with a load 0.03 N was cooled down to -25 °C and then heated to 100 °C for PLDL group or 250 °C for the other groups, and

multi-cyclic TMA, when the same procedures were repeated three times to examine the thermomechanical stability of the materials. The heating rate was 2 °C/min. From the recorded thermograms mean linear CTE were calculated.

4.3.3 Stage 3

4.3.3.1 Preparations

Specimens were prepared as parallelepipeds with the dimensions 20 × 20 × 2 mm by vacuum molding in a PTFE mold following the curing protocol described in section 4.2.1.1.

SBF was prepared following the procedure described by Kokubo and Takadama (Kokubo and Takadama, 2006). Sterile filter with pore size 0.2 μm was used to sterilize the liquid before the experiments.

4.3.3.2 Dissolution test

Specimens were kept in plastic tubes with 21 ml of SBF for 84 days in shaking water bath (OLS 200) at 37 °C. After the test, all specimens were washed with distilled water, dried for four days at 37 °C and then kept in a vacuum chamber (10 mbar, RT) for 24 h. Each specimen was weighed before and after the dissolution test.

The pH value of SBF was measured (MeterLab PHM 220; Radiometer Copenhagen, Denmark) before the test and in each plastic tube after removal of the specimens.

4.3.3.3 Three-point bending test

The test was done following the standard ASTM D790-00 on the universal testing machine (LR30K Plus). The basic flexural properties were calculated: modulus [GPa], ultimate strength [MPa] and strain at ultimate strength [mm/mm], strength [MPa] and strain [mm/mm] at break. The calculations were done according to Equations (2)…(4).

4.3.4 Stage 4

4.3.4.1 Preparation of specimens

All specimens had a parallelepiped shape with the dimensions 4 × 4 × 1.7 mm to fit a standard 96-well plate. Specimens in groups PLAMA-500, PLAMA-1000 and

PLDL were cut out of a plate, preliminarily vacuum molded as described in section 4.2.1.1. In group SS specimens were CNC milled out of a commercial fracture fixation plate for humans (Table 11). The top surface of each specimen was polished with sandpaper (ISO P4000). Polymeric specimens were sterilized by gamma-rays, while metal specimens were sterilized in autoclave.

4.3.4.2 Preparation of cells

As a substitute for osteoblasts, human osteosarcoma cells (MG-63) were employed. The cells were kept in Dulbecco's modified eagle medium (Table 12) supplemented with fetal bovine serum, penicillin-streptomycin and L-glutamine. Petri dishes with the medium were placed in closed cabinets with humidified atmosphere (5 % CO_2, 37 °C). The cells were taken from the dishes after reaching 70 % confluence using 0.05 % trypsin-EDTA. Material specimens were rinsed with the cell culture medium and then placed into 96-well plates, after which cells were seeded on the top of the specimens (5000 cells/specimen).

Table 12. Materials additionally used in Stage 4 of Study II.

Type of material	Additional information	Product name	Manufacturer
PBS		Gibco 10010015	Fisher Scientific, USA
Dulbecco's modified eagle medium		Gibco 21969035	Fisher Scientific, USA
Fetal Bovine Serum		N/D	Fisher Scientific, USA
L-glutamine		Gibco 25030081	Fisher Scientific, USA
Penicillin-streptomycin	10000 U/ml	Gibco 15140122	Fisher Scientific, USA
Trypsin-EDTA, phenol red	0.05 %	Gibco 25300054	Fisher Scientific, USA
Triton™ X-100	1 % solution in PBS	X100	Sigma-Aldrich Corp, USA
Hoechst 33258		861405	Sigma-Aldrich Corp, USA
Rhodamine phalloidin		Invitrogen™ R415	Fisher Scientific, USA
Glycerol	70 % solution PBS	N/D	N/D
Paraformaldehyde	4 % solution in PBS	N/D	N/D
Sodium dodecyl sulfate		N/D	N/D
WST-8		CK04	Dojindo Laboratories, Japan

4.3.4.3 Cell morphology test

After seeding on specimens, cells were cultured in a closed cabinet with humidified atmosphere (5 % CO_2, 37 °C). After four, eight and 24 h three specimens from each group were taken out for morphological examination. Further procedures were performed at RT. The removed specimens were rinsed with PBS, and the cells on them were fixed with solution of paraformaldehyde in PBS for 20 min (Table 12). Triton X-100 was used for 5 min to permeabilize cells. Rhodamine phalloidin (for 30 min) and Hoechst 33258 (for 10 min) were applied for staining cells. The specimens were rinsed with PBS after each step. Stained cells were visually investigated with a fluorescence microscope (Leica DMRB, Leica Camera AG, Germany). For that purpose, specimens were put in a drop of glycerol/PBS solution on a microscope glass plate. For the subsequent morphological assessment cells on

specimens were photographed (Olympus DP72, Olympus Corporation, Japan). The images were pre-processed in the software package CellSens Entry 1.5 (Olympus Corporation) and further processed in Photoshop CS 2019 (Adobe Inc., USA). To assess the morphological changes in cells, the area and the ratio between the length and width of equal number of cells from each group of specimens was calculated at each time point.

4.3.4.4 Cell proliferation test

The proliferation of cells was measured in 24 h and 96 h (humidified atmosphere, 5 % CO_2, 37 °C) after seeding on specimens and compared with proliferation in culture medium without specimens. Assessment was done with WST-8 assay (Table 12). After adding WST-8 and incubating the cells for one hour (humidified atmosphere, 5 % CO_2, 37 °C) sodium dodecyl sulphate was added to the medium, and the obtained solution moved to a new well plate for subsequent measurement of light absorbance at 450 nm (microplate reader Wallac 1420 Victor2, PerkinElmer, Inc.).

4.4 Study III

A case of bioactive *in situ* contourable fracture fixation plate as one of the advanced implementations of the novel implant concept, potentially fully bioresorbable, was evaluated. The study comprised two general Stages. In the first Stage a prototype of *in situ* contourable FRC plate reinforced with a pilot TFP preform was prepared in two versions (with and without polymer shell) and tested mechanically in three-point bending test. The second Stage included design of several spatially re-arranged patterns of TFP preforms, preparation of plate prototypes reinforced with the selected pattern and comparison of that with the pilot design. Four-point bending test of plates, as well as four-point bending and torsional tests of osteotomized cadaveric chicken tibiotarsi fixed with those plates were conducted.

4.4.1 Stage 1

4.4.1.1 Preparation of specimens

The reinforcement phase for specimens in the PTFP and PTFP/shell groups (Table 13), the prototypes of *in situ* contourable plates, were prepared by means of TFP technique. The pattern of the prefom for these groups was developed in collaboration with TraceRay Oy (Finland) and Biontec Bionic Composite Technologies AG (Switzerland). Preforms were immersed in liquid

bisGMA/TEGDMA pre-polymer (Table 14) to obtain pre-pregs. The pre-pregs in the group PTFP/shell were placed in vacuum-molded PC shells developed in collaboration with TraceRay Oy (Finland) and Medical Advanced Manufacturing Research Centre (AMRC), the University of Sheffield (UK). The PC was used in this pilot study as a substitute for bioresorbable polymer, such as aliphatic polyesters. Next, the pre-pregs were light-cured, at that pre-pregs in the group PTFP were cured as such, without a shell. Specimens from the group Unreinforced were solid pieces of polymer without reinforcement which got the same shape as the specimens from the other two groups in a mold. Light curing was carried out for all three groups according to a procedure which modeled the actual in situ curing in the conditions of a surgery by a hand device solely (Elipar S10) for 40 seconds.

Table 13. Groups of specimens used in Study III.

Group name	Matrix material	Material of reinforcement	Type of reinforcement	Used in Stage	
				1	2
Unreinforced	bisGMA/TEGDMA (60/40)	N/A	N/A	+	-
PTFP/shell[1]	bisGMA/TEGDMA (60/40)	E-glass fibers	Pilot design of TFP preform	+	-
PTFP	bisGMA/TEGDMA (60/40)	E-glass fibers	Pilot design of TFP preform	+	+
Unidir	bisGMA/TEGDMA (60/40)	E-glass fibers	Unidirectional fibers	-	+
OTFP-G	bisGMA/TEGDMA (60/40)	E-glass fibers	Optimized design of TFP preform	-	+
OTFP-PLA	PLA	E-glass fibers	Optimized design of TFP preform	-	+
Intact bones	Chicken cadaveric tibiotarsi	N/A	N/A	-	+

[1] Material of the shell: PC.
Modified from Study III.

4.4.1.2 Three-point bending test

The test procedures were developed based on the general recommendations given in the standard ASTM D790-00. The specimens were placed symmetrically on the two supporting rollers. The span between the supporting rollers was such that either roller

was in the middle between the two outermost screw holes from both ends of the specimen. The loading roller was placed in the center between the two supporting ones. Shimadzu universal testing machine (Shimadzu Corporation, Japan), equipped with 10 kN load cell, was employed for the test. Specimens were pre-loaded with the load 0.2 N. Loading speed was 1 mm/min.

Table 14. Materials used in Study III.

Material	Type of material	Additional information	Product name	Manufacturer
BisGMA	Co-polymer		N/D	Röhm Chemische Fabrik GmbH, Germany
TEGDMA	Co-polymer		261548	Aldrich Chemie GmbH, Germany
CQ	Photoinitiator		124893	Sigma-Aldrich Corp, USA
DMAEMA	Cross-linking activator		N/D	Fluka Chemie GmbH, Switzerland
PC	Biostable thermoplastic		N/D	N/D
PLA	Bioresorbable thermoplastic	Thread 167 dtex	N/D	Trevira GmbH, Germany
E-glass	Continuous fibers	Roving 600 tex	R338-600	Ahlstrom Glassfibre Oy, Finland
E-glass	Continuous fibers	Roving 300 tex	EC14 300 TD44C	Saint-Gobain Vetrotex, Germany
Chicken cadaveric tibiotarsi	Natural substitute of a dog tibia		N/D	Atria Oyj, Finland
PMMA	Biostable thermoplastic		N/D	Vertex Dental B.V., The Netherlands

Modified from Study III.

4.4.2 Stage 2

4.4.2.1 Spatial optimization of the TFP reinforcement pattern

The pattern of the TFP reinforcement used in Stage 1 was further corrected to investigate the possibilities to achieve more uniform spatial filling of the plate's volume with the reinforcement and to modify the structural mechanical properties.

During the optimization, the fiber rovings were logically divided into three groups: longitudinal (to provide bending stiffness), transverse (to provide torsional stiffness) and space-filling rovings (to provide the integrity of the whole plate and to reinforce the space around the screw holes to resist the pulling out of screw heads). The aim was to keep the balance between those groups. Several patterns were modeled in CAD software AutoCAD 2018 (Autodesk Inc., USA) and incorporated into FE mesh for the FEA program Abaqus by means of a special software AOPS (Leibniz Institute of polymer research Dresden, Germany) as individually locally oriented 3D elements. In each of those elements the local coordinate system (CS) was rotated to align with a tangent of the reinforcing fiber roving virtually passing through that element. The matrix and reinforcement were homogenized and represented as anisotropic elastic material with the three axes of anisotropy aligned with the elements' local CS. The FE representations of the TFP plates were modeled in four-point bending of plates, four-point bending and torsional test of osteotomized chicken tibiotarsi fixed with those plates. Kinematically the virtual experimental setups replicated the actual ones used in mechanical tests however were made with acceptable geometrical simplifications. The simulations were done as static general problems. Loading rollers and fixtures were represented as rigid bodies.

4.4.2.2 Preparation of plates

One of the newly developed TFP patterns was selected for the preparation of actual specimens. Preforms were made in two versions (Table 13). In the group OTFP/G the preforms were stitched out of pure fiber rovings on a non-woven glass-fiber textile using PLA multi-filament thread (Table 14). In the group OTFP/PLA the preforms were stitched on PLA film out of a hybrid yarn using PLA thread. The hybrid yarn was braided out of a fiber roving and the same PLA thread which was used as the stitching material. The preforms from the group OTFP/G (Figure 15) were impregnated in bisGMA/TEGDMA pre-polymer and solidified to obtain plates following the full light-curing cycle described in section 4.2.1.1.

The preforms in the group OTFP/PLA were placed in aluminum mold, which was further put in a hot press. The mold was mechanically subjected to the maximum pressure 10 bar whereas the air was deflated until the air pressure in the working zone achieved 50 mbar. The mold was heated to 200 °C for five minutes, after which it was cooled down within two hours to RT. Thus, all PLA containing in the preform (the thread in the hybrid yarn, the stitching thread and the base film) was molten, homogenized while in the liquid state and then solidified after cooling down. The fiber rovings became completely enclosed in the PLA matrix, maintaining the spatial arrangement which was created in the preform.

The plates in the Unidir group replicated those used in Study I (section 4.2).

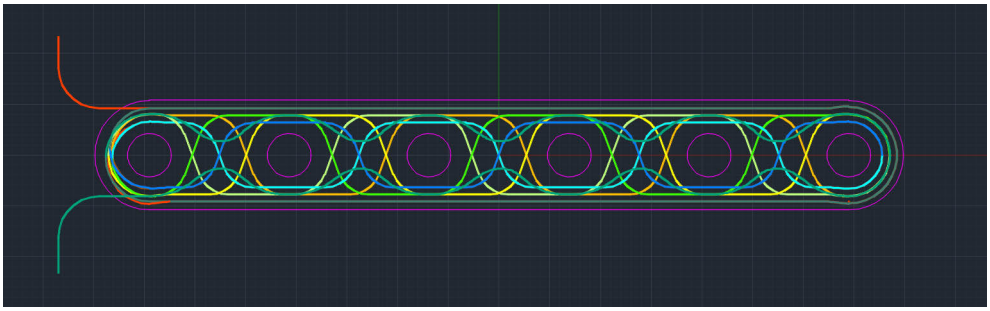

Figure 15. Pattern used in the preparation of TFP plates in the groups OTFP/G and OTFP/PLA.

4.4.2.3 Preparation of bone specimens

Chicken tibiotarsi were extracted from commercially sold chicken drumsticks (Table 14). Soft tissues were removed mechanically, after which the bones were wrapped in moisturized paper towels and kept in a refrigerator at 8 °C for 24 hours at most. Bones for torsional test were cut from the ends to achieve 70 mm length using hand dental instrument (Typ 970, KaVo Elektrotechnisches Werk GmbH, Germany) with a diamond-surfaced cutting disc. Both ends were embedded in parallelepiped pieces of PMMA, intended for fixation in the testing machine, using a PTFE mold. Six through holes with the diameter 1.6 mm were drilled in each bone for both bending and torsional tests. Then, the bone specimens were divided into two approximately equal halves so that the cut was made between the central two holes. The halves in each pair were fixed with a plate from one of the experimental groups using six surgical screws 2.0 × 12 mm (MF Cortex Screw, Synthes Holding AG, Switzerland; Figure 16). As a control, a part of bone specimens was left uncut and undrilled and thus tested in both bending and torsional tests without plates installed.

4.4.2.4 Four-point bending test of plates

The four-point bending was conducted according to the standard ISO 9585-1990 using the same experimental setup and under the same conditions as described for Study I (section 4.2.2.2). The quantitative results were calculated by Equations (6)…(10).

4.4.2.5 Four-point bending test of bone specimens

The experimental setup (Figure 16A) was based on the literature (Sod et al., 2005). The universal testing machine LR30K Plus was used. The measurement of the applied load continued until the failure of the tested construct at the loading speed 1 mm/min. Quantitatively, the results of the test were assessed by analogy with the four-point bending of plates using Equations (6)…(10).

4.4.2.6 Torsional test of bone specimens

The experimental setup for the torsional test was based on the literature (Sod et al., 2005). A testing machine (Avalon Technologies, USA) was used. Bone specimens were fixed vertically in the natural direction (Figure 16B). A constant rotation at the angular speed 64 °/min (Zhao et al., 2009) was applied to the lower part of the specimen until the failure of that. Maximum torque at failure was measured and torsional stiffness of the construct was calculated from the torque-rotation angle curve (Sod et al., 2005; Zhao et al., 2009):

$$S_\tau = \frac{\tau \cdot c}{\alpha} \tag{16}$$

where S_τ is torsional stiffness [N·m/rad], c is a degrees-to-radian conversion coefficient equal to 180/π [°/rad] and α is the rotation angle [°].

To simulate the normal physiological loading of the tibiotarsi, rotation was applied in different directions depending on the body side from which a bone was removed. Thus, by analogy with the gate of bipedal mammals, rotation was applied outwards of the median plane if seen from above (Yang et al., 2014).

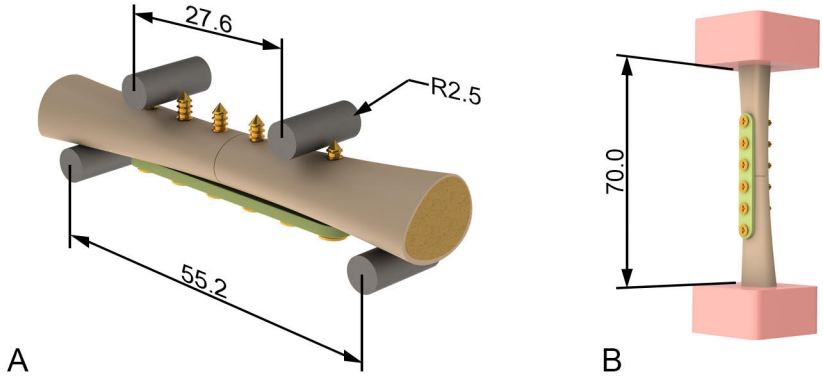

Figure 16. 3D rendering of bone specimens fixed with fracture fixation plates used in Study III: in four-point bending (A) and in torsional tests (B).

4.5 Clinical concept of the bioactive bioresorbable TTA implant (Study IV)

The concept TTA implant should consist of the three main components: 1. load-bearing shell; 2. sealing; 3. bioactive filler (Figure 17).

The load-bearing shell is made of a relatively slow-degrading polymer and should be strong enough to withstand the loads acting in the stifle during the walk. The second function of the load-bearing shell is to serve a container for the bioactive filler. The shell should gradually transfer the load-bearing function to the new bone tissue growing through the cells of the shell.

The sealing is made of a relatively fast-degrading polymer. Its only function is to prevent the bioactive filler from scattering until the implantation. After implantation, the sealer should be resorbed as soon as possible to open the bioactive filler to the body fluids. To increase the degradation speed and to guarantee the immediate contact between the filler and the body fluids, the sealer is made perforated.

The bioactive filler can be selected according to the clinical conditions.

In Study IV of the present thesis, a preliminary investigation of the materials intended for the use as the load-bearing shell (Dioxaprene® 100M, Poly-Med Inc), the sealer (Max-Prene® 955, Poly-Med Inc) and the bioactive filler (BG particles) was carried out from the prospective of the aforementioned concept.

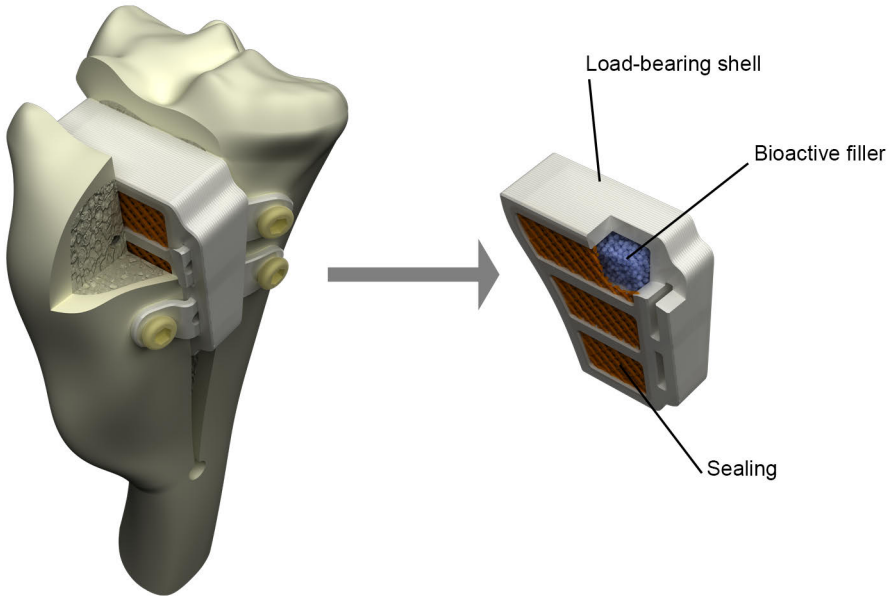

Figure 17. 3D render of the bioresorbable bioactive TTA implant.

4.6 Study IV

A concept prototype of the polymeric-based bioactive bioresorbable TTA implant for dogs was investigated in Study IV. The study comprised three Stages with different sets of groups (Table 15). In the first Stage, the applicability of the FDM technology for the preparation of the dog TTA implants was evaluated in the SBF immersion test of simplified implant prototypes made of technical grade PLA. In the second Stage the actual bioresorbable medical-grade polymer filaments for FDM printing were assessed in compression test before and after short-term dissolution test in SBF. In the third Stage, the experimental implants were prepared. The materials of the experimental implant components were selected so that in an actual TTA implant, those components would be dissolved at different speed providing the necessary change of the load-bearing properties of the implant over the time of bone healing. First, the bioresorbability and bioactivity of the experimental implants were assessed *in vitro* in SBF. Second, the biocompatibility and efficiency of the osteointegration were scrutinized *in vivo* in the rabbit model by means of histological and micro-CT analyses of samples extracted from the animals. Additionally,

mechanical performance of the actual TTA implant was estimated in a simple FEA based on the mechanical properties obtained in Stage 2.

Table 15. Groups of specimens used in Study IV.

Group name	Description	Used in Stages		
		1	2	3
Implant prototypes/BG	PLA casing with BG filler immersed in SBF	+	-	-
Implant prototypes/FG	PLA casing with FG filler immersed in SBF	+	-	-
Control BG	Control group	+	-	-
Max-Prene	Pieces of filament Max-Prene® 955 immersed in SBF	-	+	-
Dioxaprene	Pieces of filament Dioxaprene® 100M immersed in SBF	-	+	-
Pure SBF	Control group	+	+	-
Experimental implants	Casing of Max-Prene® 955, insert of Dioxaprene® 100M, BG filler.	-	-	+
Control implants	Ti-alloy implants. Control group	-	-	+
Empty defects	Control group	-	-	+

Modified from Study IV.

4.6.1 Stage 1

4.6.1.1 Preparations

Casings for prototypes were printed out of technical-grade PLA filament on a general-purpose FDM printer (Leapfrog Creatr, LeapFrog 3D Printers, the Netherlands; Figure 18A). Two groups with different fillers were prepared. The third group, control BG, was pure BG granules (Table 15, Table 16).

SBF for the immersion test was made as described in section 4.3.3.1.

4.6.1.2 SBF immersion test

Specimens were placed in plastic sterile tubes with 50 ml of SBF for seven days. SBF was changed every 24 h ["quasi-dynamic" test (Hoppe et al., 2013)] to avoid the saturation of SBF and subsequent precipitation of HA formed from Ca ions

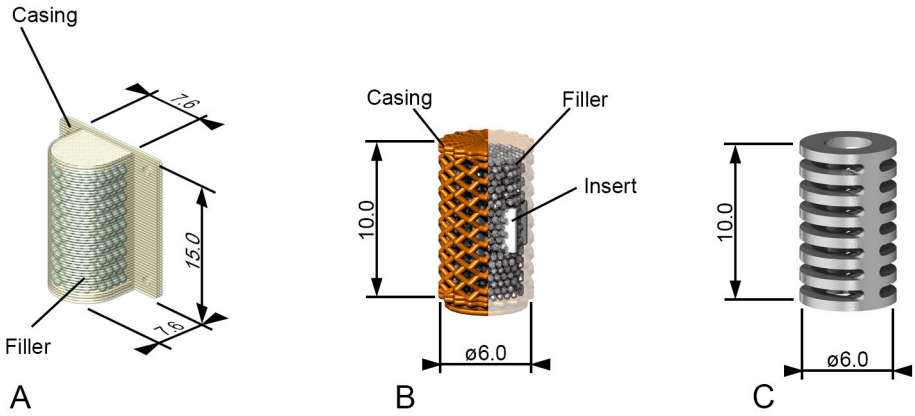

Figure 18. Specimens used in Study IV: prototype for stage 1 (A); experimental implant for stage 3 (B); control titanium implant for stage 3 (C). Modified from Study IV.

contained in the liquid instead of the ones contained in the BG granules in prototypes. Thus, the risk of false-positive result of the experiment was diminished. The tubes with SBF were kept in a shaking water bath (OLS 200, Grant Instruments Ltd., UK) at 37 °C.

4.6.1.3 Analysis of ion concentrations in SBF

Samples of SBF used on the seventh day of the immersion test were collected. Concentrations of Ca, P and Si ions in the liquid were measured by means of inductively coupled plasma-optical emission spectroscopy (ICP-OES; Optima 5300 DV, PerkinElmer, USA).

4.6.1.4 Analysis of CaP formation

Samples of the prototype casing's walls and the filler were investigated by means of back-scattered electron imaging (BEI). The precipitation of CaP on the surface of the prototype casing samples was studied by desktop scanning electron microscope with energy dispersive X-ray spectroscopy (SEM/EDS; Phenom ProX, Phenom-World B.V., the Netherlands).

Table 16. Materials used in Study IV.

Material	Type of material	Additional information	Product name	Manufacturer
FG	Filler	Granules with fraction size 800 – 1000 µm	N/A	N/A[1]
BG	Filler	Granules with fraction size 800 – 1000 µm (Stage 1) and 300 – 500 µm (Stage 2)	S53P4	BonAlive Biomaterials Ltd., Finland
SBF	Body fluid substitute		N/A	N/A[2]
PLA	Pellets	Filament (diameter 1.75-mm) was drawn from pellets	Ingeo Biopolymer 4043D	NatureWorks LLC, USA
PGLA	FDM filament	Diameter 1.75-mm	Max-Prene® 955	Poly-Med, Inc., USA
PDXO	FDM filament	Diameter 1.75-mm	Dioxaprene® 100M	Poly-Med, Inc., USA
Ti-6Al-4V	Implant material	Humeral locking nail	VersaNail®	DePuy International Ltd., USA

[1]See details of the composition in (Kokubo and Takadama, 2006).
[2]See details of the composition in (Madanat et al., 2009).
Modified from Study IV.

4.6.2 Stage 2

4.6.2.1 Preparation of specimens and materials

The specimens of commercially available filaments for FDM printing (Table 16) were prepared for immersion in SBF by cutting the filaments into 10 mm-long pieces.

SBF for the dissolution test was made following the same protocol as described in section 4.3.3.1.

4.6.2.2 Dissolution test

A part of the specimens of each group was immersed in 15 ml of SBF in plastic tubes for 14 days in a shaking water bath at 37 °C. The other part was kept dry. After the

dissolution test, the 10 mm specimens from both batches of groups were cut into 3.5 mm-long specimens.

4.6.2.3 Compression test

The 3.5 mm specimens (both dry and immersed in SBF for 14 days) were then tested in compression test. The testing protocol was based on the standard ISO 604:2002. A universal material testing machine LR30K Plus was used. Mechanical parameters (elastic modulus [GPa] and yielding strength [MPa]) were obtained from the test.

4.6.2.4 Modeling of the compression test by FEA

To validate the mechanical parameters of the polymers found in the compression test, a FE simulation of the test was performed in FEA software package Abaqus. Modeling was done in two dimensions as a general static problem. The supporting and loading pieces were modeled as rigid bodies.

4.6.2.5 Modeling of TTA implants by FEA

A preliminary design of the load-bearing part of the dog TTA implant was modeled under compression loading in FEA software package Abaqus. The mechanical properties obtained from the compression test of the group Dioxaprene were used. The virtual experimental setup mimicked that used by Etchepareborde and colleagues (Etchepareborde et al., 2014). The modeling was done as 3D general static problem.

4.6.3 Stage 3

4.6.3.1 Preparation of the experimental implants

Experimental implants consisted of a casing, an insert and bioactive filler (Table 16; Figure 18B). The parts of implants were printed on FDM printer using custom-written G-Codes. After assembling, the implants were sterilized using irradiation with gamma rays.

4.6.3.2 Dissolution test

Experimental implants were kept in sterile plastic tubes with 77 ml of SBF for 12 weeks in a shaking water bath at 37 °C. After 12 weeks, the remainders of

resorbed implants were collected and dried in desiccator. The implant remainders were assessed visually on macro- and microscopic levels.

4.6.3.3 Preparation of the control titanium implants

In addition to experimental implants (section 4.6.3.1), control implants were prepared for the *in vivo* experiment (Figure 18C). Titanium alloy was acquired from commercial human proximal humeral locking nails (Table 16). The design features simulated conventional existing TTA implants (*e.g.*, made by KYON AG, Switzerland). Sterilization was provided by autoclaving.

4.6.3.4 *In vivo* biocompatibility and osteointegration tests

Ten male New Zealand white rabbits were used. The animals were acclimatized for 14 days before the experiment and housed in standard individual plastic boxes. Day/night cycle was 12 h/12 h. The food was given *ad libitum*. 3R principles were followed, as well as the European Directive 2010/63/EU on the protection of animals used for scientific purposes and FELASA guidelines. The experiment was conducted at the National Veterinary School – Oniris in Nantes, France. The necessary permits were obtained.

During the surgery conducted under general anesthesia, analgesic and aseptic conditions, skin incisions followed by arthrotomy were made to access distal femoral condyles. In the condyles critical-sized cylindrical defects were drilled, irrigated with saline. Following the randomization plan, experimental (polymeric) or control (titanium) implants could be inserted into the defects, or the defects could be left empty (Table 15). The same operation was repeated bilaterally thus creating 20 defects in 10 animals.

Within 12-weeks follow-up period animals were inspected daily and subjected to an analgesia if necessary. The rabbits were euthanized on day 84 with general anesthesia. Thereafter, distal femoral condyles were obtained and fixed in 4.0 % Formol solution.

4.6.3.5 Micro-CT analysis of rabbit femora

Micro-CT (Skyscan 1072, Skyscan N.V., Belgium) and the software package Mimics 14 (Materialise N.V., Belgium) were employed to obtain 3D images of the condyles implanted with polymeric experimental implants or with empty defects. Subsequently, a total volume of interest (VOI) corresponding to the volume of initial defect and comprising three compartments (VOI-I…VOI-III) was defined in each

3D representation of a condyle to calculate a fraction of the conglomerate of new bone and remaining BG.

4.6.3.6 Histological analysis of rabbit femora

Two undecalcified sections with thickness 20 μm were cut from each condyle for histological examination (Daculsi et al., 2011; Voor et al., 2004; Zheng et al., 2014). The sections were made approximately along the central axis of the cylindrical defect to minimize geometrical biases. Von Kossa (VK) stain was used for one sample and hematoxylin and eosin (HE) stain was used for the other sample in each pair of histological samples. The samples were assessed visually with optical microscope and morphometrically by means of the computer program CT Analysis v.1.18.8.0 (Bruker Corporation, USA). For the morphometrical analysis a fraction of the conglomerate of the new bone and remaining BG was calculated in the region of interest (ROI) defined as a cross-section of the initial defect.

4.7 Statistical methods used in the research

When applicable, the numerical results of experiments were statistically analyzed. In all studies the same protocols were followed.

To identify the normality of the distribution of an independent data set, or of a difference between paired data sets, the Kolmogorov-Smirnov test was used.

If all data sets in an experiment were independent and distributed normally, the independent-samples *t*-test was applied to compare two data sets or one-way ANOVA with Tukey *post hoc* test was used to compare multiple sets.

If at least one of the independent data sets in an experiment was not distributed normally, the Mann-Whitney *U*-test was used for comparison of two data sets or Kruskall-Wallis test with pairwise comparison was applied in experiments with more than two groups.

If differences between paired data sets were distributed normally, paired-samples *t*-test was employed.

If at least one of the differences between paired sets of data did not follow normal distribution, Wilcoxon signed-ranks test was used.

The level of significance, *P*, was 0.05 in all statistical analyses. To report the normality in the present thesis, the following notion is used: “mean value (SD)” for normally distributed data set, or “median (25^{th} percentile, 75^{th} percentile)” for data sets whose distribution normality was not confirmed.

To perform statistical tests the software package SPSS Statistics 25 (IBM Corporation, USA) was used.

5 Results

5.1 Study I

5.1.1 Stage 1

5.1.1.1 Three-point bending test of FRC specimens

The group GFR-BisGMA/unidir demonstrated the highest flexural modulus compared to other groups ($P < 0.001$ in all cases). Flexural strength of GFR-BisGMA/sleeving was second high, with $P = 0.025$ compared to CFR-PEEK and $P = 0.018$ compared to bisGMA/short (ranked third and fourth however without significant difference to each other), and with $P < 0.001$ with respect to bisGMA/sheet (Table 17, Figure 19A).

In yield strength, the ranking was the same as in flexural modulus, with the exception for CFR-PEEK and bisGMA/short which swapped their places, with GFR-BisGMA/unidir having significance $P < 0.001$ to any other group. However, GFR-BisGMA/sleeving was significantly stronger only compared to bisGMA/short ($P = 0.014$) and bisGMA/sheet ($P = 0.02$). In all other pairs there were no significant differences (Table 17, Figure 19B).

Ultimate strength again was the highest in GFR-BisGMA/unidir and the lowest in the GFR-BisGMA/sheet groups, however significant difference was confirmed only compared to GFR-BisGMA/short ($P = 0.005$) and GFR-BisGMA/sheet ($P < 0.001$). Also, the difference between CFR-PEEK, ranked second, and GFR-BisGMA/sheet was significant ($P = 0.009$; Table 17, Figure 19C).

The highest strain at the ultimate strength was demonstrated by CFR-PEEK ($P < 0.001$ compared to ranked fourth GFR-BisGMA/sleeving and $P < 0.001$ with respect to GFR-BisGMA/short ranked the last one). GFR-BisGMA/unidir was on the second place, having $P = 0.001$ with GFR-BisGMA/sleeving and $P < 0.001$ with GFR-BisGMA/short. The group GFR-BisGMA/sheet, being on the third place, had the same $P = 0.001$ and $P < 0.001$ with GFR-BisGMA/sleeving and GFR-BisGMA/short, correspondingly. Finally, the difference between GFR-

BisGMA/sleeving and GFR-BisGMA/short had significance level $P = 0.03$ (Table 17, Figure 19D).

5.1.1.2 Modeling of the three-point bending test by FEA

To compare results of FEA, the load-displacement curves obtained in FEA were superimposed on the corresponding graphs obtained from the mechanical testing. This showed good prediction of the linear part of the response, however on the inelastic portion the predicted stiffness was higher than the realistic one with the exception for GFR-BisGMA/short.

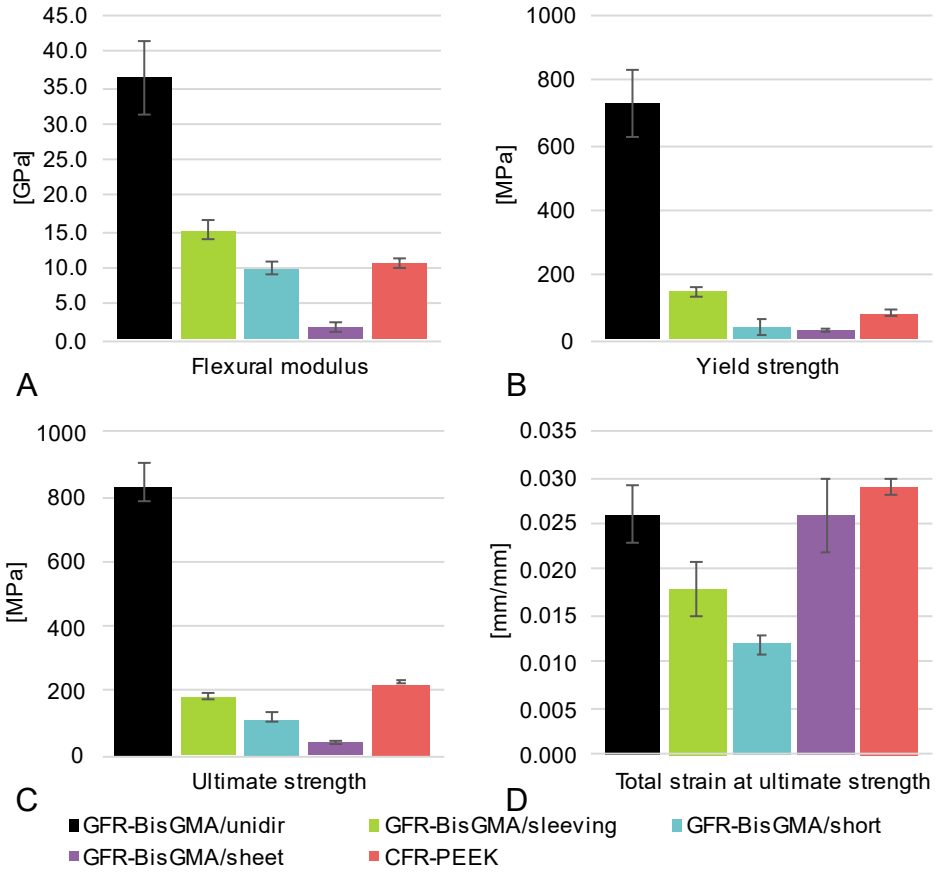

Figure 19. Results of the three-point bending tests conducted in Study I: flexural modulus (A), yield strength (B), ultimate strength (C), strain at ultimate strength (D).

Table 17. Results of the three-point bending tests conducted in Study I.

Group name	Flexural modulus [MPa][1]	Yield strength [MPa][1]	Ultimate strength [MPa][2]	Total strain at ultimate strength [mm/mm][1]
GFR-BisGMA/unidir	36.4 (5.2)	732 (103)	831 (789, 904)	0.026 (0.003)
GFR-BisGMA/sleeving	15.3 (1.2)	149 (17)	178 (176, 193)	0.018 (0.003)
GFR-BisGMA/short	10.0 (1.1)	43 (25)	114 (103, 135)	0.012 (0.001)
GFR-BisGMA/sheet	1.8 (0.5)	28 (7)	41 (36, 47)	0.026 (0.004)
CFR-PEEK	10.6 (0.8)	83 (9)	223 (220, 236)	0.029 (0.001)
Stainless steel 316L[3]	210.0	896	1006	0.047

[1] The data presented in the format: mean (SD).
[2] The data presented in the format: median (25^{th} percentile, 75^{th} percentile).
[3] The material was not tested, data was found in the literature and used in the subsequent FEA.
Modified from Study I.

5.1.2 Stage 2

5.1.2.1 Four-point bending test of fracture fixation plates

The slope of the load-displacement curve was the highest in the Stainless Steel group with the significance level $P < 0.001$ with all other groups with the exception for GFR-BisGMA/unidir. The value in the group GFR-BisGMA/unidir was significantly higher than in GFR-BisGMA/sleeving ($P = 0.002$), GFR-BisGMA/short and GFR-BisGMA/sheet ($P < 0.001$). In the group GFR-BisGMA/sleeving, the slope was higher than in GFR-BisGMA/short ($P = 0.012$), CFR-PEEK and GFR-BisGMA/sheet ($P < 0.001$). In the group GFR-BisGMA/short, the slope was insignificantly higher than in CFR-PEEK and higher than in GFR-BisGMA/sheet ($P = 0.001$). Slope in CFR-PEEK was insignificantly greater than in GFR-BisGMA/sheet (Table 18, Figure 20A).

The equivalent bending stiffness was the highest also in the Stainless Steel group with $P < 0.001$ in all pairs excepting for GFR-BisGMA/unidir. In the latter group, the value was significantly higher than in GFR-BisGMA/sleeving ($P = 0.002$) and in the resting groups ($P < 0.001$). GFR-BisGMA/sleeving was stiffer than GFR-BisGMA/short ($P = 0.012$) and CFR-PEEK and GFR-BisGMA/sheet ($P < 0.001$).

GFR-BisGMA/short was stiffer than GFR-BisGMA/sheet ($P = 0.001$; Table 18, Figure 20B).

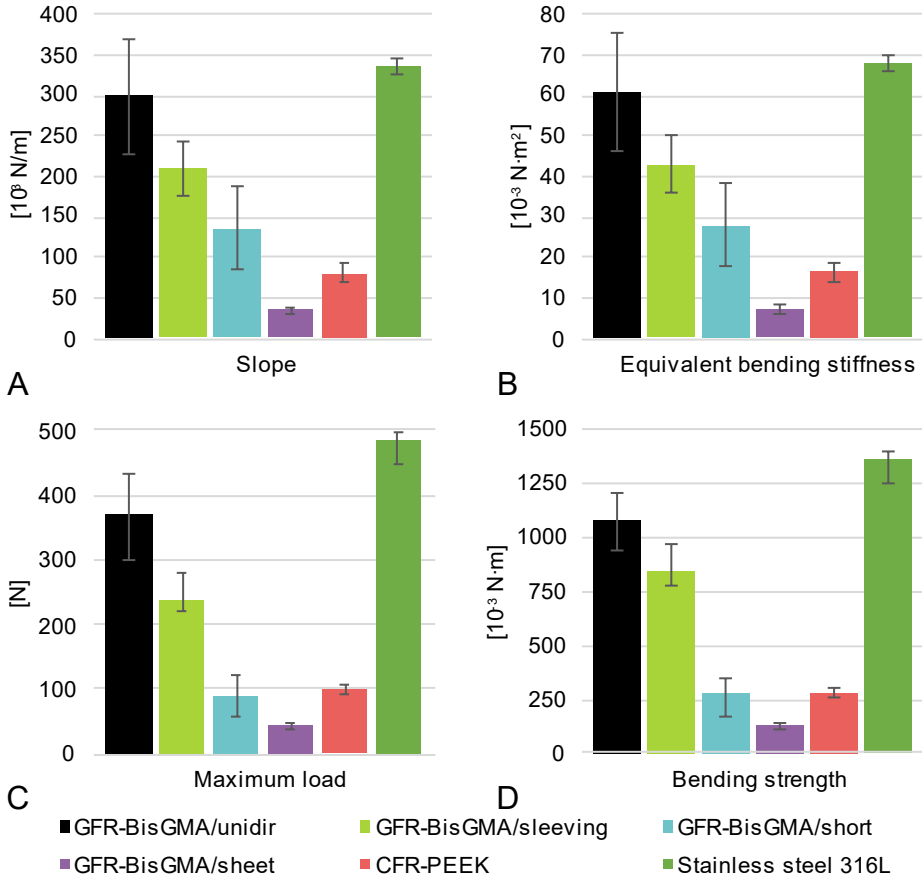

Figure 20. Results of the four-point bending tests conducted in Study I: curve slope (A), equivalent bending stiffness (B), maximum load (C), bending strength (D).

The highest maximum load was achieved by Stainless steel with significance level compared to other groups: GFR-BisGMA/short $P = 0.006$, CFR-PEEK $P = 0.013$ and GFR-BisGMA/sheet $P < 0.001$. The group GFR-BisGMA/unidir was ranked second and had statistically significant difference with GFR-BisGMA/sheet solely ($P = 0.002$). The group GFR-BisGMA/sleeving demonstrated the maximum load significantly higher than GFR-BisGMA/sheet ($P = 0.009$). There was no significant difference between the other groups (Table 18, Figure 20C).

Bending strength achieved the highest value in Stainless Steel (insignificantly greater than in GFR-BisGMA/unidir and GFR-BisGMA/sleeving, $P = 0.017$

compared to CFR-PEEK, $P = 0.013$ compared to GFR-BisGMA/short and $P < 0.001$ compared to GFR-BisGMA/sheet). GFR-BisGMA/unidir was significantly stronger than GFR-BisGMA/sheet ($P = 0.004$) and insignificantly stronger than GFR-BisGMA/sleeving, CFR-PEEK and GFR-BisGMA/short. The group GFR-BisGMA/sleeving was statistically insignificantly stronger than CFR-PEEK and GFR-BisGMA/short, while significance level in comparison with GFR-BisGMA/sheet was $P = 0.004$ (Table 18, Figure 20D).

Table 18. Results of the four-point bending tests conducted in Study I.

Group name	Slope [10^3 N/m]	Equivalent bending stiffness [10^{-3} N·m^2]	Maximum load [N]	Bending strength [10^{-3} N·m]
GFR-BisGMA/ unidir	299 (72)	61.0 (14.7)	370 (298, 432)	1081 (939, 1210)
GFR-BisGMA/sleeving	210 (33)	43.0 (6.8)	239 (221, 279)	835 (773, 975)
GFR-BisGMA/short	136 (51)	27.8 (10.4)	91 (56, 124)	283 (171, 347)
GFR-BisGMA/sheet	35 (4)	7.2 (0.9)	45 (39, 47)	125 (108, 132)
CFR-PEEK	80 (12)	16.4 (2.5)	100 (92, 107)	280 (257, 300)
Stainless steel 316L	334 (10)	68.2 (2.0)	485 (448, 498)	1358 (1254, 1395)

Modified from Study I.

5.1.2.2 Modeling of the four-point bending test by FEA

The load-displacement curves achieved in FEA were superimposed with the ones obtained in the mechanical test. The best overlapping of curves was demonstrated in groups GFR-BisGMA/short and CFR-PEEK. In the other groups, the predicted response could be as stiffer (Stainless Steel, GFR-BisGMA/unidir, GFR-BisGMA/sleeving), as lower (GFR-BisGMA/sheet) than in actual testing.

The correlation analysis confirmed, in general, a good correlation between the ranking of the results of the groups in the mechanical test and in FEA using actual dimensions of plates (Table 19). For the slope and equivalent bending stiffness, the correlation was very strong ($R_s = 1.000$). For the bending strength the correlation was lower but still significant ($R_s = 0.829$, $P = 0.042$). Only for the maximum load the correlation was not significant ($R_s = 0.771$, $P = 0.072$).

Table 19. Results of the modeling of the four-point bending tests conducted in Study I.

Group name	Slope [10^3·N/m]	Equivalent bending stiffness [10^{-3} N·m^2]	Maximum load [N]	Bending strength [10^{-3} N·m]	Design
GFR-BisGMA/ unidir	525 (176)[1]	107.2 (176)	738 (199)	2067 (191)	2
	165 (55)[2]	33.7 (55)	235 (64)	658 (61)	
GFR-BisGMA/sleeving	368 (175)	75.2 (175)	408 (171)	1427 (171)	2
	61 (29)	12.4 (29)	83 (35)	289 (35)	
GFR-BisGMA/short	120 (88)	24.4 (88)	90 (99)	253 (89)	2
	38 (28)	7.7 (28)	28 (31)	80 (28)	
GFR-BisGMA/sheet	11 (31)	2.3 (32)	13 (29)	35 (28)	1
	6 (17)	1.2 (17)	6 (13)	18 (14)	
CFR-PEEK	68 (85)	13.8 (84)	83 (83)	231 (83)	1
	30 (38)	6.1 (37)	37 (37)	103 (37)	
Stainless steel 316L	530 (159)	108.3 (159)	390 (80)	1091 (80)	1
Spearman correlation with experimental results (by each parameter)	1.000	1.000	0.771 (P = 0.072)	0.829 (P = 0.042)	N/A

[1] In the upper row, the data for the model with averaged actual thickness are given.
[2] In the lower row, the data for the modeling with nominal thickness (1.5 mm) are given.
In the parentheses the percentage to the obtained experimental value is given.
Modified from Study I.

5.1.2.3 Analysis of the effect of plate thickness and curvature on the stiffness

The results of the test (Table 20) showed that for one and the same design and material, the raise of the obtained value could achieve 233 %, while the growth in the thickness was only 54 %.

Table 20. Results of the analysis of the effect of plate thickness and curvature conducted in Study I.

Group name	Difference in the parameter between the lowest and the highest thicknesses in one model [%]		
	Cross-section area	Slope of the linear part of the load-displacement curve	Maximum theoretical load
GFR-BisGMA/unidir	64 / 54[1]	231 / 233	176 / 177
GFR-BisGMA/sleeving	64 / 54[1]	128 / 145	164 / 165
GFR-BisGMA/short	64 / 54[1]	211 / 217	173 / 173
GFR-BisGMA/sheet	64 / 54[1]	134 / 151	165 / 166
CFR-PEEK	64 / 54[1]	220 / 220	189 / 186
Stainless steel 316L	64 / 54[1]	201 / 207	187 / 182

[1] In the numerator: value for the flat plate; in the denominator: value for the curved plate.
Modified from Study I.

5.2 Study II

5.2.1 Stage 1

5.2.1.1 Visual description of the synthesized polymers

PLAMA resins in both variants (molecular mass 500 and 1000) were colorless transparent viscous liquids, visually indistinguishable from each other. The components of the photoinitiating system added yellow color to the resins so that PLAMA became indistinguishable from the control bisGMA resin either.

After light curing, both PLAMA variants obtained transparent glassy solid state with yellow color, visually lighter in PLAMA-1000 than in PLAMA-500 or in solidified bisGMA. Subjectively, solidified PLAMA-1000 was remarkably less rigid, less hard and less elastic and more flexible, having also some ductility, thus resembling the mechanical behavior of hard elastomers.

5.2.1.2 FTIR and ^{1}H-NMR spectra of PLAMA

Typical values of observed spectra peaks for PLAMA-500 and PLAMA-1000 are reported in Table 21.

Table 21. Control FTIR and ^{1}H-NMR spectra peaks used for synthesis of PLAMA in Study II.

Group name	FTIR Wavenumbers ν [cm^{-1}][1]	^{1}H-NMR Chemical shifts δ [ppm][2]
PLAMA-500	3383, 2991, 2961, 2945, 2899, 1722, 1636, 1538, 1455, 1256, 1195	6.13, 5.60, 6.06-6.29, 4.37-4.40, 4.18-4.23, 3.60-3.63, 1.96, 1.73, 1.41-1.60, 1.25, 0.88
PLAMA-1000	3415, 2992, 2959, 2945, 2901, 1754, 1636, 1534, 1453,1260, 1188	6.12, 5.60, 6.06-6.23, 4.36-4.39, 4.17-4.23, 3.49-3.61, 1.96, 1.72, 1.41-1.60, 1.26, 0.87-0.88

[1] Neat spectra.
[2] Solvent: $CDCl_3$, frequency: 400 MHz.
Modified from Study II.

5.2.1.3 Degree of conversion

Both modifications of PLAMA demonstrated significantly higher DC at all time points (immediately after curing and one, three, seven and 28 days after curing) compared to bisGMA with $P < 0.001$ for both PLAMA after 24 hours and $P = 0.011$ for PLAMA-500 and $P = 0.048$ for PLAMA-1000 on day 28 (Table 22; Figure 21). Within the first 24 hours after the light curing, all groups had significant increase of DC: $P = 0.007$, $P = 0.001$ and $P = 0.002$ for PLAMA-500, PLAMA-1000 and bisGMA, correspondingly. The PLAMA-500 samples showed significant increase ($P = 0.041$) also in the next 48 hours, while post-curing in the PLAMA-1000 and bisGMA groups further remained insignificant. Final spectra are shown in Figure 22.

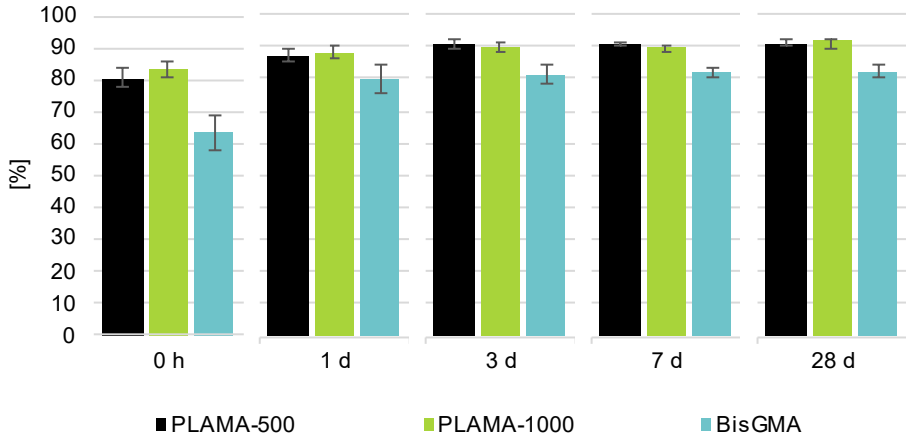

Figure 21. Degree of conversion by time points.

Table 22. Results of the measurement of degree of conversion of polymers conducted in Study II.

Group name	DC after light-curing [%]	DC obtained due to the post-curing on day [%]			
		1	3	7	28
PLAMA-500	80.74 (3.10)[1]	87.30 (1.61)	90.58 (1.51)	90.76 (0.60)	90.70 (90.20, 91.90)[2]
PLAMA-1000	83.14 (2.42)	88.16 (2.26)	89.62 (1.38)	89.38 (0.99)	92.20 (89.75, 92.35)
BisGMA	63.00 (5.49)	79.88 (4.67)	81.20 (2.82)	82.12 (1.76)	81.50 (80.65, 84.20)

[1] The data presented in the format: mean (SD).
[2] The data presented in the format: median (25th percentile, 75th percentile).
Modified from Study II.

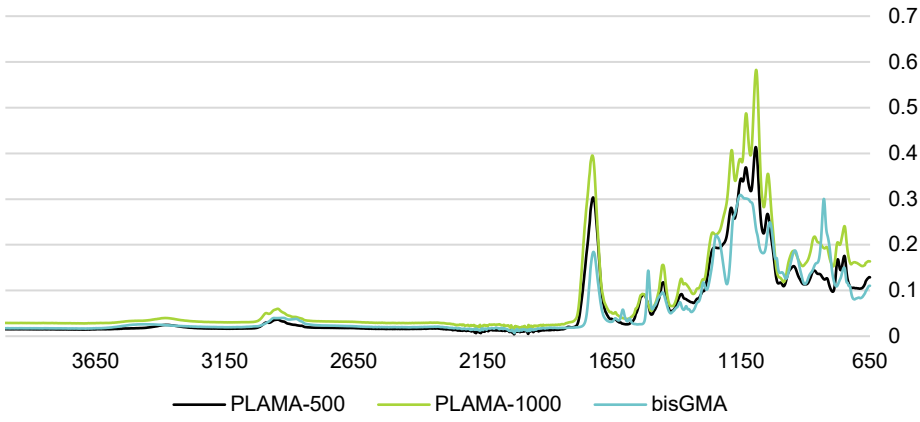

Figure 22. FTIR spectra obtained in fully cured specimens on day 28 in Study II.

5.2.2 Stage 2

5.2.2.1 Tensile test

All groups except for PLDL demonstrated non-linear stress-strain curves. Curves of some specimens in the PLAMA-500 groups had a softening segment unlike bisGMA. The curve of PLAMA-1000 did not have visible linear segment. Surprisingly, the specimens from the PLDL group broke sufficiently earlier than expected without reaching the non-linear segment.

Nevertheless, the highest elastic modulus was obtained by PLDL, with significance level $P = 0.015$ compared to the bisGMA group and $P < 0.001$ compared to the other two groups. PLAMA-500 was slightly less stiff than bisGMA,

and both were significantly stiffer than PLAMA-1000 ($P < 0.001$; Table 23, Figure 23A).

The calculated Poisson's ratio was the highest in the PLAMA-1000 group ($P = 0.018$ compared to PLAMA-500, $P = 0.035$ compared to bisGMA and $P < 0.001$ compared to PLDL). There was no significant difference in the other pairwise comparisons (Table 23, Figure 23B).

The achieved variances in the UTS were narrow, providing strong significance level $P < 0.001$ in all possible pairwise comparisons. In the groups PLAMA-1000 and bisGMA the UTS point coincided with the fracture point on the stress-strain plot. Due to the softening observed in PLAMA-500, its UTS and fracture occurred at different moments in time. The groups were ranked by the UTS value as follows, starting from the strongest one: bisGMA, PLAMA-500, PLDL, PLAMA-1000 (Table 23, Figure 23C).

There were no significant differences between the strains at UTS point in the groups PLAMA-500, PLAMA-1000 and bisGMA, however the PLAMA-1000 specimens had the highest average strain, followed by PLAMA-500 and bisGMA. The group PLDL had the lowest strain with significance level $P < 0.001$ with all the other materials (Table 23, Figure 23D).

Table 23. Results of the tensile tests conducted in Study II.

Group name	Modulus of elasticity [GPa]	Poisson's ratio	Ultimate tensile strength [MPa]	Strain at ultimate tensile strength [mm/mm]
PLAMA-500	3.4 (0.2)	0.27 (0.04)	68.5 (1.9)	0.0359 (0.0031)
PLAMA-1000	0.9 (0.1)	0.39 (0.03)	14.0 (1.7)	0.0344 (0.0118)
bisGMA	4.0 (0.2)	0.29 (0.05)	84.2 (6.0)	0.0305 (0.0040)
PLDL	5.2 (1.1)	0.20 (0.09)	52.4 (6.9)	0.0110 (0.0027)

The data presented in the format: mean (SD).
Modified from Study II.

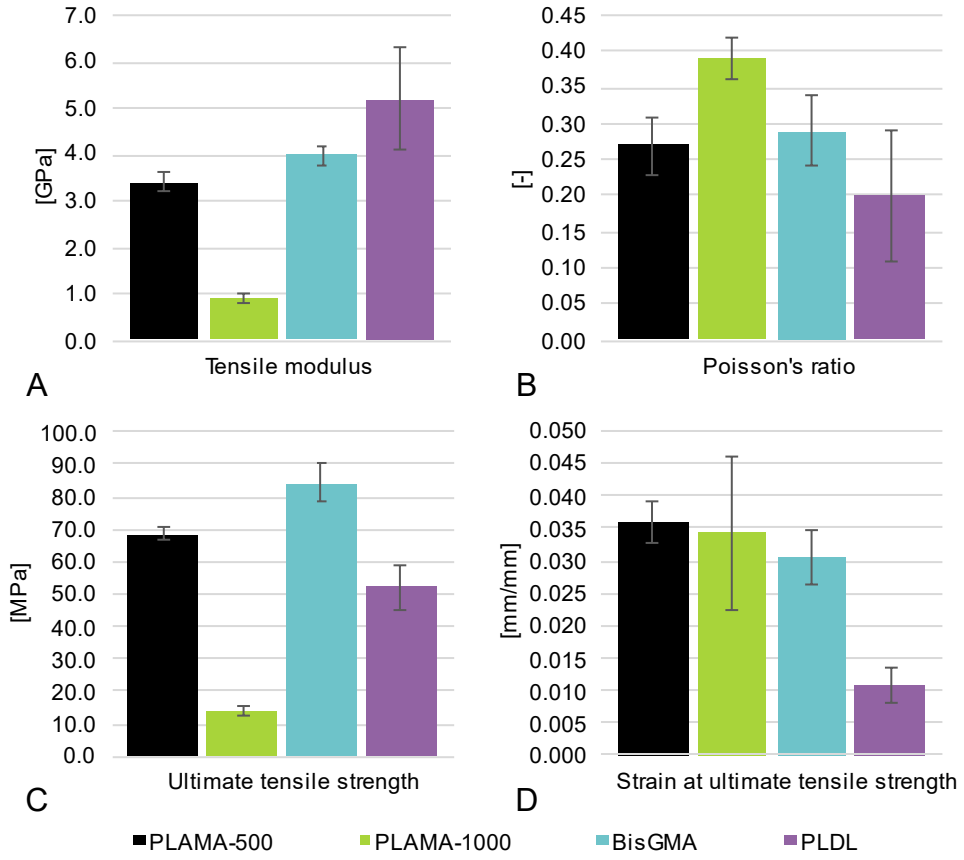

Figure 23. Results of the tensile tests conducted in Study II: tensile modulus (A), Poisson's ratio (B), ultimate tensile strength (C), strain at ultimate strength (D).

5.2.2.2 Thermomechanical analysis

Averaged values of the glass transition temperature were in line with expectations for similar types of materials, with a lower value for more flexible PLAMA-1000 and the highest value for the stiffest of the studied thermosets, bisGMA (Table 24). The value obtained for PLDL was similar to the typically reported ones (Table 4). The results of the multi-cyclic TMA (Table 25) were similar to the single-cyclic test.

Table 24. Results of the single-cyclic thermomechanical analysis conducted in Study II.

Group name	Coefficient of thermal expansion [10^{-6}/°C]		Glass transition temperature [°C]
	At room temperature[1]	At body temperature[2]	
PLAMA-500	90.6	131.2	38.1
PLAMA-1000	146.2	179.9	20.8
bisGMA	58.9	75.0	109.8
PLDL	82.9	106.9	52.5

[1] 18 - 22 °C.
[2] 35 - 45 °C.
The data presented as arithmetic means for three specimens (five specimens for PLDL).
Modified from Study II.

Table 25. Results of the multi-cyclic thermomechanical analysis conducted in Study II.

Group name	Coefficient of thermal expansion [10^{-6}/°C]		Glass transition temperature [°C]
	Room temperature[1]	Body temperature[2]	
PLAMA-500	121.5	155.9	42.7
PLAMA-1000	152.2	179.6	11.8
bisGMA	62.5	72.6	113.6
PLDL	84.1[3]	125.8	56.7

[1] 18 - 22 °C.
[2] 35 - 45 °C.
[3] The average for two runs due to one incorrect measurement.
The data presented as arithmetic means for three runs.
Modified from Study II.

5.2.3 Stage 3

5.2.3.1 Dissolution test

The group PLAMA-500 did not demonstrate visible traces of material dissolution after 12 weeks in SBF. In contrast to that, PLAMA-1000 remarkably changed and had visually detected signs of dissolution such as cavities.

The mass losses (Table 26) were significant in both groups compared to the initial mass of the specimens ($P = 0.008$ and $P < 0.001$ for PLAMA-500 and PLAMA-1000, correspondingly). In the beginning of the test the masses in both groups were identical, while the losses in PLAMA-1000 were significantly greater than in PLAMA-500 ($P < 0.001$; Figure 24A).

The pH value measured in the tubes with specimens after the dissolution test confirmed significant drop in the group PLAMA-1000 ($P < 0.001$) compared to the clean SBF, while in PLAMA-500 the pH value decreased insignificantly (Table 26). Correspondingly, the final pH was significantly lower in PLAMA-1000 compared with the corresponding measurements in PLAMA-500 (Figure 24B).

Table 26. Results of the dissolution test conducted in Study II.

Group name	Mass [g]		pH value	
	Before the test	After the test	Before the test	After the test
PLAMA-500	0.133 (0.003)	0.129 (0.003)	7.51[1]	7.52 (0.05)
PLAMA-1000	0.132 (0.002)	0.119 (0.002)	7.51[1]	7.20 (0.02)

[1] Measured in bulk.
The data presented in the format: mean (SD).
Modified from Study II.

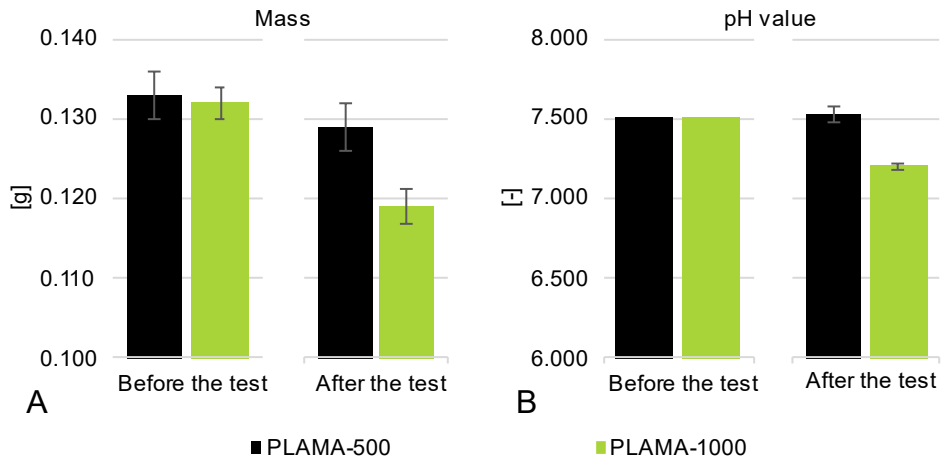

Figure 24. Results of the dissolution test conducted in Study II: mass losses (A), changes in pH value of SBF (B).

5.2.3.2 Three-point bending test

The flexural behavior of dry specimens was in general in line with the results of the tensile test (Table 27). Some specimens in the PLAMA-1000 group in the available experimental setup did not break before the testing machine reached the displacement limit. After the dissolution test, both materials became more brittle.

Both before and after the test, PLAMA-500 was significantly stiffer ($P < 0.001$) and stronger ($P < 0.001$) than PLAMA-1000. After the dissolution (Table 28), both materials lost significantly as in modulus ($P < 0.001$ for both groups), as in the strength ($P = 0.002$ and $P = 0.049$, correspondingly; Figure 25A, B).

The strain at UTS decreased in both materials after the dissolution test, however in both cases it was higher in PLAMA-1000 than in PLAMA-500 ($P < 0.001$ and $P = 0.017$). The decrease within each group was also significant, with $P = 0.013$ for

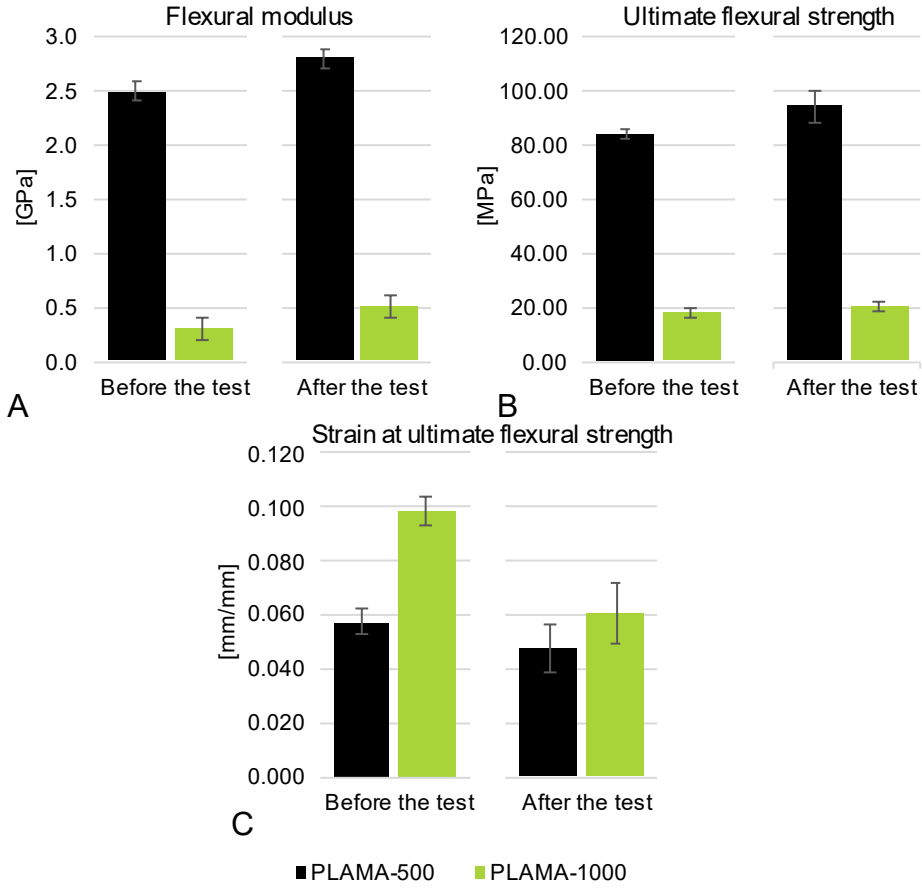

Figure 25. Results of the three-point bending test conducted in Study II: flexural modulus (A), ultimate flexural strength (B), strain at ultimate flexural strain (C).

PLAMA-500 and $P < 0.001$ for PLAMA-1000 (Figure 25C). All specimens in PLAMA-1000 broke after the dissolution test, unlike the dry specimens.

Table 27. Results of the three-point bending test of dry specimens conducted in Study II.

Group name	Flexural modulus [GPa]	Ultimate flexural strength [MPa]	Strain at ultimate flexural strength [mm/mm]
PLAMA-500	2.5 (0.1)	84.4 (1.6)	0.0576 (0.0052)
PLAMA-1000	0.3 (0.1)	18.0 (2.0)	0.0986 (0.0053)

The data presented in the format: mean (SD).
Modified from Study II.

Table 28. Results of the three-point bending test of the specimens after the dissolution test conducted in Study II.

Group name	Flexural modulus [GPa]	Ultimate flexural strength [MPa]	Strain at ultimate flexural strength [mm/mm]
PLAMA-500	2.8 (0.1)	94.2 (6.1)	0.0476 (0.0085)
PLAMA-1000	0.5 (0.1)	20.2 (2.0)	0.0610 (0.0111)

The data presented in the format: mean (SD).
Modified from Study II.

5.2.4 Stage 4

5.2.4.1 Cell morphology test

Visual microscopic evaluation confirmed presence of angular-shaped cells on specimens in all experimental groups (Figure 26). Stress fibers in cells were observed.

The surface area did not significantly vary between the groups and within each group at all time points, with the exception for PLAMA-500, in which significant growth was detected between the points four and eight hours ($P = 0.015$; Table 29, Figure 28).

Some tendency to increase was observed in the aspect ratio in all groups excepting for PLDL, however statistical significance for that was not confirmed. Differences among the groups at time points were also insignificant, with the

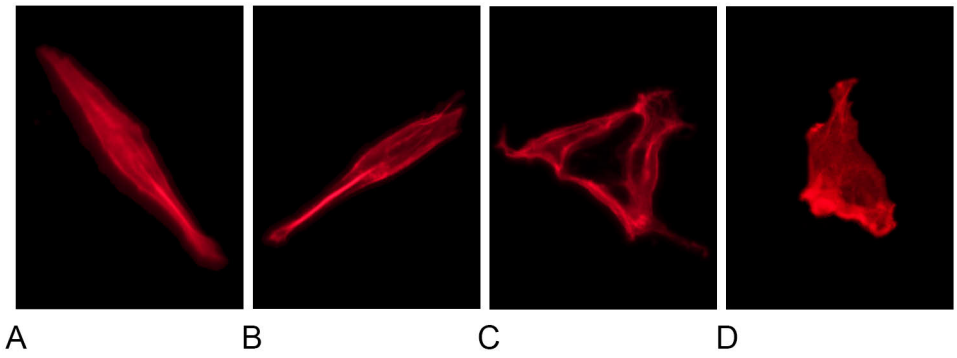

Figure 26. Examples of MG-63 cells observed on the material specimens in Study II: PLAMA-500 (A), PLAMA-1000 (B), PLDL (C), Stainless Steel (D). Image modified from Study II.

exception for a sporadically observed significant difference between PLAMA-1000 and PLDL at eight hours (Table 29, Figure 27).

5.2.4.2 Cell proliferation test

The average absorbance at 450 um was similar in all groups at the first time point (24 h) with the exception for the pair PLDL and PLAMA-1000, in which the value of the PLDL group was higher ($P = 0.007$). After 96 h, the absorbance value significantly grew in all groups with the levels of significance $P < 0.001$ for stainless steel, $P = 0.015$ for PLDL, $P = 0.029$ for PLAMA-500 and $P = 0.020$ for PLAMA-1000. Among the groups, the highest absorbance was achieved by stainless steel, followed by PLDL with insignificant difference; the absorbance in PLAMA-500 was the third ($P = 0.022$ compared to stainless steel). The lowest absorbance was demonstrated by PLAMA-1000 with significant difference with stainless steel ($P < 0.001$) and PLDL ($P = 0.023$; Table 30, Figure 29).

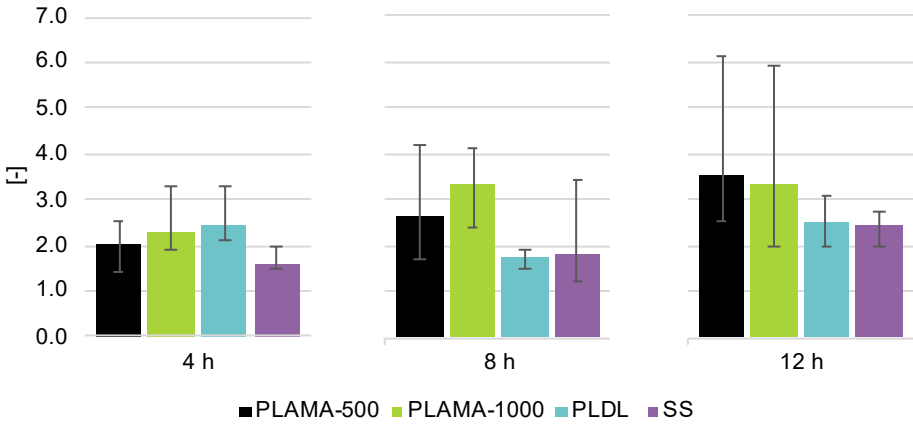

Figure 27. Average aspect ratio of the cells obtained in the morphology test conducted in Study II.

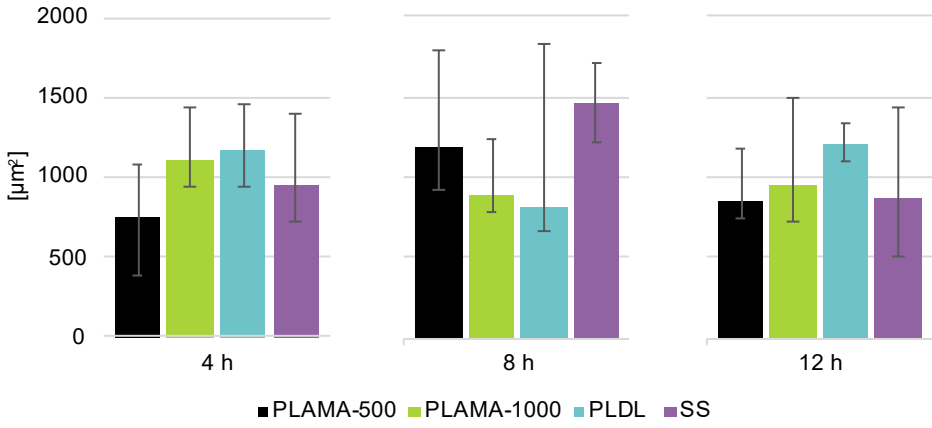

Figure 28. Average surface area of the cells obtained in the morphology test conducted in Study II.

Table 29. Results of the cell morphology test conducted in Study II.

Group name	Surface area [µm²]			Aspect ratio		
	4 h	8 h	12 h	4 h	8 h	12 h
PLAMA-500	762 (385, 1076)	1183 (911, 1781)	855 (740, 1177)	2.0 (1.4, 2.5)	2.6 (1.7, 4.2)	3.5 (2.5, 6.1)
PLAMA-1000	1116 (934, 1446)	898 (789, 1238)	944 (722, 1500)	2.3 (1.9, 3.3)	3.3 (2.4, 4.1)	3.3 (2.0, 5.9)
PLDL	1176 (934, 1462)	810 (667, 1828)	1203 (1104, 1338)	2.4 (2.1, 3.3)	1.7 (1.5, 1.9)	2.5 (2.0, 3.1)
SS	957 (724, 1406)	1452 (1207, 1709)	872 (500, 1427)	1.6 (1.5, 2.0)	1.8 (1.2, 3.4)	2.4 (2.0, 2.7)

The data presented in the format: median (25th percentile, 75th percentile).
Modified from Study II.

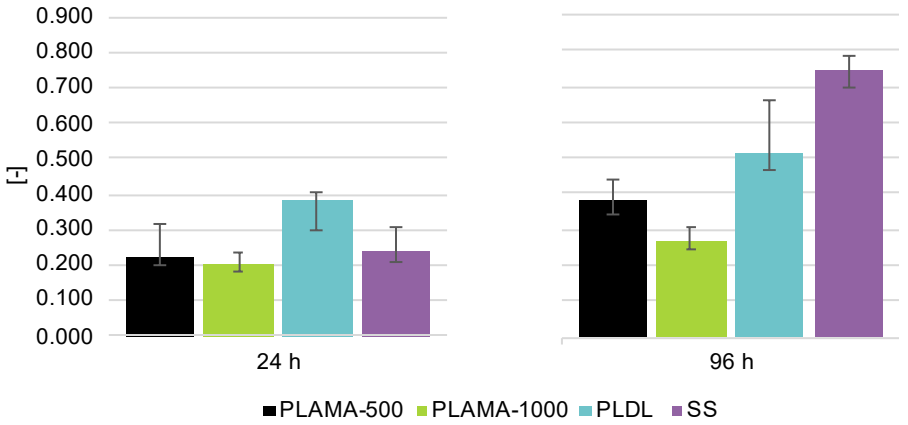

Figure 29. Results of the cell proliferation test conducted in Study II.

Table 30. Results of the cell proliferation test conducted in Study II.

Group name	Absorbance at 450 μm	
	After 24 h	After 96 h
PLAMA-500	0.223 (0.202, 0.314)	0.380 (0.341, 0.439)
PLAMA-1000	0.203 (0.179, 0.234)	0.271 (0.241, 0.303)
PLDL	0.380 (0.294, 0.402)	0.512 (0.466, 0.660)
SS	0.243 (0.208, 0.305)	0.748 (0.695, 0.786)

The data presented in the format: median (25^{th} percentile, 75^{th} percentile).
Modified from Study II.

5.3 Study III

5.3.1 Stage 1

5.3.1.1 Three-point bending test

The test showed substantial increase in the ultimate load for the prototype plates reinforced with TFP preforms with respect to the unreinforced specimens. Enclosing the TFP reinforced plates into the PC shell additionally boosted the mechanical capabilities of the reinforced plates (Table 31, Figure 30).

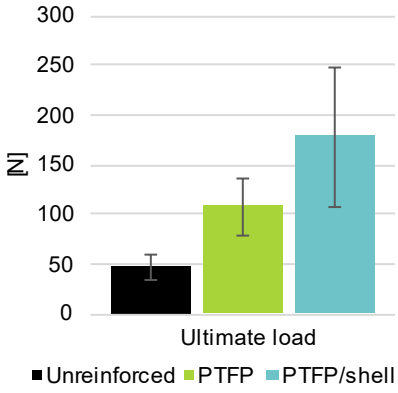

Figure 30. Results of the three-point bending test of fracture fixation plates conducted in Study III.

Table 31. Results of the three-point bending test of fracture fixation plates conducted in Study III.

Group name	Ultimate load [N]
Unreinforced	46.8 (13.0)
PTFP	107.5 (29.2)
PTFP/shell	177.8 (70.7)

The data presented in the format: mean (SD).
Modified from Study III.

5.3.2 Stage 2

5.3.2.1 Four-point bending test of plates

The Unidir group expectedly demonstrated the highest slope of the load-displacement curve compared to any other group ($P < 0.001$). The value of the plots' slope was second high in OTFP/PLA, which in turn was significantly higher than in OTFP/G and PTFP with the levels of significance $P < 0.001$ and $P = 0.044$, and no other differences were statistically significant (Table 32, Figure 31A).

In the equivalent bending stiffness, the highest result was also achieved by the group Unidir with the level of significance $P < 0.001$ with any other group. The plates in the group OTFP/PLA were significantly stiffer than in groups OTFP/G and PTFP ($P < 0.001$ and $P = 0.044$, correspondingly), while the other pairwise comparisons revealed no significant differences in the bending stiffness (Table 32, Figure 31B).

In maximum load, the Unidir group was on the first place showing significantly greater value than the other groups ($P = 0.008$). Other significant differences were found between PTFP, ranked second, and OTFP/G ($P = 0.016$) and between OTFP/PLA, ranked third, and OTFP/G ($P = 0.047$; Table 32, Figure 31C).

The group Unidir was significantly stronger than any other group in equivalent bending strength ($P = 0.008$). The group PTFP was significantly stronger than the groups OTFP/PLA and OTFP/G ($P = 0.008$ for both). The group OTFP/PLA was significantly stronger than OTFP/G. In the other pairs no statistically significant differences were discovered (Table 32, Figure 31D).

Table 32. Results of the four-point bending test of fracture fixation plates conducted in Study III.

Group name	Slope [10^3 N/m]	Equivalent bending stiffness [10^{-3} N·m^2]	Maximum load [N]	Bending strength [10^{-3} N·m]
Unidir	325.2 (18.1)[1]	71 (4)	373.9 (368.0, 426.1)[2]	1030 (1020, 1180)
PTFP	88.4 (14.2)	19 (3)	222.8 (183.8, 230.5)	630 (610, 800)
OTFP/G	72.4 (12.0)	16 (3)	124.6 (123.2, 134.7)	343 (340, 372)
OTFP/PLA	113.4 (7.4)	25 (2)	162.7 (152.7, 165.1)	450 (420, 460)

[1] The data presented in the format: mean (SD).
[2] The data presented in the format: median (25th percentile, 75th percentile).
Modified from Study III.

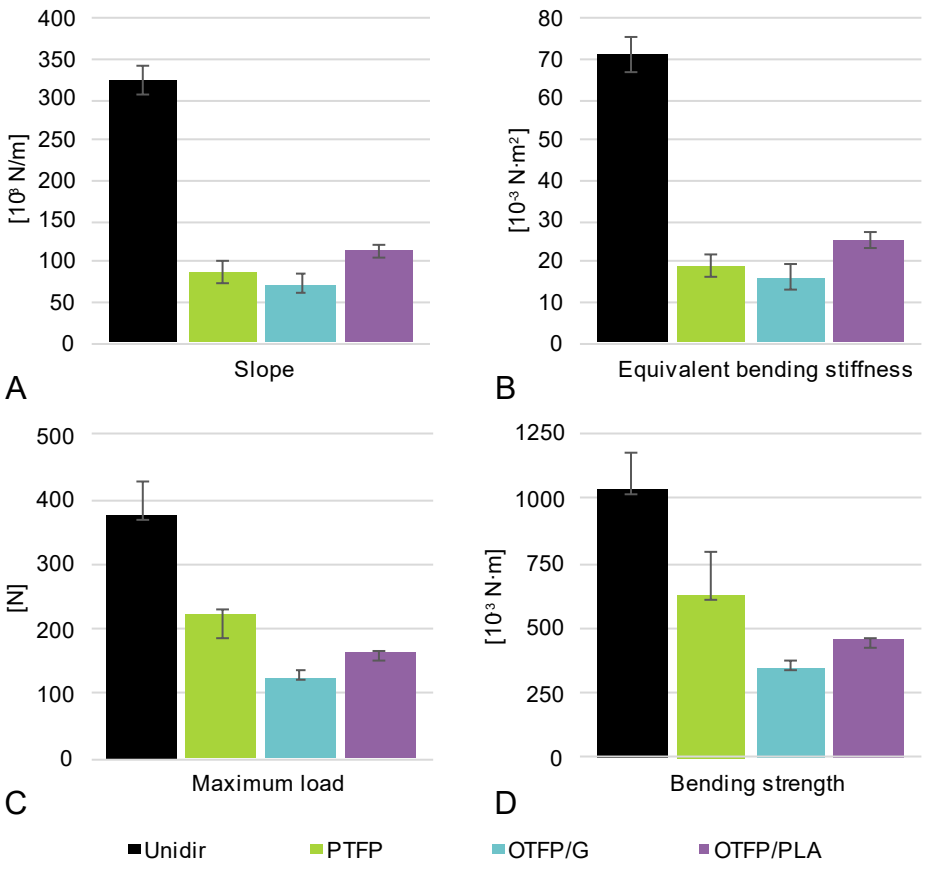

Figure 31. Results of the four-point bending test of fracture fixation plates conducted in Study III: curve slope (A), equivalent bending stiffness (B), maximum load (C), bending strength (D).

5.3.2.2 Four-point bending test of bone specimens

In none of the groups, none of the measured mechanical parameter had statistically significant difference in pairwise comparisons (Table 33, Figure 32).

Table 33. Results of the four-point bending of bone specimens conducted in Study III.

Group name	Slope [10^3 N/m]	Equivalent bending stiffness [10^{-3} N·m^2]	Maximum load [N]	Bending strength [10^{-3} N·m]
Unidir	177.0 (31.0)	310 (50)	225.8 (83.6)	1250 (460)
PTFP	135.1 (42.2)	240 (70)	266.3 (30.4)	1470 (170)
OTFP/G	218.8 (62.5)	380 (110)	262.4 (55.1)	1450 (300)
OTFP/PLA	180.8 (37.3)	320 (70)	234.8 (79.8)	1300 (440)
Intact bones	167.4 (43.6)	290 (80)	308.3 (54.2)	1700 (300)

The data presented in the format: mean (SD).
Modified from Study III.

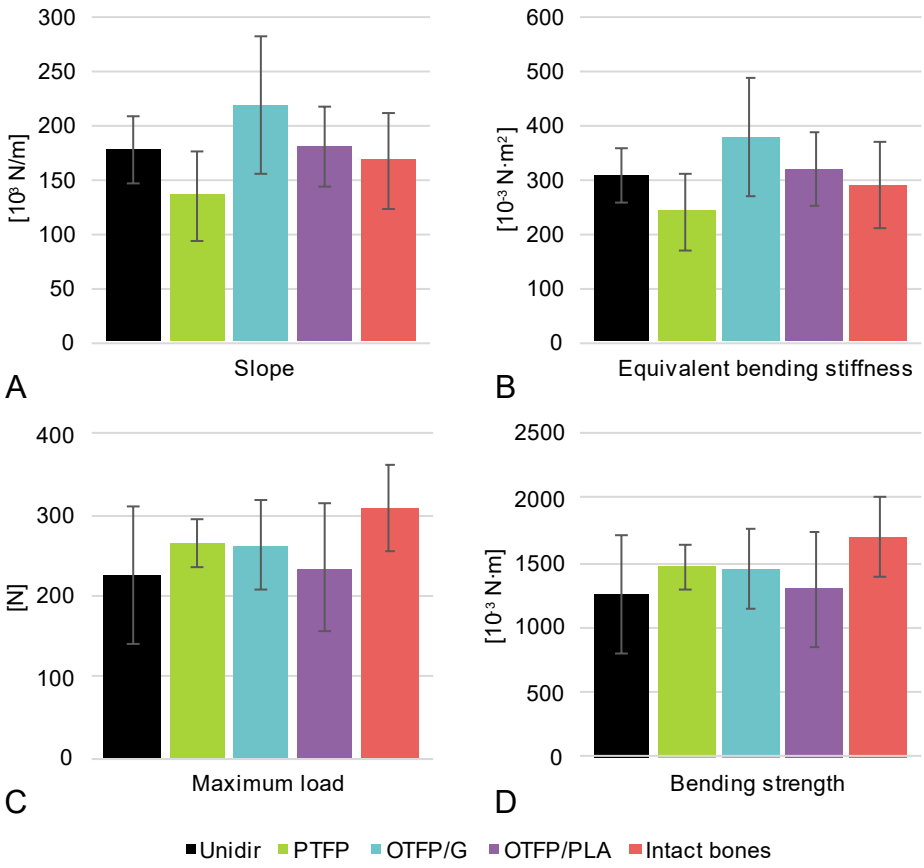

Figure 32. Results of the four-point bending test of bone specimens conducted in Study III: curve slope (A), equivalent bending stiffness (B), maximum load (C), bending strength (D).

5.3.2.3 Torsional test of bone specimens

Intact bones expectedly were significantly stronger in torsion than any of the groups in which the osteotomized bone was fixed with a plate ($P < 0.001$ in all comparisons). Among the plated groups, the groups OTFP/PLA and OTFP/G showed higher resistance to break in torsion than the Unidir group ($P < 0.001$ and $P = 0.002$, respectively). The other pairwise comparisons did not reveal statistically significant differences (Table 34, Figure 33A).

The maximum torque values were obtained at the highest angle in the group OTFP/G and OTFP/PLA, which were higher than the corresponding angle in the group Unidir with the significance levels $P = 0.008$ in both cases. Compared to the intact bone, the maximum angle in OTFP/G and OTFP/PLA was greater with the

significance $P = 0.001$ and $P = 0.007$ correspondingly. The other differences were insignificant (Table 34, Figure 33B).

The torsional stiffness, besides the intact bones, was the highest in the group OTFP/PLA which was significantly higher than the stiffness of Unidir plates ($P = 0.016$). The intact bones were stiffer than any of the plated bones group ($P < 0.001$; Table 34, Figure 33C).

Table 34. Results of the torsional test of bone specimens conducted in Study III.

Group name	Maximum torque [N·m]	Angle at maximum torque [°]	Torsional stiffness [N·m/rad]
Unidir	0.25 (0.08)[1]	13.4 (9.5, 14.6)[2]	1.1 (1.0, 1.6)
PTFP	0.54 (0.21)	24.1 (22.5, 31.1)	1.4 (1.1, 2.2)
OTFP/G	0.82 (0.23)	61.2 (26.7, 62.7)	1.5 (1.3, 2.5)
OTFP/PLA	0.91 (0.25)	40.6 (35.7, 44.1)	2.3 (2.3, 2.4)
Intact bones	2.01 (0.37)	1.1 (1.0, 1.6)	13.8 (13.2, 18.8)

[1] The data presented in the format: mean (SD).
[2] The data presented in the format: median (25^{th} percentile, 75^{th} percentile).
Modified from Study III.

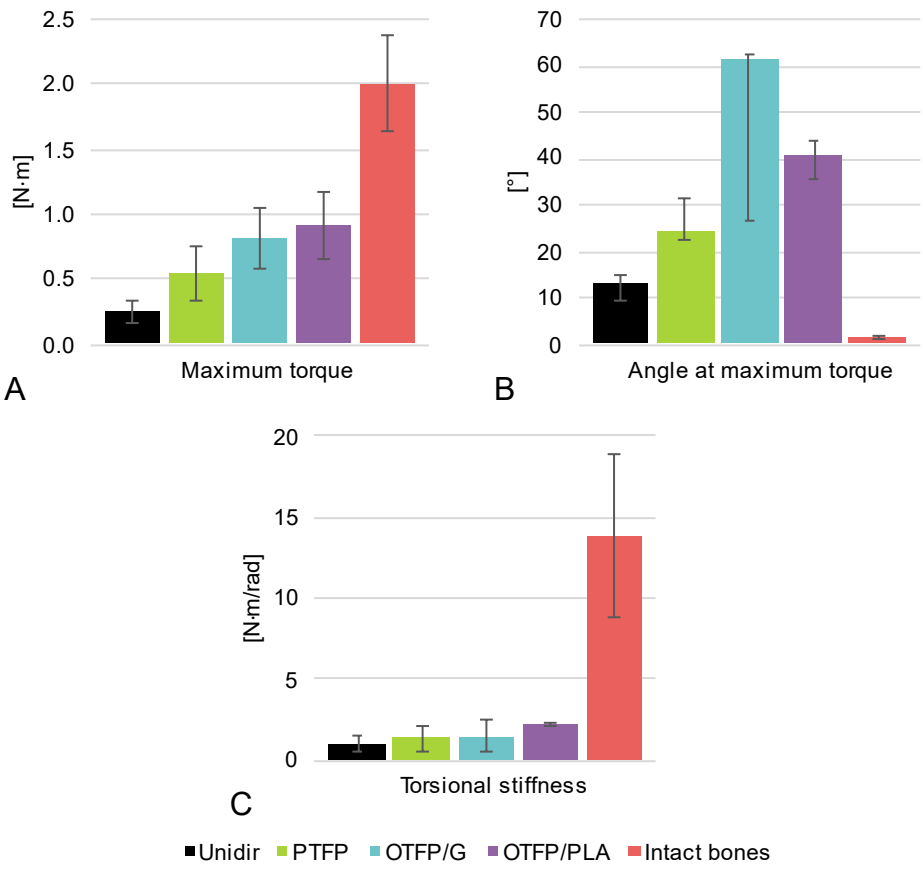

Figure 33. Results of the torsional test of bone specimens conducted in Study III: maximum torque (A), angle at maximum torque (B), torsional stiffness (C).

5.4 Study IV

5.4.1 Stage 1

5.4.1.1 Ion concentrations in SBF

The ICP-OES analysis (Figure 34) expectedly confirmed that in the group Implant prototypes/FG, the concentrations of all types of ions of interest (Ca, Si and P) did not differ from the Pure SBF after seven days of immersion. On the contrary, the analysis revealed significant increase of Si ($P = 0.002$ compared to the pure SBF and $P = 0.001$ compared to the Implant prototype/FG) and Ca (both $P < 0.001$) ion concentrations in the Implant prototypes/BG group. In the Control BG group without

any casing, concentrations of both types of ions were higher than in both Implant prototypes/FG and Pure SBF groups with significance level $P < 0.001$. At the same time, the concentrations of Ca did not differ significantly between the Implant prototypes/BG and the Control BG groups, although the concentration of Si increased in the Control BG group even higher than in the Implant prototypes/BG ($P < 0.001$). The concentration of P significantly ($P < 0.001$) dropped in the Control BG group compared to any of the other groups.

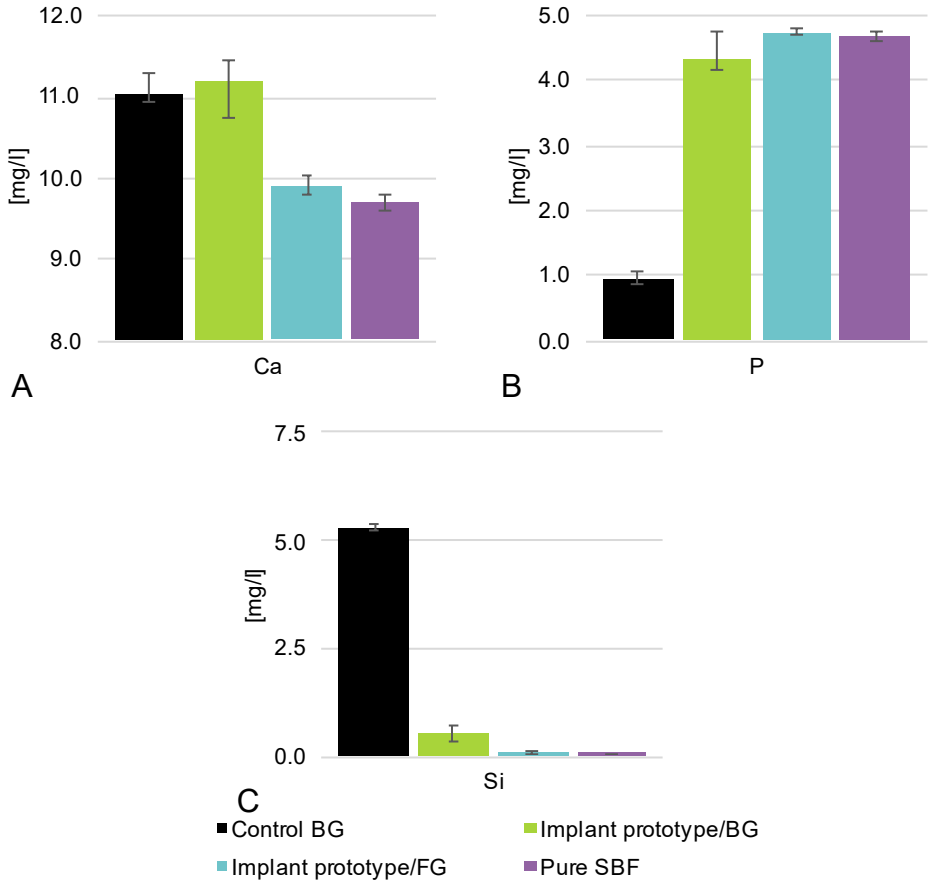

Figure 34. Results of the ICP-OES analysis conducted in Study IV: ion concentration of Ca (A), ion concentration of P (B), ion concentration of Si (C).

5.4.1.2 CaP formation

The SEM/EDS analysis detected the precipitation of CaP on the facets of the BG particles in the Control BG group. Similarly, the formation of CaP was found on

both BG particles and walls of the prototype casings in the Implant prototypes/BG group. At the same time, in the Implant prototypes/FG group, no traces of CaP formation were observed.

5.4.2 Stage 2

5.4.2.1 Dissolution test

The visual inspection of the specimens from the groups PLA and Dioxaprene® did not confirmed apparent signs of the dissolution of materials. On the contrary, the specimens from the group Max-Prene® bleached and got cracks on the surface.

5.4.2.2 Compression test

The maximum load obtained during the compression test increased after the short-term dissolution test in the groups PLA and Dioxaprene®. In the Dioxaprene® group, the slope of the load-displacement curve also visibly increased. In contrast, the specimens from the group Max-Prene® completely lost load-bearing capabilities and, although having sufficiently higher strength and stiffness before the immersion in SBF, after the immersion destroyed under minimum load which was not possible to measure.

5.4.2.3 Modeling of compression test by FEA

The mechanical properties of Dioxaprene® (Table 35) were derived from the compression test. The parameters were averaged from the available number of specimens.

The resulting load-displacement curves obtained in FEA of the compression test coincided satisfyingly with the experimental curves.

Table 35. Mechanical parameters of Dioxaprene® used in FEA in Study IV.

Parameter	Before the dissolution test	After the dissolution test
Elastic modulus [GPa]	0.538	0.657
Yield strength [MPa]	16.8	29.5

Modified from Study IV.

5.4.2.4 Modeling of TTA implants by FEA

The simulation of the 3D model of the real TTA implant for a middle-sized dog, using the parameters obtained and validated for the group Dioxaprene®, demonstrated the absence of irreversible inelastic deformations under the loads up to the limit (1917 N) achieved by Etchepareborde and colleagues (Etchepareborde et al., 2014).

5.4.3 Stage 3

5.4.3.1 Dissolution test

In the dissolution test of whole experimental implants, the observed speed of the degradation of different parts coincided with the results of the preliminary dissolution test of the filament specimens (section 5.4.2.1). The casings made of Max-Prene® bleached and disintegrated into multiple small particles. After filtering of the remainders of the implants through paper filter, the particles of Max-Prene® became visually indistinguishable from the BG particles. At the same time, the insert made of Dioxaprene maintained its initial star-like shape, although multiple cracks and surface cavities were observed under light microscope.

5.4.3.2 General results of the *in vivo* experiment

One of the rabbits was prematurely excluded from the *in vivo* experiment. The animal was euthanized on day 26 due to severe mandible infection. Samples for micro-CT and histological analyses were nevertheless extracted and studied, however not included in the statistics. The excluded animal had an empty defect on one side and an experimental implant on another side.

Thus, nine out of ten animals successfully recovered from the surgery. The euthanasia was performed on day 84 as planned. Before the extraction of biological samples, a visual inspection was done. No pathologies were found, hence the micro-CT and histological samples from nine rabbits were included in the statistical analysis.

5.4.3.3 Micro-CT analysis of rabbit femora

Reconstructed 3D images of all samples confirmed bone growth in the experimental implants in all collected biological samples. Formation of new tissues occurred from all sides of an implanted defect, connecting in the middle of the implant and encapsulating the insert and BG particles. The amount of the conglomerate of new

tissues and encapsulated BG particles in the experimental implants was higher than number of new tissues in the empty defects, however the difference was not significant (Table 36, Figure 35).

Table 36. Results of the micro-CT analysis of rabbit femora conducted in Study IV.

Group name	Bone volume fraction by VOI compartment [%]			Total bone volume fraction with respect to the whole VOI
	VOI-I	VOI-II	VOI-III	
Experimental implants	30.2 (16.0)[1]	8.9 (5.8, 13.5)[2]	10.8 (7.6, 17.4)	19.2 (7.8)
Empty defects	17.3 (8.4)	0.4 (0.1, 1.15)	1.1 (0.1, 10.0)	11.8 (12.6)
Experimental implant in the excluded animal	28.5	8.8	29.1	23.8
Empty defect in the excluded animal	9.5	1.4	19.2	10.4

[1] The data presented in the format: mean (SD).
[2] The data presented in the format: median (25th percentile, 75th percentile).
For the experimental implants a volume of the conglomerate of bone tissue and BG particles is considered.
Modified from Study IV.

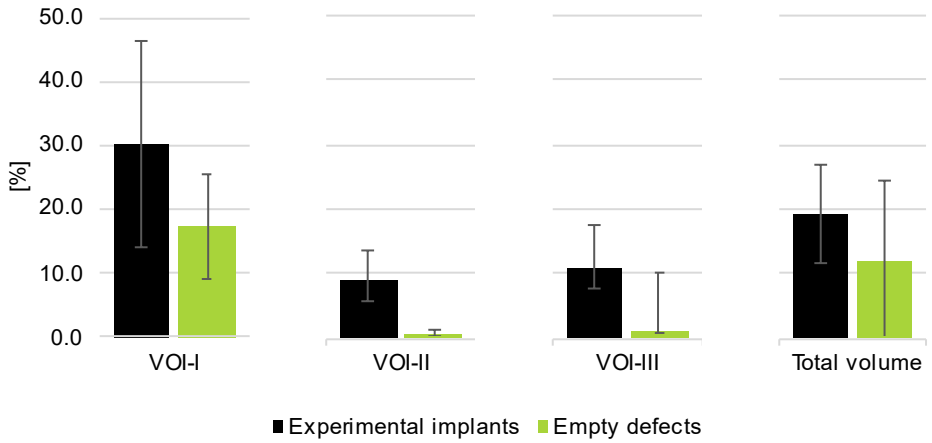

Figure 35. Results of the micro-CT analysis of rabbit femora conducted in Study IV.

5.4.3.4 Histological analysis of rabbit femora

Qualitative visual assessment of the tissues in histological samples confirmed formation of normal bone tissues in all groups (Figure 37).

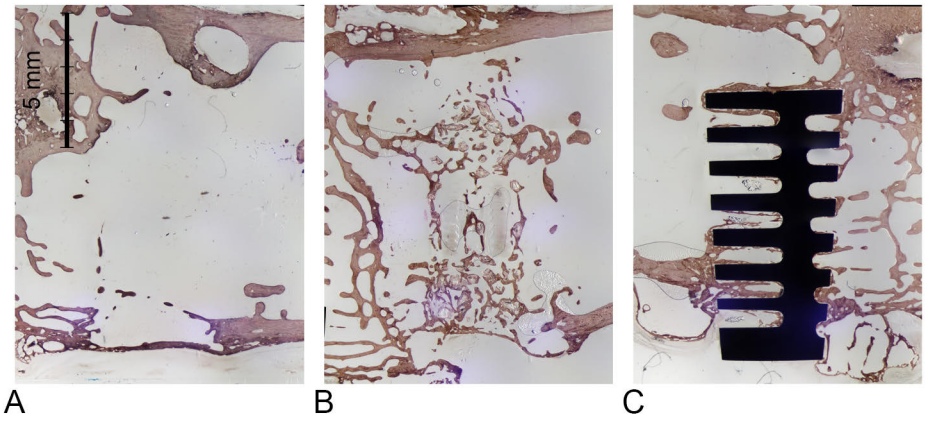

Figure 36. Examples of histological sections (VK stain): empty defects (A), experimental implants (B), control implants (C). Image modified from Study IV.

In the control implants, the new tissue grew in the transverse groves but not in the axial channel. In the experimental implants the new tissue grew throughout whole volume by encapsulating and bridging the BG particles, confirming the result of the micro-CT examination. A layer of CaP was visually observed in the cross-sections of BG particles, thus implying the resorption of BG. Insignificant amount of the new tissue was observed also in the empty defects.

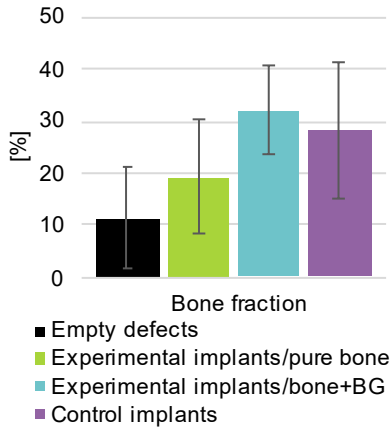

Figure 37. Results of the histological analysis of rabbit femora.

Quantitative analysis of the amount of new bone in the experimental implants was generally in line with micro-CT analysis (Table 37, Figure 37) however the difference between the experimental implants and empty defects was not significant statistically if considering the volume of new bone solely. At the same time, the significance level for the difference between the control implants and empty defects was $P = 0.003$. If taking into account the total volume of the bone and encapsulated BG particles which eventually would

be substituted with bone, the significance between the experimental implants and empty defects reached $P < 0.001$. The total amount of new bone in control implants and bone/BG particles conglomerate in the experimental implants was similar to the bone fraction in the intact rabbit femur (van der Meulen et al., 2009, 2006).

Table 37. Results of the histological analysis of rabbit femora.

Group name	Bone fraction [%]
Experimental implants	19.2 (11.0) / 32.0 (8.5)[1]
Control implants	28.3 (13.0)
Empty defects	11.3 (9.7)
Experimental implant in the excluded animal	12.0
Empty defect in the excluded animal	9.7

[1] In the numerator: volume fraction of bone tissue; in the denominator: volume fraction of the conglomerate of bone tissue and encapsulated BG particles.
The data presented in the format: mean (SD).
Modified from Study IV.

6 Discussion

The present PhD dissertation included four studies in which the main aspects related to the development and preliminary examination of a novel concept of non-metallic bioactive load-bearing implants were logically and systematically covered. The multidisciplinary research included a wide range of mechanical, chemical and biological experiments, including *in vivo* pre-clinical study of a veterinary implant, performed in the broad collaboration.

The novel concept proposed in the research is intended for both animals and humans. In the framework of this dissertation, the veterinary applications were considered as the first step on the way to the applications in humans. Novel treatment solutions to actual issues typical in pets were suggested: the *in situ* contourable FRC fracture fixation plate for the treatment of antebrachial fractures and a prospective polymer intended for the use as the matrix in that FRC plate (Studies I…III), and the implant for the treatment of CrCL disease (Study IV). The research resulted in conceptual prototypes and prepared a broad basis for further studies.

6.1 Study I

In the first study we experimentally assessed the hypothesis that biostable FRC can be used for manufacturing of small-sized fracture fixation plates intended to treat antebrachial fractures in toy-breed dogs. Based on the previous fundamental studies in larger animal models and clinical outcomes of the applications of FRC implants in humans (Akeson et al., 1975; Bradley and Hastings, 1980; Gillett et al., 1985; Jockisch et al., 1992; Kettunen et al., 1999b, 1999a; Pemberton et al., 1994; Tayton et al., 1982; Tayton and Bradley, 1983; Woo et al., 1983), we presumed that the mechanical properties of FRC would be more adequate to the bone tissue in terms of the stiffness, providing desirable amount of micromotions in the fracture, while being strong enough, also in smaller devices. To test the hypothesis, we prepared a few different FRC having bisGMA-TEGDMA co-polymer as the matrix and E-glass reinforcement in different forms and tested them mechanically. Additionally, we tested capabilities of simple inbuilt material models, available in most of FEA programs, to perform preliminary estimation of mechanical properties of FRC plates using the obtained materials' properties.

Biostable FRC reported in earlier studies usually had thermosetting epoxy (Pemberton et al., 1994; Tayton et al., 1982; Tayton and Bradley, 1983) or thermoplastic (Akeson et al., 1975; Jockisch et al., 1992; Woo et al., 1983) matrix reinforced with carbon fibers. However, more recent studies showed that a combination of methacrylate matrix materials, such as bisGMA, reinforced with E-glass fibers, can also be successfully applied for skeletal reconstruction, including load-bearing applications (Aitasalo et al., 2014; Moritz et al., 2014; Piitulainen et al., 2017, 2015; Zhao et al., 2009). As shown in the literature, FRC plates made of carbon-fiber-reinforced PEEK are one of the limited number of relatively often used composites in medical practice (Boriani et al., 2018; Laux et al., 2018; Zoccali et al., 2016); therefore, this material was used as a control.

As one of the main loading modalities leading to fractures of long bones is bending (Jain et al., 2018), the investigation of flexural properties of composites was chosen for the experiment. Three-point bending test, applied in the Study, is one of the standardized methods to acquire the flexural properties of materials (ASTM D790-00).

One of the sub-goals of the study was to determine the range of the acceptable physical properties of the materials and structural mechanical properties of the plates as whole parts. One should consider that the intrinsic material's physical properties as such do not guarantee that the stiffness of the bone-implant construct would be adequate. For instance, one of the fundamental studies on the question of the less-rigid fixation concept (Woo et al., 1983) reported a design of a hollow metallic plate which possessed substantially more adequate structural stiffness than a solid device of the same material, stainless steel. By varying the thickness or, being more precise, the cross-section area of a plate and the material's mechanical properties, one can achieve comparable stiffness of plates made of quite different materials. Apparently, it is important to find a balance between the choice of material and the design. Thus, two main characteristics were studied in the literature: 1. the elastic modulus and, related to that, stiffness of the device; and 2. the material's strength and, corresponding to that, structural strength of the device.

In our search we presumed that the intrinsic mechanical properties of homogeneous polymers are below the range in question. As the minimum threshold, we accepted the properties of so called self-reinforced polymers. These polymers are a type of composites, in which the reinforcement fiber-like elements are made of the same material as the matrix. Made by different techniques, those fiber-like elements comprise highly oriented polymer chains. Self-reinforced polymers have been used in rods and screws at least since 1980s (Majola et al., 1992; Niiranen et al., 2004; Törmälä, 1992; Veiranto et al., 2002). Saikku-Backstrom and colleagues (Saikku-Bäckström et al., 2005) demonstrated that self-reinforced PLDL can be successfully used in the fracture fixation plates for small dogs. The reported flexural strength of

similar polylactides is within the range 166…300 MPa (Majola et al., 1992; Niiranen et al., 2004; Törmälä, 1992; Veiranto et al., 2002). For self-reinforced mixed PLA/PGA polymers flexural strength could achieve 250…370 MPa (Vainionpää et al., 1987) The other studies on the less-rigid fixation concept reported similar values achieved by mean of the reinforcement of a polymeric matrix with fibers: from 251 MPa (Gillett et al., 1985) to 450 MPa (Kettunen et al., 1999b). These values are in fact comparable to or barely slightly higher than the analogous averaged parameter of the canine cortical bone – 185 MPa by (Acevedo et al., 2015) or 251.0 MPa (Autefage et al., 2012).

As for the stiffness characteristics, the flexural modulus of PLDL analogous to the one used by Saikku-Bäckström could achieve 4…5 GPa (Majola et al., 1992; Niiranen et al., 2004; Veiranto et al., 2002) or even 10 GPa (Törmälä, 1992). The flexural modulus of the reinforced polymers was reported to achieve from 8.52 GPa (Gillett et al., 1985) to 40 GPa (Kettunen et al., 1999b). The reported intrinsic flexural modulus of the canine cortex might have value from 15.6 GPa (Autefage et al., 2012) to 18 GPa (Acevedo et al., 2015), which lies approximately in the middle of the reported values of moduli of self-reinforced polymers and polymeric composites.

At the same time, the conventional metallic alloys have an order of magnitude greater elastic moduli: 106…114 GPa is a typical value range for titanium alloys (Baron et al., 2015; Losertová et al., 2016), 210 GPa – for the surgical stainless steel (Losertová et al., 2016), while cobalt-chromium alloy might achieve 283 GPa (Baron et al., 2015; Baron and Ahearne, 2017). The strength of metals is also usually higher, although the difference is less considerable: 940…1034 MPa for titanium (Baron et al., 2015; Losertová et al., 2016), 977 MPa for stainless steel (Losertová et al., 2016) and up to 1403 MPa for Co-Cr alloy (Baron et al., 2015; Baron and Ahearne, 2017).

Thus, we assumed that the sufficient value for the strength and modulus of the material might in fact fall within a broad range estimated in 166 MPa and higher, and approximately 4 to 40 GPa, respectively. Moreover, it is important to consider that quadrupedal animals, which are the target patients of the study, have a possibility to re-distribute the loads during the healing period on the three healthy legs (Anderson, 1993). From that prospective, the characteristics of metals especially seem to be an overkill for toy-breed dogs.

The FRC specimens prepared and tested in Study I with bisGMA as a matrix material, demonstrated considerably different intrinsic parameters in three-point bending depending on the type of reinforcement. However, our results, including those for the control CFR-PEEK, were similar to the values reported in the literature for analogues composites earlier. Unsurprisingly, the highest properties were demonstrated by the composites reinforced with continuous unidirectional fibers: modulus 36.4 GPa and strength 831 MPa, which were in line with the earlier results

of Moritz and colleagues: 30 GPa and 631 MPa, respectively; (Moritz et al., 2016) and Abdulmajeed and colleaugues: up to 32.2 GPa and 902 MPa, depending on the fiber fraction (Abdulmajeed et al., 2011). Also similar results were shown, for example, for hybrid glass/flax/epoxy composites: 39.84 GPa and 591.25 MPa (Manteghi et al., 2017). The results of the control group, CFR-PEEK, were within the range of the values reported in the literature. Our results were 10.6 GPa and 223 MPa for modulus and strength, while found in the literature were bending modulus from 5.41 GPa to 17.0 GPa and strength from 159.25 MPa to 307 MPa depending on the type of fibers and manufacturing method (Han et al., 2019; Jockisch et al., 1992). Similar results were achieved by chopped carbon-fiber reinforced composites with different thermoplastic matrix, for instance, in (Gillett et al., 1985).

The shape of the plates, prepared from the experimental FRC and tested in the second stage of Study I, repeated that of one of the commercially available stainless-steel devices for toy-breed dogs; those stainless-steel plates also served as the control. However, cutting original curvy shape of the plate in some groups was considerably hampered by the form of the reinforcement. Therefore, in these groups the shape was simplified to the one with straight edges.

The testing modality for the plates was based on the standard ISO9585-1990 for testing metal plates with the length 50 mm or longer. To the best of our knowledge, there is no standardized methods for testing plates of the dimensions similar to the ones prepared in the study, nor a special standard for FRC plates. However already in early studies of FRC plates the four-point bending was applied (Bradley and Hastings, 1980; Tayton and Bradley, 1983). On the other hand, the aforementioned standard has been used for testing of small plates for facial reconstruction with the length 50 mm or even shorter (Lee et al., 2016; Waizy et al., 2012).

Expectedly, stainless steel plates demonstrated the highest results in the four-point bending, however the group bisGMA/unidir was only insignificantly weaker. In addition, since the results of the first stage for bisGMA/sleeving and the control CFR-PEEK groups fell within the acceptable range of mechanical properties defined earlier, the group bisGMA/sleeving could preliminarily be considered as deserving further studies.

Another direction for further research might be more thorough investigation of the properties of FRC devices in question at the aqueous environment. The previous studies demonstrated the adverse effect of the liquid absorption for the mechanical properties of FRC (Lassila et al., 2002), which undoubtedly should be accounted for in the design of FRC fracture fixation devices.

The material's parameters obtained in the three-point bending of parallelepiped FRC specimens were used in the FE simulation of the mechanical tests. The design of the FE model was deliberately aimed at use of the most available material models

which usually included FE software by default and do not require complex mechanical testing to achieve the material's parameters. Thus, standard metal plasticity model was selected to reflect the inelastic behavior of materials since the amount of such inelastic deformations was expected to be relatively small (Bergstrom, 2015). The results of that computer simulation demonstrated reasonable coincidence of the modeled load-displacement curves with the ones obtained in the actual tests. However, in the simulation of the four-point bending tests the differences in results were considerable in absolute values. Alike discrepancies were observed, for instance, in the FE simulation of bisGMA-based FRC in (Zhao et al., 2009). There might be various factors contributing to the resulting imprecision. Among them, for example, homogenization of anisotropic properties of FRC. However, since the tests modeled in FEA included only bending load, in which the stresses aligned with the longitudinal axis of specimens contribute overwhelmingly, we considered this simplification acceptable. Another challenge in modeling small-sized objects like the tested mini fracture fixation plates was the geometrical precision achievable in the manufacturing process and in the measurement of plates. It is known that the bending stiffness is a function of the area moment of inertia of the object subjected to bending. Additional FEA, in which we compared the bending stiffness of plates with different thicknesses with the step of 0.05 mm demonstrated numerically that the difference in stiffness might achieve 233 % while the thickness changed by 54%. Thus, the total imprecision in the thickness between the plate and its 3D model could substantially decrease the precision of modeling when the order of magnitude of the object's dimensions is as low as 10^0... 10^1 mm. Also, the ratio between the size of the composites' constituents and the plates is considerably different from that in modeling, for instance, of parts of an airplane. Thus, it is more difficult to achieve comparable uniformity of the mechanical properties throughout the FRC mini plate than *e.g.*, the airplane wing, which obviously contribute to the imprecision of material homogenization approach.

Particularly for the stainless-steel plates, some challenges were also faced in finding proper mechanical characteristics for modeling. It is known fact that some manufacturing methods, such as cold working, significantly (hundreds of percents) affects the mechanical properties of metals, including stainless steel (Moen and Duncan, 1976). Without knowing the exact fabrication method of the stainless steel plates used in the study, we applied one of the sets of mechanical properties reported in the literature (Losertová et al., 2016). The resulted load-displacement curves demonstrated in general similar behavior although without exact matching.

Nevertheless, the correlation analysis showed that the relation among the results of different groups in modeling corresponded that among the groups in actual testing. Thus, we concluded that the selected modeling approach, although limited in the precision of the absolute values, allows for comparison of different materials and

might be used for preliminary estimation of the mechanical properties of FRC plates. The validation of those results however must be performed in actual testing on the further steps of the development process. Alternatively, one should use one of the available methods of modeling of anisotropic materials, such as anisotropic homogenization of mechanical properties or separating the reinforcement phase and matrix on the level of the FE mesh.

6.2 Study II

In Study II we proposed the description of the concept of *in situ* contourable bioresorbable bioactive load bearing FRC plate for fracture fixation and developed a candidate light-curable bioresorbable polymer for use as the matrix in those plates. The polymer was named PLAMA (**p**oly**la**ctide functionalized with di**me**th**a**crylate). The study included determination of basic chemical, physical and biological properties of PLAMA.

The synthesis route of oligomer mixtures from which the final light-curable resins were prepared, was relatively simple and was based on commercially available PLA diols with different molecular masses. In the literature, one could find different routes of obtaining cross-linkable aliphatic polyester oligomers, such as functionalization of polyester polyols with acrylate (Sawhney et al., 1993), unsaturated methacrylate (Melchels et al., 2009; Storey et al., 1993) or fumarate (Grijpma et al., 2005) groups. In our study, we selected methacrylate group which is used in clinically approved materials for dental and orthopedic applications, such as PMMA and bisGMA. By this, the number of variables in further actions was reduced. For instance, the photoinitiation system, which directly influence the effectiveness of cross-linking reaction in light-curable resins and, therefore, the physical and chemical characteristics of the solidified polymer (Anastasio et al., 2019; Emami and Söderholm, 2005), was adapted from bisGMA, also used in Studies I and IV of the present thesis. The photoinitiation system consisted of CQ and DMAEMA. The efficacy of that combination with respect to the obtained material properties has been demonstrated in literature (Furuse et al., 2011; Taira et al., 1988; Yoshida and Greener, 1994). The highest DC in bisGMA, found in the literature (80.6 %, seven days after curing), was also achieved with the combination CQ/DMAEMA (Furuse et al., 2011). Especially important for the purposes of our study is that the presence of blood and bone tissue did not significantly affect the cross-linking efficacy of resin, functionalized with dimethacrylate group and having CQ/DMAEMA as the photoinitiation system, used as a matrix of a FRC implant (Tuusa et al., 2005). Based on these facts, the light-curing protocol used in the study, completely replicated the protocol applied to bisGMA specimens in other studies of the present research. The correctness of this approach was proven by the

measurements of DC, which showed significantly greater values in PLAMA-500 and PLAMA-1000 in comparison with bisGMA/TEGDMA co-polymer. Finally, that a large selection of instruments for curing of dental resins with the wave range 430…480 nm can be applied to cure PLAMA.

In accordance with another research on polyester-based thermoset (Storey et al., 1993), in most of experiments of this study different modifications of PLAMA showed significantly different results. For example, PLAMA-500 had higher stiffness and strength, while PLAMA-1000 demonstrated faster dissolution and, thus, more significantly affected the change of pH value of SBF and had higher mass losses. Presumably, the properties of the final polymer can be tailored in a controllable manner by mixing two resins with different molecular masses. This could be used for adjustment of the properties of a whole implant according to the needs of a patient. However, this hypothesis needs to be tested in separate studies to derive the properties of interest as functions of the average molecular mass of the resin.

The nature of the aforementioned observations could be associated with the density of cross-links in the polymer. The higher the density of cross-links is, the higher the mechanical properties are (Ifkovits and Burdick, 2007). On the other hand, the longer molecule length and lower cross-links density increases the probability of the breakage of chemical bonds between the repeating units as one of the mechanisms of biodegradation (Ifkovits and Burdick, 2007).

As was mentioned, the mechanical properties of PLAMA-500 were expectedly higher than of PLAMA-1000. In turn, bisGMA had higher properties than PLAMA-500. The difference between bisGMA and PLAMA-500 was not dramatic numerically, however statistically significant. Study I (Liesmäki et al., 2019) demonstrated high strength and stiffness of E-glass FRC with bisGMA as a matrix, which was in accordance with previous publications (Moritz et al., 2014; Zhao et al., 2009). We expect that with fiber reinforcement, the mechanical capabilities of PLAMA-500 might be high enough for load-bearing applications, however further experiments are needed. Also, a preliminary estimation of mechanical performance of FRC might be done by means of FEA, using the results of our tensile testing as the input. For instance, a rule of mixture or similar approaches might be applied provided that the mechanical properties of fibers are also available (Sudheer et al., 2015).

Controversial results were obtained in three-point bending after the immersion in SBF, when the strength and stiffness of PLAMA slightly increased. Similar phenomenon was observed later in Study IV (Plyusnin et al., 2020) with clinically approved materials. It should be noted that in both cases we did not have intermediate time points, and the period of the immersion was limited. Obviously, longer

immersion tests with multiple intermediate tests are needed to describe in all details the character of the degradation of mechanical properties of PLAMA.

Biological safety of PLAMA was considered from two main points. First, the backbone of the PLAMA molecule, consisting of lactide repeating units, was expected to have the same degradation mechanisms as thermoplastic PLA. Therefore, all adverse effects of those were also expected to take place (Ifkovits and Burdick, 2007). Namely, PLA and the aliphatic polyesters in general are known to increase the acidity in the surrounding liquids (Agarwal et al., 1998; Li et al., 1990), which can lead to appearance of osteolysis in bones (Barber and Dockery, 2006; Böstman and Pihlajamäki, 2000; Meyer et al., 2012). The cell proliferation test carried out in our study demonstrated significant growth of MG-63 cells, often used to substitute normal osteoblasts in orthopedics material studies (Antony et al., 2017; Choppadandi et al., 2019), on PLAMA specimens. Also, the morphological test demonstrated presence of angular-shaped cells with stress fibers, which are crucial evidence of normal morphogenesis of cells, as well as good adhesion and migration on the surface of material. There were no statistically significant differences between the groups, including surgical stainless steel.

In the proposed concept of *in situ* curable fracture fixation plate, it is expected that BG fibers (Eichhorn et al., 2021; Lehtonen et al., 2013a, 2013b) of the reinforcement phase will also compensate for the adverse effects of degradation of the PLA backbone. The mechanism of that is well documented and based on the release of alkali ions from BG into the body fluids which balances the increase of acidity (Boccaccini and Maquet, 2003; Jones et al., 2006; Li et al., 1990). In addition, the BG fibers should stimulate bone growth (Hoppe et al., 2011; O'Neill et al., 2018) and, on the other hand, inhibit the growth of bacteria decreasing the risk of infection (Allan et al., 2001; Drago et al., 2018). Our expectations are based on multiple studies investigated the properties of a combination of polyesters and BG as bioactive filler in composite implants and scaffolds (Boccaccini and Maquet, 2003; Daculsi et al., 2011; Kunze et al., 2003). Supposedly, it can be possible to adjust the rate of biodegradation and bioactivity of an implant, thus tailoring it to a concrete patient and clinical conditions, by varying the composition, amount and distribution of the BG fibers of the reinforcement phase.

The second aspect of biological safety relates to the dimethacrylate functional group. Acrylic biomaterials have been used in medicine since the middle of the 20th century, and therefore there is vast amount of the data on the adverse effects of those. The main concerns in the application of PLAMA as orthopedic implant material one could attribute to allergic reactions in skin (Gautschi et al., 2010; Kanerva et al., 1997; Prajapati et al., 2013), cytotoxicity caused by acrylate free radicals (Moreau et al., 1998), inflammation and osteolysis invoked by the products of wearing of acrylic materials (Chiu et al., 2006; Glant et al., 1993; Quinn et al., 1992). Despite that,

research on novel acrylic materials continues (Hu et al., 2018; Miao et al., 2016; Rajasekharan et al., 2020). Also, application of acrylates in such sensitive applications as cranial implants have been reported (Aitasalo et al., 2014; Peltola et al., 2012; Piitulainen et al., 2015). Considering promising results reported in previous cell studies on materials similar to PLAMA (Melchels et al., 2009; Sawhney et al., 1993), we can expect that the biocompatibility of PLAMA can be adequate, however additional experiments, including *in vitro* and *in vivo* experiments, are needed to support this assumption.

6.3 Study III

Study III summarized the previous endeavors of the research group (Kulkova et al., 2016; Kulkova, 2020) as well as Studies I (Liesmäki et al., 2019) and II (Plyusnin et al., 2021) of the present thesis to demonstrate the proof of concept of one of the implementations of the novel implant concept, namely – the *in situ* contourable bioresorbable bioactive fracture fixation plate. The feasibility of the TFP technology for fabrication of fracture fixation mini plates was shown. Mechanical testing of TFP-reinforced plates with and without prototype polymeric shell demonstrated that such plates could withstand sufficient loads in bending and torsion until cracking, providing the same time exceptional structural integrity beyond the onset of cracking. Spatial optimization of the TFP reinforcement was done, remarking possible ways for further, more comprehensive optimization of the TFP pattern.

As was shown in Study I, the plates reinforced with a glass-fiber braided sleeving, although were significantly weaker than the ones reinforced with unidirectional fibers, still were comparable to the control plates prepared from commercial CFR-PEEK composite (Liesmäki et al., 2019). At the same time, the plates reinforced with the sheet glass fiber fabric completely failed the bending test. This attracted our attention to the braided structures which, being adapted to the concrete intended application and thus, to the design of the exterior of a fracture fixation device, might be used as the reinforcement in composite plates, especially in the small ones like plates for toy-breed dogs. In the plates investigated in the present research, the width of the remaining material surrounding the holes for fixation screws is less than 1.5 mm on each side. Based on our findings we assumed that this width would not significantly contribute to the mechanical performance of the plate in transverse loads, *i.e.*, in torsion. Thus, it might be beneficial to fill these areas with longitudinal fiber rovings solely, which would in addition go through the whole length of the plate. At the same time, passing the screw holes in the shape of eight would increase the transversal stiffness and the structural integrity of the plate. A piece of a braided sleeving partially met these requirements. However, it might be challenging to shape the braided sleeve to the form of a particular fixation device

due to the looseness of the sleeving. In addition, one cannot adjust the number of fibers in standardized sleevings, neither rearrange them to further control the stiffness in this or that part of the device. Thus, the TFP technology (Gliesche et al., 2003; Mattheij et al., 1998; Spickenheuer et al., 2008) which enables manufacturing of arbitrary-shaped fiber-reinforced structures, adapted to the anticipated directions of loads acting in the structure, was applied to prepare the reinforcement of the next iteration of the FRC plates. Taking the advantages of TFP, a pilot design partially inspired by the braided sleeving was developed and tested in the first stage.

The pilot three-point bending test expectedly showed considerable improvement of the withstood load in the TFP-reinforced plates compared to the unreinforced specimens. The further increase in that parameter in the plates encased into PC shell was also anticipated due to increase of the thickness and thus amount of material in the cross-section (Woo et al., 1983). However, since PC was used as a surrogate of a bioresorbable shell, the final value of that increase will depend also on the modulus (Woo et al., 1983) of the actual material of the shell.

Based on the assumptions explained in details in the discussion section for Study I (Liesmäki et al., 2019), the four-point bending test was applied to compare mechanical capabilities of plates in the next stage of Study IV. In the control plates reinforced with continuous unidirectional fibers, identical to the ones used in Study I, the test reproduced results also very similar to the values obtained in that previous Study. However, in the current Study, plates in all groups were made with transversal curvature which in clinical conditions would improve the contact with a bone. In the case of unidirectionally-reinforced plates, this curvature led to occurring of a longitudinal crack instantly propagated through the whole plate shortly before the breakage of the plate. On a load-displacement plot it was seen as a slight step down on the almost straight line. Apparently, this crack contributed to the bending properties of the plates inconsiderably since it occurred due to the decohesion in the matrix-fibers interface while the fibers remained intact. However, this implied that fully unidirectional plates should never be used as actual fixation devices due to the risk of a total collapse. Thus, the bending properties achieved by the unidirectional plates could be considered rather as the ultimate point to which the TFP plates could asymptotically tend but obviously would never reach it.

Nevertheless, the bending capabilities of the Unidir group in the four-point bending were significantly higher than the ones achieved by any of the TFP groups. On the other hand, the TFP plates demonstrated the ability to keep the residual integrity far beyond the initial failure point, while the Unidir plates could break not only longitudinally, as explained above, but also transversely.

In Study I we concluded that devices made of a material whose homogenized mechanical properties fall within the acceptable range, defined as at least 166 MPa for the strength and 4 GPa to 40 GPa for the bending modulus (Liesmäki et al.,

2019), are expected to perform well enough in fracture fixation devices. To account for the design features, we used the four-point bending test adapted from the standard ISO9585, which allowed us to compare different implants with each other. The same test was also applied in the current study. However, these assessments still leave room for misinterpretation since they do not answer the question whether the stiffness of the concrete device is sufficient for the concrete clinical condition? Attempts to quantitatively estimate the relevance of an implant to the successful fracture treatment were made in (Tayton et al., 1982; Tayton and Bradley, 1983). In those works, the authors used bending stiffness expressed in [N·m/°] to estimate and compare the stiffness of fracture fixation devices. The stiffness was measured in four-point bending resembling the setup eventually included in the standard ISO9585. Numerically, the value in question was expressed as the ratio of the achieved bending moment to the angle of bending. Discussion on the effect of the stiffness of fracture fixation plates on the healing process in human tibia was presented by Tayton and Bradely in their publication on the clinical study (Tayton and Bradley, 1983). The authors evaluated two types of stainless-steel plates and two types of FRC plates filled with carbon fibers. The design of the latter two devices replicated that of the metallic counterparts. The achieved bending stiffness constituted 4.34 N·m/° and 3.8 N·m/° for stainless steel plates and 2.0 N·m/° and 1.65 N·m/° for the composite plates. Based on the results, the authors suggested that the minimum threshold value of bending needed to exclude the non-union was as low as 1.0 N·m/°, while completely uneventful healing was liable provided that the stiffness was above 1.75 N·m/° (Tayton and Bradley, 1983).

Bearing in mind the differences in the dimensions of the plates for human tibia and the mini plates for toy-breed dogs, investigated in our research, the method explained above was downscaled to the dimensions of the mini plates, taking the value of 45…50 % of the stiffness of the stainless-steel plates as the threshold. Thus, the stiffness of the unidirectionally-reinforced FRC plates in Study I was estimated as 74 % of the control stainless steel plates stiffness. In the present Study IV, the stiffness of PTFP-G plates was 12 %, in the group OTFP-G it was 5 % and in the group OTFP-PLA – 11 %. Obviously, the applicability of the method to small-sized plates needs to be investigated in separate studies. Nevertheless, the rough estimation shows that the stiffness of TFP plates achieved in the present research might be insufficient, and further *in vitro* and *in vivo* studies are needed.

In addition to the bending tests of plates, in this study we carried out a series of bending tests of osteotomized bones fixed with the same types of plates. The experimental setup was based on the previously reported studies aimed at biomechanical comparison of fracture fixation plates (Sod et al., 2005) and was adjusted to the dimensions of our mini plates. In our research, we intended to achieve in these tests additional data which would allow to compare the behavior of plates in

more mechanically relevant conditions than benchmark tests of plates. However, the results of all groups, surprisingly, did not significantly differ from each other. Based on one experiment, it was difficult to conclude what were the reasons for the achieved outcome. However, one could question the choice of the chicken tibiotarsi as the substitute for canine tibiae. In this test, the focus was still on the mechanical properties of plates. Thus, the bone played secondary role as a support for the plate. Also, it was impossible to collect the necessary amount of the actual canine tibiae of comparable dimensions, especially considering the fact that the morphology (Palierne et al., 2008) and mechanical properties (Autefage et al., 2012) of dog bones significantly differ among breeds. From those points, we selected chicken tibiotarsi extracted from the chicken drumsticks available in food stores as a substitute. The dimensions of those bones were comparable to tibiae of toy-breed dogs. Importantly, that the elastic modulus of chicken tibiae found in the literature was 13.15…15.41 GPa and the ultimate strength was 341.73…358.12 MPa (Regmi et al., 2017) while the corresponding averaged values for different breeds of dogs were 15.6 GPa (SD 2.6 GPa) and 251.0 GPa (SD 49.2 GPa) (Autefage et al., 2012). Finally, the common point that avian bones could be considered *a priori* lighter and more fragile is questionable; it was shown that the ratio between the body mass and the mass of leg bones in birds is even higher than in small mammals (Cubo and Casinos, 2000). Thus, the choice of chicken tibiotarsi was considered appropriate. Nevertheless, further experiments could help to clarify the encountered uncertainty.

Plated bone specimens were also tested in torsional test adapted from (Sod et al., 2005). Expectedly, the Unidir specimens demonstrated catastrophic failure due to matrix-fiber decohesion. Opposite to that, all TFP specimens demonstrated significantly higher capability to withstand torsional loads. However, there was no statistically significant difference among the TFP groups.

Providing an adequate torsional stiffness is crucial for a fracture fixation plate. Even in normal straight gait there are transverse components in the ground reaction forces acting in dog's front and hind limbs (Kapatkin et al., 2007). Also, it should be borne in mind that different muscles in both front and hind limbs are attached from all sides of bones (Shahar and Milgram, 2005, 2001) thus creating some torsion moments. Similar situation is present in bipedals (Yang et al., 2014). Obviously, it is unlikely that a plate is perfectly aligned with any of axis in the kinematics scheme, nor unlikely that the forces distribution along the three Cartesian axes remains the same in actual conditions when the patient needs to do more kinematically complex moves than straight walk. Generally speaking, the idea of fiber reinforcing is that the more fibers are aligned with the expected load, the better the stiffness and strength of composite is. Thus, with the same amount of material, increase of reinforcement in one direction is always made at the expenses of the decrease in another direction (Moritz et al., 2014; Zhao et al., 2009). Our results showed that the current TFP

design needs improvement of stiffness in the bending direction, and the aiming value might be approximately 45 % of the stiffness of stainless-steel plates tested in our studies. Further *in vitro* and *in vivo* studies are needed to test whether the needed balance is reachable.

6.4 Study IV

In Study II we proposed the concept and investigated the *in vitro* and *in vivo* behavior of the prototypes of novel bioresorbable bioactive TTA implant. The outcome of the Study generally reflected our expectations. We expect that the novel implants could decrease the adverse effects of conventional metallic TTA implants which remain in the body for the lifetime of the patient, on one hand, and increase the osteointegration rate due to the bioactive properties of the BG filler of the novel implant. We also believe that our implant can be used to replace a metallic counterpart in the case of revision surgery due to the failure of metallic implant to compensate for bone losses.

The prototypes of the future TTA implants were prepared for this study by means of FDM, one of the most widespread and economically affordable AM technologies. The pivotal role in this choice also played the fact that medical-grade polymeric filaments for FDM printing already exist in the market. Furthermore, AM technologies in general, and FDM in particular, allows for relatively easy scaling of the reference design, and, if needed, tailoring of that to the specific patient's needs.

The pilot test conducted with biostable PLA prototypes in the first stage of the study confirmed that the BG filler encased in sealed casings was in contact with the SBF, which led to the formation of CaP on the surfaces of BG filler and casings' walls (Kokubo and Takadama, 2006). Other evidences to that were the statistically significant, compared to the pure SBF and control FG prototypes, fluctuations of the concentration of Ca and Si ions in the liquid (Hench et al., 1971; Hoppe et al., 2011; Jones et al., 2006). Thus, we concluded that in technical PLA filament, whose dissolution rate was negligible within the time frames of the experiment, the natural pores occurred during the filament deposition were enough to allow for the beginning of the reaction between the bioactive filler and the surrounding fluids. Technically, this implied that the bioactive filler of the FDM-printed implants could start working almost immediately after implantation even if the degradation of the fast-resorbing parts whose only aim was to prevent scattering the BG particles before and during the implantation is inhibited due to some reason.

The concept of separating the actual TTA implant into faster and slower-resorbing parts was tested in the next stages using more advanced experimental prototypes. Although the first stage demonstrated the penetrability of virtually non-resorbable printed structures for the active ions, the casings of the experimental

implants were deliberately made perforated to minimize risks for the animals in the *in vivo* experiment. The size of the pours, *ca.* 350 µm, was based on the literature (Li et al., 2007; Otsuki et al., 2006). The outcomes of both *in vitro* dissolution test of the experimental implants and *in vivo* test in rabbits demonstrated that our choice of the material for the fast-resorbing parts of implants was correct. In fact, the design of the experimental implant can be used as such or with some modifications as a bioactive device for filling large bone defects in addition to a separate load-bearing device. In that case, the BG particles could be replaced or combined with another filler. Such devices could be used in both animals and humans.

It is well-known fact that the dissolution of a large amount of bioresorbable polymers, such as aliphatic polyesters similar to the materials used in the study, leads to the release of acidic products. This results in adverse effects like osteolysis in the trabecular bone (Barber and Dockery, 2006; Böstman and Pihlajamäki, 2000; Meyer et al., 2012). From that point, the additional role of the BG filler of the implant is to compensate for the decrease in pH level caused by the acidic products of the implant's casing degradation by balancing the pH value during the dissolution of BG (Boccaccini and Maquet, 2003; Jones et al., 2006; Li et al., 1990; D. Zhang et al., 2010). Furthermore, the increase of pH is presumably one of the mechanisms of antimicrobial activity of BG (Allan et al., 2001; Drago et al., 2018; D. Zhang et al., 2010).

The reader could raise the question whether a putty-like BG-loaded bone graft substitute could have been more convenient to handle than BG particles both in fabrication of an implant and during the surgery, which could have also allowed to avoid fast-resorbing sealing. However, we rejected that option due to doubts in the effectiveness of this choice. It has been shown that bioactivity of BG particles, the most of which remains embedded in the putty, can be significantly inhibited until dissolution of the binding substance (Stoor and Frantzen, 2017). On the contrary, too fast dissolution of the binder leads to collapse of the filler due to appearance of a dead space between the particles, which might affect the load-bearing capabilities of an implant (van Gestel et al., 2019).

The outcome of the *in vivo* study confirmed our expectation regarding the speed of degradation of the two polymers selected for the fabrication of experimental implants and were in line with the *in vitro* dissolution test of the same type of implants. The qualitative examination of histological sections showed the visual evidence of the CaP layer formation on the surfaces of BG particles. Along with the result of the first stage, immersion of implant prototypes in SBF, this implied that the dissolution of BG particles had occurred. Both histological sections and micro-CT 3D reconstructions showed BG particles and new bone tissue, which ingrew in the inner space of the experimental implants, bridging those particles together. However, the two analyses showed different total amount of this

conglomerate: 19.2 % (SD 7.8 %) vs 32.0 % (SD 8.5 %); the latter value was in line with the normal amount of trabecular bone in a healthy rabbit femur [32.7…36.6 % (van der Meulen et al., 2009, 2006)]. Combining all these finding together, we believe that we could expect that significant amount of BG particles would eventually dissolve and would be replaced with bone tissue (Heikkilä et al., 1995; Lindfors et al., 2008; Turunen et al., 2004). However, the present study was not enough to give the definite answer on the length of this time period.

One could speculate on the relevance of the animal model to the aims of the study and on the reason for an additional pre-clinical animal study of the implant for veterinary applications. The final design of the TTA implant proposed by the authors represents to our opinion a significant advancement in this kind of devices. There exist publications on similar implants which were examined in dogs without, to our knowledge, preliminary studies thus amplifying the risks of a failure and related significant distress to the dogs and their owners (Bander et al., 2018; Barnhart et al., 2016). One of those studies resulted in 38 % (0.19-0.61, CI 95%) total complications rate (Bander et al., 2018). Thus, our approach assumed that maximum possible data must be collected before the clinical studies in patients even though our patients are pets. On the other hand, due to the differences in the kinematics between the dogs and rabbits, as well as due to the difference in the size (CrCL is more typical for medium-to-large sized dog breeds), our decision was to use modified experimental implants instead of the actual TTA design, first of all, to obtain the data on the biological behavior of the implant concept. The animal model in the present study was based on previous publications (Daculsi et al., 2011; Heikkilä et al., 1995). Nevertheless, the mechanical capabilities of the design of the TTA were preliminary estimated by FEA. The material model used standard metal plasticity to mimic the inelastic behavior of the polymer taking into account considerations discussed in Study I (Bergstrom, 2015; Liesmäki et al., 2019). The modeling within the range of forces 178…1917 N, reported in (Etchepareborde et al., 2014), using the virtual experimental setup based on the kinematics of mechanical tests performed in the same work, showed that no inelastic deformations occurred. Further *in vitro* and *in vivo* studies of the actual TTA implant design are in progress, clinical trials are expected.

7 Conclusions

In Study I, it was shown that fabrication of small-sized FRC fracture fixation devices is feasible. A range of possible mechanical properties appropriate for the fabrication of such plates was estimated. Plates with UD reinforcement showed the highest mechanical properties. It was demonstrated that simple FEA based on standard features available in most FEA software packages is feasible for comparison of different types of plates.

In Study II, a light-curable bioresorbable polymer intended for the use as the composite matrix in the *in situ* contourable fracture fixation plate was synthesized. Basic physical, chemical and biological properties of the polymer were identified. The results implied that the developed polymer can be used in further studies of the prototypes of the fracture fixation plates. The concept design of such plates was proposed.

In Study III, the prototypes of *in situ* contourable composite fracture fixation plates were prepared and mechanically tested. Thus, the feasibility of the concept proposed in the present research was demonstrated. A few types of TFP reinforcement were designed to assess the possibilities of the adjustment of the structural mechanical properties of those.

In Study IV, it was shown that conventional FDM 3D printing can be used for the preparation of ion-penetrable implant casings. The *in vitro* dissolution test showed the bioresorbability of the materials selected for the preparation of bioresorbable bioactive TTA implant. The *in vivo* test confirmed successful bioresorbability and safety of the selected materials in living tissues and bone growth within the experimental implants.

Acknowledgements

The author is grateful to all people who contributed to this thesis directly or indirectly and to all organizations which funded the project or hosted the author. The author asks the reader not to rank the importance of this or that person or organization to the author according to the position in the list, as the list is given in alphabetical order. Everybody's contribution was crucial. The author also would like to apologize if he forgot to mention anybody in this non exhaustive list:

Genevieve Alfont
José Humberto S. Almeida
Gareth Arthurs
Jasmina Bijelic
Lars Bittrich
Annette Breier
Cindy Elschner
Tiia Forsström
Sufyan Garoushi
Mona Gibreel
Prakirth Govardhanam
Serguei Gordeev
Päivi Haaranen
Jingwei He
Johanna Hoffren
Outi Irjala
Niki Jalava
Kaveh Nik Jamal
Päivi Jokinen
Anni Juvonen
Ilkka Kangasniemi
Tomi Kalpio
Anna Kazakova
Pauli Keränen
Simon Konze
Mihail Kopotev
Anna Kostiander
Ignat Kulkov
Julia Kulkova
Andrei Kuusinen
Lippo Lassila
Oliver Liesmäki
Tales de Vargas Lisbôa
Jonathan Massera
Niko Moritz
Tarja Mäkelä
Miho Nakamura
Michael Nelson
Regina Nizamova
Rustem Nizamov
Kristina Nuutila
Tarek Omran
Jeremy Palmer
Leila Perea-Lowery
Vesa Pohjola
Dhayakumar Rajan Prakash
Mervi Puska
Emanuel Richter

Antti Saraste
Christina Scheffler
Nicole Schmidt
Khalil Shahramian
Anna Slita
Axel Spickenheuer
Venkat Subramaniam
Gianluca Turco
Kai Uhlig
Peter Uppstu
Mariia Valkama
Pekka Vallittu
Fernanda Vecchietti
Ekaterina Vorobieva
Zoya Zhuravleva
… and all my family.

And also:

Brinter Oy
Doctoral Programme in Clinical Research, Faculty of Medicine, University of Turku
Finnish Cultural Foundation
Finnish Dental Society “Apollonia”
Finnish Foundation of Veterinary Research
Finnish National Agency for Education (EDUFI)
Leibniz-Institute of Polymer Research Dresden (IPF)
Traceray Oy
Turku Clinical Biomaterials Centre, Institute of Dentistry, University of Turku
Turku University Foundation
University of Turku.

August 2022, Turku
Artem Plyusnin

References

Abdel-Wahab, A.A., Silberschmidt, V.V., 2011. Numerical modelling of impact fracture of cortical bone tissue using X-FEM. J. Theor. Appl. Mech. 49, 599–619.

Abdulmajeed, A.A., Närhi, T.O., Vallittu, P.K., Lassila, L.V.J., 2011. The effect of high fiber fraction on some mechanical properties of unidirectional glass fiber-reinforced composite. Dent. Mater. 27, 313–321. https://doi.org/10.1016/j.dental.2010.11.007

Acevedo, C., Bale, H., Gludovatz, B., Wat, A., Tang, S.Y., Wang, M., Busse, B., Zimmermann, E.A., Schaible, E., Allen, M.R., Burr, D.B., Ritchie, R.O., 2015. Alendronate treatment alters bone tissues at multiple structural levels in healthy canine cortical bone. Bone 81, 352–363. https://doi.org/10.1016/j.bone.2015.08.002

Agarwal, M., Koelling, K.W., Chalmers, J.J., 1998. Characterization of the Degradation of Polylactic Acid Polymer in a Solid Substrate Environment. Biotechnol. Prog. 14, 517–526. https://doi.org/10.1021/bp980015p

Aitasalo, K.M.J., Piitulainen, J.M., Rekola, J., Vallittu, P.K., 2014. Craniofacial bone reconstruction with bioactive fiber-reinforced composite implant: Bioactive Fiber-Reinforced Composite Implant. Head Neck 36, 722–728. https://doi.org/10.1002/hed.23370

Akeson, W.H., Woo, S.L.Y., Coutts, R.D., Matthews, J.V., Gonsalves, M., Amiel, D., 1975. Quantitative histological evaluation of early fracture healing of cortical bones immobilized by stainless steel and composite plates. Calcif. Tissue Res. 19, 27–37. https://doi.org/10.1007/BF02563988

Akeson, W.H., Woo, S.L.Y., Rutherford, L., Coutts, R.D., Gonsalves, M., Amiel, D., 1976. The Effects of Rigidity of Internal Fixation Plates on Long Bone Remodeling: A Bio Mechanical and Quantitative Histological Study. Acta Orthop. Scand. 47, 241–249. https://doi.org/10.3109/17453677608991984

Aksoy, U., Özkayalar, H., Orhan, K., 2020. Micro-CT in Comparison with Histology in the Qualitative Assessment of Bone and Pathologies, in: Orhan, K. (Ed.), Micro-Computed Tomography (Micro-CT) in Medicine and Engineering. Springer, Cham.

Alam, F., Varadarajan, K.M., Koo, J.H., Wardle, B.L., Kumar, S., 2020. Additively Manufactured Polyetheretherketone (PEEK) with Carbon Nanostructure Reinforcement for Biomedical Structural Applications. Adv. Eng. Mater. 22, 2000483. https://doi.org/10.1002/adem.202000483

Albertsson, A.-C., Varma, I.K., 2002. Aliphatic Polyesters: Synthesis, Properties and Applications, in: Degradable Aliphatic Polyesters, Advances in Polymer Science. Springer Berlin Heidelberg, Berlin, Heidelberg, pp. 1–40. https://doi.org/10.1007/3-540-45734-8_1

Allan, I., Newman, H., Wilson, M., 2001. Antibacterial activity of particulate Bioglass® against supra- and subgingival bacteria. Biomaterials 22, 1683–1687. https://doi.org/10.1016/S0142-9612(00)00330-6

Allen, M.R., Burr, D.B., 2014. Techniques in Histomorphometry, in: Allen, M.R., Burr, D.B. (Eds.), Basic and Applied Bone Biology. Elsevier, pp. 131–148. https://doi.org/10.1016/B978-0-12-416015-6.00007-1

Alqurashi, H., Khurshid, Z., Syed, A.U.Y., Rashid Habib, S., Rokaya, D., Zafar, M.S., 2021. Polyetherketoneketone (PEKK): An emerging biomaterial for oral implants and dental prostheses. J. Adv. Res. 28, 87–95. https://doi.org/10.1016/j.jare.2020.09.004

Anastasio, R., Peerbooms, W., Cardinaels, R., van Breemen, L.C.A., 2019. Characterization of Ultraviolet-Cured Methacrylate Networks: From Photopolymerization to Ultimate Mechanical Properties. Macromolecules 52, 9220–9231. https://doi.org/10.1021/acs.macromol.9b01439

Anderson, M.A., 1993. A Comparison of Nonthreaded, Enhanced Threaded, and Ellis Fixation Pins Used in Type I External Skeletal Fixators in Dogs 8. https://doi.org/10.1111/j.1532-950X.1993.tb00425.x

Andersson, G.B.J., Lereim, P., Galante, J.O., Rostoker, W., 1982. Segmental Replacement of the Femur in Baboons with Fiber Metal Implants and Autologous Bone Grafts of Different Particle Size. Acta Orthop. Scand. 53, 349–354. https://doi.org/10.3109/17453678208992227

Antoniac, I., Popescu, D., Zapciu, A., Antoniac, A., Miculescu, F., Moldovan, H., 2019. Magnesium Filled Polylactic Acid (PLA) Material for Filament Based 3D Printing. Materials 12, 719. https://doi.org/10.3390/ma12050719

Antony, G.J.M., Jarali, C.S., Aruna, S.T., Raja, S., 2017. Tailored poly(ethylene) glycol dimethacrylate based shape memory polymer for orthopedic applications. J. Mech. Behav. Biomed. Mater. 65, 857–865. https://doi.org/10.1016/j.jmbbm.2016.10.011

Asgharzadeh, P., Röhrle, O., Willie, B.M., Birkhold, A.I., 2020. Decoding rejuvenating effects of mechanical loading on skeletal aging using in vivo μCT imaging and deep learning. Acta Biomater. 106, 193–207. https://doi.org/10.1016/j.actbio.2020.02.007

Asmussen, E., Peutzfeldt, A., 1998. Influence of UEDMA, BisGMA and TEGDMA on selected mechanical properties of experimental resin composites. Dent. Mater. 14, 51–56. https://doi.org/10.1016/S0109-5641(98)00009-8

Autefage, A., Palierne, S., Charron, C., Swider, P., 2012. Effective mechanical properties of diaphyseal cortical bone in the canine femur. Vet. J. 194, 202–209. https://doi.org/10.1016/j.tvjl.2012.04.001

Bagheri, Z.S., Tavakkoli Avval, P., Bougherara, H., Aziz, M.S.R., Schemitsch, E.H., Zdero, R., 2014. Biomechanical Analysis of a New Carbon Fiber/Flax/Epoxy Bone Fracture Plate Shows Less Stress Shielding Compared to a Standard Clinical Metal Plate. J. Biomech. Eng. 136, 091002. https://doi.org/10.1115/1.4027669

Bai, T., Zhu, B., Liu, H., Wang, Y., Song, G., Liu, C., Shen, C., 2020. Biodegradable poly(lactic acid) nanocomposites reinforced and toughened by carbon nanotubes/clay hybrids. Int. J. Biol. Macromol. 151, 628–634. https://doi.org/10.1016/j.ijbiomac.2020.02.209

Bair, H.E., Akinay, A.E., Menczel, J.D., Prime, R.B., Jaffe, M., 2009. Thermomechanical analysis (TMA) and thermodilatometry (TD), in: Menczel, J.D. (Ed.), Thermal Analysis of Polymers: Fundamentals and Applications. John Wiley, Hoboken, N.J.

Bander, N.B., Barnhart, M.D., Watson, A.T., Naber, S.J., 2018. Short-Term Prospective Clinical Evaluation of a Polyglycolic Acid Tibial Tuberosity Advancement Cage Implant. J. Am. Anim. Hosp. Assoc. 54, 85–94. https://doi.org/10.5326/JAAHA-MS-6532

Bandopadhyay, S., Bandyopadhyay, N., Ahmed, S., Yadav, V., Tekade, R.K., 2019. Current Research Perspectives of Orthopedic Implant Materials, in: Tekade, R.K. (Ed.), Biomaterials and Bionanotechnology. Elsevier, pp. 337–374. https://doi.org/10.1016/B978-0-12-814427-5.00010-X

Bandyopadhyay-Ghosh, S., Faria, P.E.P., Johnson, A., Felipucci, D.N.B., Reaney, I.M., Salata, L.A., Brook, I.M., Hatton, P.V., 2010. Osteoconductivity of modified fluorcanasite glass-ceramics for bone tissue augmentation and repair. J. Biomed. Mater. Res. A 94A, 760–768. https://doi.org/10.1002/jbm.a.32750

Barber, F.A., Dockery, W.D., 2006. Long-Term Absorption of Poly-L-Lactic Acid Interference Screws. Arthrosc. J. Arthrosc. Relat. Surg. 22, 820–826. https://doi.org/10.1016/j.arthro.2006.04.096

Barkarmo, S., Wennerberg, A., Hoffman, M., Kjellin, P., Breding, K., Handa, P., Stenport, V., 2013. Nano-hydroxyapatite-coated PEEK implants: A pilot study in rabbit bone. J. Biomed. Mater. Res. A 101A, 465–471. https://doi.org/10.1002/jbm.a.34358

Barnhart, M.D., Watson, A.T., Thatcher, L.G., Wotton, H., Naber, S.J., 2016. Prospective Randomized Clinical and Radiographic Evaluation of a Novel Bioabsorbable Biocomposite Tibial Tuberosity Advancement Cage Implant. Vet. Surg. 45, 651–658. https://doi.org/10.1111/vsu.12502

Baron, S., Ahearne, E., 2017. An investigation of force components in orthogonal cutting of medical grade cobalt–chromium alloy (ASTM F1537). Proc. Inst. Mech. Eng. [H] 231, 269–275. https://doi.org/10.1177/0954411917690181

Baron, S., Ahearne, E., Connolly, P., Keaveney, S., Byrne, G., 2015. An Assessment of Medical Grade Cobalt Chromium Alloy ASTM F1537 as a "Difficult-to-Cut (DTC)" Material, in: The Proceedings of MTTRF 2015 Annual Meeting. Presented at the MTTRF/IAM-CNC Annual Meeting, San Francisco, CA, USA, p. 6.

Becker, T., Weigl, D., Mercado, E., Katz, K., Bar-On, E., 2012. Fractures and Refractures After Femoral Locking Compression Plate Fixation in Children and Adolescents. J. Pediatr. Orthop. 32, e40–e46. https://doi.org/10.1097/BPO.0b013e318264496a

Bergstrom, J., 2015. Mechanics of solid polymers: theory and computational modeling. Elsevier, Amsterdam.

Bhan, A., Qiu, S., Rao, S.D., 2018. Bone histomorphometry in the evaluation of osteomalacia. Bone Rep. 8, 125–134. https://doi.org/10.1016/j.bonr.2018.03.005

Boccaccini, A., Maquet, V., 2003. Bioresorbable and bioactive polymer/Bioglass® composites with tailored pore structure for tissue engineering applications. Compos. Sci. Technol. 63, 2417–2429. https://doi.org/10.1016/S0266-3538(03)00275-6

Bodnárová, S., Gromošová, S., Hudák, R., Rosocha, J., Živčák, J., Plšíková, J., Vojtko, M., Tóth, T., Harvanová, D., Ižariková, G., Danišovič, Ľ., 2019. 3D printed Polylactid Acid based porous scaffold for bone tissue engineering: an in vitro study. Acta Bioeng. Biomech. 21, 101–110. https://doi.org/10.37190/ABB-01407-2019-02

Boriani, S., Tedesco, G., Ming, L., Ghermandi, R., Amichetti, M., Fossati, P., Krengli, M., Mavilla, L., Gasbarrini, A., 2018. Carbon-fiber-reinforced PEEK fixation system in the treatment of spine tumors: a preliminary report. Eur. Spine J. 27, 874–881. https://doi.org/10.1007/s00586-017-5258-5

Bose, S., Vahabzadeh, S., Bandyopadhyay, A., 2013. Bone tissue engineering using 3D printing. Mater. Today 16, 496–504. https://doi.org/10.1016/j.mattod.2013.11.017

Böstman, O.M., Pihlajamäki, H.K., 2000. Adverse Tissue Reactions to Bioabsorbable Fixation Devices: Clin. Orthop. 371, 216–227. https://doi.org/10.1097/00003086-200002000-00026

Bouler, J.M., Pilet, P., Gauthier, O., Verron, E., 2017. Biphasic calcium phosphate ceramics for bone reconstruction: A review of biological response. Acta Biomater. 53, 1–12. https://doi.org/10.1016/j.actbio.2017.01.076

Bradley, J.S., Hastings, G.W., 1980. Carbon Fibre Reinforced Plastics for Load-Bearing Implants. Eng. Med. 9, 127–130. https://doi.org/10.1243/EMED_JOUR_1980_009_033_02

Brie, J., Chartier, T., Chaput, C., Delage, C., Pradeau, B., Caire, F., Boncoeur, M.-P., Moreau, J.-J., 2013. A new custom made bioceramic implant for the repair of large and complex craniofacial bone defects. J. Cranio-Maxillofac. Surg. 41, 403–407. https://doi.org/10.1016/j.jcms.2012.11.005

Brinson, H.F., Brinson, L.C., 2015. Polymer Engineering Science and Viscoelasticity. Springer US, Boston, MA. https://doi.org/10.1007/978-1-4899-7485-3

Brockett, C.L., Carbone, S., Fisher, J., Jennings, L.M., 2017. PEEK and CFR-PEEK as alternative bearing materials to UHMWPE in a fixed bearing total knee replacement: An experimental wear study. Wear 374–375, 86–91. https://doi.org/10.1016/j.wear.2016.12.010

Castilho, M., Dias, M., Vorndran, E., Gbureck, U., Fernandes, P., Pires, I., Gouveia, B., Armés, H., Pires, E., Rodrigues, J., 2014. Application of a 3D printed customized implant for canine cruciate

ligament treatment by tibial tuberosity advancement. Biofabrication 6, 025005. https://doi.org/10.1088/1758-5082/6/2/025005

Castilho, M., Rodrigues, J., Vorndran, E., Gbureck, U., Quental, C., Folgado, J., Fernandes, P.R., 2017. Computational design and fabrication of a novel bioresorbable cage for tibial tuberosity advancement application. J. Mech. Behav. Biomed. Mater. 65, 344–355. https://doi.org/10.1016/j.jmbbm.2016.08.036

Cengiz, I.F., Oliveira, J.M., Reis, R.L., 2018. Micro-CT – a digital 3D microstructural voyage into scaffolds: a systematic review of the reported methods and results. Biomater. Res. 22, 11pp. https://doi.org/10.1186/s40824-018-0136-8

Chen, H., Wu, D., Yang, H., Guo, K., 2015. Clinical Use of 3D Printing Guide Plate in Posterior Lumbar Pedicle Screw Fixation. Med. Sci. Monit. 21, 3948–3954. https://doi.org/10.12659/MSM.895597

Chen, H., Zhang, Y., Kalra, M.K., Lin, F., Chen, Y., Liao, P., Zhou, J., Wang, G., 2017. Low-Dose CT With a Residual Encoder-Decoder Convolutional Neural Network. IEEE Trans. Med. Imaging 36, 2524–2535. https://doi.org/10.1109/TMI.2017.2715284

Chen, J., Tan, L., Yu, X., Etim, I.P., Ibrahim, M., Yang, K., 2018. Mechanical properties of magnesium alloys for medical application: A review. J. Mech. Behav. Biomed. Mater. 87, 68–79. https://doi.org/10.1016/j.jmbbm.2018.07.022

Chiu, R., Ma, T., Smith, R.L., Goodman, S.B., 2006. Polymethylmethacrylate particles inhibit osteoblastic differentiation of bone marrow osteoprogenitor cells. J. Biomed. Mater. Res. A 77A, 850–856. https://doi.org/10.1002/jbm.a.30697

Choppadandi, M., More, N., Kapusetti, G., 2019. Detoxification of poly(methyl methacrylate) bone cement by natural antioxidant intervention. J. Biomed. Mater. Res. A 107, 2835–2847. https://doi.org/10.1002/jbm.a.36785

Choy, W.J., Mobbs, R.J., Wilcox, B., Phan, S., Phan, K., Sutterlin, C.E., 2017. Reconstruction of Thoracic Spine Using a Personalized 3D-Printed Vertebral Body in Adolescent with T9 Primary Bone Tumor. World Neurosurg. 105, 1032.e13-1032.e17. https://doi.org/10.1016/j.wneu.2017.05.133

Chye Joachim Loo, S., Ooi, C.P., Hong Elyna Wee, S., Chiang Freddy Boey, Y., 2005. Effect of isothermal annealing on the hydrolytic degradation rate of poly(lactide-co-glycolide) (PLGA). Biomaterials 26, 2827–2833. https://doi.org/10.1016/j.biomaterials.2004.08.031

Cifuentes, S.C., Frutos, E., Benavente, R., Lorenzo, V., González-Carrasco, J.L., 2017. Assessment of mechanical behavior of PLA composites reinforced with Mg micro-particles through depth-sensing indentations analysis. J. Mech. Behav. Biomed. Mater. 65, 781–790. https://doi.org/10.1016/j.jmbbm.2016.09.013

Clark, D.P., Badea, C.T., 2021. Advances in micro-CT imaging of small animals. Phys. Med. 88, 175–192. https://doi.org/10.1016/j.ejmp.2021.07.005

Colquhoun, R., Tanner, K.E., 2015. Mechanical behaviour of degradable phosphate glass fibres and composites—a review. Biomed. Mater. 11, 014105. https://doi.org/10.1088/1748-6041/11/1/014105

Compston, J., Skingle, L., Dempster, D.W., 2018. Bone Histomorphometry, in: Feldman, D. (Ed.), Vitamin D. Elsevier, pp. 959–973. https://doi.org/10.1016/B978-0-12-809965-0.00053-7

Coulembier, O., Degée, P., Hedrick, J.L., Dubois, P., 2006. From controlled ring-opening polymerization to biodegradable aliphatic polyester: Especially poly(β-malic acid) derivatives. Prog. Polym. Sci. 31, 723–747. https://doi.org/10.1016/j.progpolymsci.2006.08.004

Cowin, S.C. (Ed.), 2001. Bone mechanics handbook, 2nd ed. ed. CRC Press, Boca Raton, FL.

Cronskär, M., Rännar, L.-E., Bäckström, M., Nilsson, K.G., Samuelsson, B., 2015. Patient-Specific Clavicle Reconstruction Using Digital Design and Additive Manufacturing. J. Mech. Des. 137, 111418. https://doi.org/10.1115/1.4030992

Crovace, M.C., Souza, M.T., Chinaglia, C.R., Peitl, O., Zanotto, E.D., 2016. Biosilicate® — A multipurpose, highly bioactive glass-ceramic. In vitro, in vivo and clinical trials. J. Non-Cryst. Solids 432A, 90–110. https://doi.org/10.1016/j.jnoncrysol.2015.03.022

Cubo, J., Casinos, A., 2000. Incidence and mechanical significance of pneumatization in the long bones of birds. Zool. J. Linn. Soc. 130, 499–510. https://doi.org/10.1111/j.1096-3642.2000.tb02198.x

Daculsi, G., Goyenvalle, E., Cognet, R., Aguado, E., Suokas, E.O., 2011. Osteoconductive properties of poly(96L/4D-lactide)/beta-tricalcium phosphate in long term animal model. Biomaterials 32, 3166–3177. https://doi.org/10.1016/j.biomaterials.2011.01.033

De Aza, P.N., De Aza, A.H., Pena, P., De Aza, S., 2007. Bioactive glasses and glass-ceramics. Bol. Soc. Esp. Cerámica Vidr. 46, 45–55.

den Boer, F.C., Patka, P., Bakker, F.C., Wippermann, B.W., van Lingen, A., Vink, G.Q.M., Boshuizen, K., Haarman, H.J.Th.M., 1999. New segmental long bone defect model in sheep: Quantitative analysis of healing with dual energy X-ray absorptiometry. J. Orthop. Res. 17, 654–660. https://doi.org/10.1002/jor.1100170506

Díez-Pascual, A.M., Naffakh, M., Gómez, M.A., Marco, C., Ellis, G., Martínez, M.T., Ansón, A., González-Domínguez, J.M., Martínez-Rubi, Y., Simard, B., 2009. Development and characterization of PEEK/carbon nanotube composites. Carbon 47, 3079–3090. https://doi.org/10.1016/j.carbon.2009.07.020

Díez-Pascual, A.M., Naffakh, M., González-Domínguez, J.M., Ansón, A., Martínez-Rubi, Y., Martínez, M.T., Simard, B., Gómez, M.A., 2010. High performance PEEK/carbon nanotube composites compatibilized with polysulfones-II. Mechanical and electrical properties. Carbon 48, 3500–3511. https://doi.org/10.1016/j.carbon.2010.05.050

Distler, T., Fournier, N., Grünewald, A., Polley, C., Seitz, H., Detsch, R., Boccaccini, A.R., 2020. Polymer-Bioactive Glass Composite Filaments for 3D Scaffold Manufacturing by Fused Deposition Modeling: Fabrication and Characterization. Front. Bioeng. Biotechnol. 8, 552. https://doi.org/10.3389/fbioe.2020.00552

Doblaré, M., García, J.M., Cegoñino, J., 2002. Development of an Internal Bone Remodelling Theory and Applications to Some Problems in Orthopaedic Biomechanics. Mecc. Int. J. Theor. Appl. Mech. 37, 365–374. https://doi.org/10.1023/A:1020835720405

Dong, Y., Ruan, Y., Wang, H., Zhao, Y., Bi, D., 2004. Studies on glass transition temperature of chitosan with four techniques. J. Appl. Polym. Sci. 93, 1553–1558. https://doi.org/10.1002/app.20630

Drago, L., Toscano, M., Bottagisio, M., 2018. Recent Evidence on Bioactive Glass Antimicrobial and Antibiofilm Activity: A Mini-Review. Materials 11, 326. https://doi.org/10.3390/ma11020326

Dumitriu, S. (Ed.), 2002. Polymeric biomaterials, 2nd ed., rev.expanded. ed. Marcel Dekker, Inc, New York.

Eichhorn, J., Elschner, C., Groß, M., Reichenbächer, R., Martín, A.X.H., Soares, A.P., Fischer, H., Kulkova, J., Moritz, N., Hupa, L., Stommel, M., Scheffler, C., Kilo, M., 2021. Spinning of Endless Bioactive Silicate Glass Fibres for Fibre Reinforcement Applications. Appl. Sci. 11, 7927. https://doi.org/10.3390/app11177927

Einhorn, T.A., 1998. The Cell and Molecular Biology of Fracture Healing: Clin. Orthop. 355S, S7–S21. https://doi.org/10.1097/00003086-199810001-00003

Elhattab, K., Bhaduri, S.B., Lawrence, J.G., Sikder, P., 2021. Fused Filament Fabrication (Three-Dimensional Printing) of Amorphous Magnesium Phosphate/Polylactic Acid Macroporous Biocomposite Scaffolds. ACS Appl. Bio Mater. 4, 3276–3286. https://doi.org/10.1021/acsabm.0c01620

Eliades, T., Voutsa, D., Sifakakis, I., Makou, M., Katsaros, C., 2011. Release of bisphenol-A from a light-cured adhesive bonded to lingual fixed retainers. Am. J. Orthod. Dentofacial Orthop. 139, 192–195. https://doi.org/10.1016/j.ajodo.2009.12.026

Elsawy, M.A., Kim, K.-H., Park, J.-W., Deep, A., 2017. Hydrolytic degradation of polylactic acid (PLA) and its composites. Renew. Sustain. Energy Rev. 79, 1346–1352. https://doi.org/10.1016/j.rser.2017.05.143

Emami, N., Söderholm, K.-J.M., 2005. Influence of light-curing procedures and photo-initiator/co-initiator composition on the degree of conversion of light-curing resins. J. Mater. Sci. Mater. Med. 16, 47–52. https://doi.org/10.1007/s10856-005-6445-1

Engelberg, I., Kohn, J., 1990. Physico-mechanicaplroperties of degradablepolymersused in medical applications:a comparativestudy. Biomaterials 12, 292–304. https://doi.org/10.1016/0142-9612(91)90037-B

Erben, R.G., Glösmann, M., 2019. Histomorphometry in Rodents, in: Idris, A.I. (Ed.), Bone Research Protocols, Methods in Molecular Biology. Springer New York, New York, NY, pp. 411–435. https://doi.org/10.1007/978-1-4939-8997-3_24

Espalin, D., Arcaute, K., Rodriguez, D., Medina, F., Posner, M., Wicker, R., 2010. Fused deposition modeling of patient-specific polymethylmethacrylate implants. Rapid Prototyp. J. 16, 164–173. https://doi.org/10.1108/13552541011034825

Etchepareborde, S., Barthelemy, N., Brunel, L., Claeys, S., Balligand, M., 2014. Biomechanical testing of a β-tricalcium phosphate wedge for advancement of the tibial tuberosity. Vet. Comp. Orthop. Traumatol. 27, 14–19. https://doi.org/10.3415/VCOT-13-04-0053

Evans, S.L., Gregson, P.J., 1998. Composite technology in load-bearing orthopaedic implants. Biomaterials 19, 1329–1342. https://doi.org/10.1016/S0142-9612(97)00217-2

Feerick, E.M., Liu, X. (Cheryl), McGarry, P., 2013. Anisotropic mode-dependent damage of cortical bone using the extended finite element method (XFEM). J. Mech. Behav. Biomed. Mater. 20, 77–89. https://doi.org/10.1016/j.jmbbm.2012.12.004

Ferguson, S.J., Visser, J.M.A., Polikeit, A., 2006. The long-term mechanical integrity of non-reinforced PEEK-OPTIMA polymer for demanding spinal applications: experimental and finite-element analysis. Eur. Spine J. 15, 149–156. https://doi.org/10.1007/s00586-005-0915-5

Ferizi, U., Honig, S., Chang, G., 2019. Artificial intelligence, osteoporosis and fragility fractures. Curr. Opin. Rheumatol. 31, 368–375. https://doi.org/10.1097/BOR.0000000000000607

Frost, H.M., 2003. Bone's mechanostat: A 2003 update. Anat. Rec. 275A, 1081–1101. https://doi.org/10.1002/ar.a.10119

Furuse, A.Y., Mondelli, J., Watts, D.C., 2011. Network structures of Bis-GMA/TEGDMA resins differ in DC, shrinkage-strain, hardness and optical properties as a function of reducing agent. Dent. Mater. 27, 497–506. https://doi.org/10.1016/j.dental.2011.02.007

Garcia-Leiner, M., Ghita, O., McKay, R., Kurtz, S.M., 2019. Additive Manufacturing of Polyaryletherketones, in: Kurtz, S.M. (Ed.), PEEK Biomaterials Handbook. Elsevier, pp. 89–103. https://doi.org/10.1016/B978-0-12-812524-3.00007-7

Gautschi, O.P., Schlett, C.L., Fournier, J.-Y., Cadosch, D., 2010. Laboratory confirmed polymethyl-methacrylate (Palacos®)-hypersensitivity after cranioplasty. Clin. Neurol. Neurosurg. 112, 915–916. https://doi.org/10.1016/j.clineuro.2010.07.013

Gibson, R.F., 2016. Principles of Composite Material Mechanics, 4th ed. CRC Press, Boca Raton.

Gillett, N., Brown, S., Dumbleton, J., Pool, R., 1985. The use of short carbon fibre reinforced thermoplastic plates for fracture fixation. Biomaterials 6, 113–121. https://doi.org/10.1016/0142-9612(85)90074-2

Gioka, C., Bourauel, C., Hiskia, A., Kletsas, D., Eliades, T., Eliades, G., 2005. Light-cured or chemically cured orthodontic adhesive resins? A selection based on the degree of cure, monomer leaching, and cytotoxicity. Am. J. Orthod. Dentofacial Orthop. 127, 413–419. https://doi.org/10.1016/j.ajodo.2004.02.015

Glant, T.T., Jacobs, J.J., Molnár, G., Shanbhag, A.S., Valyon, M., Galante, J.O., 1993. Bone resorption activity of particulate-stimulated macrophages. J. Bone Miner. Res. 8, 1071–1079. https://doi.org/10.1002/jbmr.5650080907

Gliesche, K., Hübner, T., Orawetz, H., 2003. Application of the tailored fibre placement (TFP) process for a local reinforcement on an “open-hole” tension plate from carbon/epoxy laminates. Compos. Sci. Technol. 63, 81–88. https://doi.org/10.1016/S0266-3538(02)00178-1

Gregor, A., Filová, E., Novák, M., Kronek, J., Chlup, H., Buzgo, M., Blahnová, V., Lukášová, V., Bartoš, M., Nečas, A., Hošek, J., 2017. Designing of PLA scaffolds for bone tissue replacement fabricated by ordinary commercial 3D printer. J. Biol. Eng. 11, 31. https://doi.org/10.1186/s13036-017-0074-3

Grijpma, D.W., Hou, Q., Feijen, J., 2005. Preparation of biodegradable networks by photo-crosslinking lactide, ε-caprolactone and trimethylene carbonate-based oligomers functionalized with fumaric acid monoethyl ester. Biomaterials 26, 2795–2802. https://doi.org/10.1016/j.biomaterials.2004.08.002

Grinberg, N., Rodriguez, S. (Eds.), 2019. Ewing’s Analytical Instrumentation Handbook, 4th ed. CRC Press/Taylor & Francis Group, Boca Raton. https://doi.org/10.1201/9781315118024

Gutwald, R., Schön, R., Gellrich, N.-C., Schramm, A., Schmelzeisen, R., Pistner, H., 2002. Bioresorbable implants in maxillo-facial osteosynthesis: experimental and clinical experience. Injury 33, 4–16. https://doi.org/10.1016/S0020-1383(02)00127-4

Hambli, R., Frikha, S., Toumi, H., Tavares, J.M.R.S., 2016. Finite element prediction of fatigue damage growth in cancellous bone. Comput. Methods Biomech. Biomed. Engin. 19, 563–570. https://doi.org/10.1080/10255842.2015.1048687

Han, X., Yang, D., Yang, C., Spintzyk, S., Scheideler, L., Li, P., Li, D., Geis-Gerstorfer, J., Rupp, F., 2019. Carbon Fiber Reinforced PEEK Composites Based on 3D-Printing Technology for Orthopedic and Dental Applications. J. Clin. Med. 8, 240. https://doi.org/10.3390/jcm8020240

Han, Y., Ye, J.C., 2018. Framing U-Net via Deep Convolutional Framelets: Application to Sparse-view CT. IEEE Trans. Med. Imaging 37, 1418–1429. https://doi.org/10.1109/TMI.2018.2823768

Harasen, G., 2003. Common long bone fractures in small animal practice — Part 1. Can. Vet. J. 44, 333–334.

Hasegawa, T., Ushirozako, H., Shigeto, E., Ohba, T., Oba, H., Mukaiyama, K., Shimizu, S., Yamato, Y., Ide, K., Shibata, Y., Ojima, T., Takahashi, J., Haro, H., Matsuyama, Y., 2020. The Titanium-coated PEEK Cage Maintains Better Bone Fusion With the Endplate Than the PEEK Cage 6 Months After PLIF Surgery: A Multicenter, Prospective, Randomized Study. Spine 45, E892–E902. https://doi.org/10.1097/BRS.0000000000003464

Hayashi, K., Manley, P.A., Muir, P., 2004. Cranial Cruciate Ligament Pathophysiology in Dogs With Cruciate Disease: A Review. J. Am. Anim. Hosp. Assoc. 40, 385–390. https://doi.org/10.5326/0400385

He, J., Söderling, E., Lassila, L.V.J., Vallittu, P.K., 2014. Synthesis of antibacterial and radio-opaque dimethacrylate monomers and their potential application in dental resin. Dent. Mater. 30, 968–976. https://doi.org/10.1016/j.dental.2014.05.013

Heikkilä, J.T., Aho, H.J., Yli-urpo, A., Happonen, R.-P., Aho, A.J., 1995. Bone formation in rabbit cancellous bone defects filled with bioactive glass granules. Acta Orthop. Scand. 66, 463–467. https://doi.org/10.3109/17453679508995588

Hench, Kokubo, 1998. Properties of bioactive glasses and glass-ceramics, in: Black, J., Hastings, G. (Eds.), Handbook of Biomaterial Properties. Chapman & Hall, London.

Hench, L.L., 2006. The story of Bioglass®. J. Mater. Sci. Mater. Med. 17, 967–978. https://doi.org/10.1007/s10856-006-0432-z

Hench, L.L., Polak, J.M., 2002. Third-Generation Biomedical Materials. Science 295, 1014–1017. https://doi.org/10.1126/science.1067404

Hench, L.L., Splinter, R.J., Allen, W.C., Greenlee, T.K., 1971. Bonding mechanisms at the interface of ceramic prosthetic materials. J. Biomed. Mater. Res. 5, 117–141. https://doi.org/10.1002/jbm.820050611

Henderson, D., Sinha, S., 2020. OssDsign cranioplasty in children: a single-centre experience. Childs Nerv. Syst. 36, 1773–1776. https://doi.org/10.1007/s00381-020-04584-9

Henton, D.E., Gruber, P., Lunt, J., Randall, J., 2005. Polylactic Acid Technology, in: Mohanty, A.K., Misra, M., Drzal, L.T. (Eds.), Natural Fibers, Biopolymers, and Biocomposites. CRC Press, pp. 527–577.

Hollevoet, N., Verdonk, R., 2003. Outcome of distal radius fractures in relation to bone mineral density. Acta Orthop. Belg. 69, 510–514.

Hollevoet, N., Verdonk, R., Kaufman, J.-M., Goemaere, S., 2011. Osteoporotic fracture treatment. Acta Orthop. Belg. 77, 441–447.

Hoppe, A., Güldal, N.S., Boccaccini, A.R., 2011. A review of the biological response to ionic dissolution products from bioactive glasses and glass-ceramics. Biomaterials 32, 2757–2774. https://doi.org/10.1016/j.biomaterials.2011.01.004

Hoppe, A., Meszaros, R., Stähli, C., Romeis, S., Schmidt, J., Peukert, W., Marelli, B., Nazhat, S.N., Wondraczek, L., Lao, J., Jallot, E., Boccaccini, A.R., 2013. In vitro reactivity of Cu doped 45S5 Bioglass® derived scaffolds for bone tissue engineering. J. Mater. Chem. B 1, 5659. https://doi.org/10.1039/c3tb21007c

Hu, Y., Shang, Q., Tang, J., Wang, C., Zhang, F., Jia, P., Feng, G., Wu, Q., Liu, C., Hu, L., Lei, W., Zhou, Y., 2018. Use of cardanol-based acrylate as reactive diluent in UV-curable castor oil-based polyurethane acrylate resins. Ind. Crops Prod. 117, 295–302. https://doi.org/10.1016/j.indcrop.2018.02.053

Huang, G.J., Zhong, S., Susarla, S.M., Swanson, E.W., Huang, J., Gordon, C.R., 2015. Craniofacial Reconstruction With Poly(Methyl Methacrylate) Customized Cranial Implants. J. Craniofac. Surg. 26, 64–70. https://doi.org/10.1097/SCS.0000000000001315

Hulsen, D.J., van Gestel, N.A., Geurts, J.A.P., Arts, J.J.C., 2017. S53P4 bioactive glass, in: Arts, J.J.C., Geurts, J. (Eds.), Management of Periprosthetic Joint Infections (PJIs). Elsevier, pp. 69–80. https://doi.org/10.1016/B978-0-08-100205-6.00004-5

Ifkovits, J.L., Burdick, J.A., 2007. Review: Photopolymerizable and Degradable Biomaterials for Tissue Engineering Applications. Tissue Eng. 13, 2369–2385. https://doi.org/10.1089/ten.2007.0093

Jain, R., Shukla, B.P., Nema, S., Shukla, S., Chabra, D., Karmore, S.K., 2018. Incidence of fracture in dog: A retrospective study. Vet. Pract. 19, 63–65.

Jaszkiewicz, A., Bledzki, A.K., Franciszczak, P., 2013. Improving the mechanical performance of PLA composites with natural, man-made cellulose and glass fibers — a comparison to PP counterparts. Polimery 58, 435–442. https://doi.org/10.14314/polimery.2013.435

Jockisch, K.A., Brown, S.A., Bauer, T.W., Merritt, K., 1992. Biological response to chopped-carbon-fiber-reinforced peek. J. Biomed. Mater. Res. 26, 133–146. https://doi.org/10.1002/jbm.820260202

Johnson, J., Austin, C., Breur, G., 1994. Incidence of Canine Appendicular Musculoskeletal Disorders in 16 Veterinary Teaching Hospitals from 1980 through 1989. Vet. Comp. Orthop. Traumatol. 7, 56–69. https://doi.org/10.1055/s-0038-1633097

Jones, J.R., 2013. Review of bioactive glass: From Hench to hybrids. Acta Biomater. 9, 4457–4486.

Jones, J.R., Ehrenfried, L.M., Saravanapavan, P., Hench, L.L., 2006. Controlling ion release from bioactive glass foam scaffolds with antibacterial properties. J. Mater. Sci. Mater. Med. 17, 989–996. https://doi.org/10.1007/s10856-006-0434-x

Kabiri, A., Liaghat, G., Alavi, F., 2021. Biomechanical evaluation of glass fiber/polypropylene composite bone fracture fixation plates: Experimental and numerical analysis. Comput. Biol. Med. 132, 104303. https://doi.org/10.1016/j.compbiomed.2021.104303

Kandola, B.K., Pornwannachai, W., Ebdon, J.R., 2020. Flax/PP and Flax/PLA Thermoplastic Composites: Influence of Fire Retardants on the Individual Components. Polymers 12, 2452. https://doi.org/10.3390/polym12112452

Kandziora, F., Schollmeier, G., Scholz, M., Schaefer, J., Scholz, A., Schmidmaier, G., Schröder, R., Bail, H., Duda, G., Mittlmeier, T., Haas, N.P., 2002. Influence of cage design on interbody fusion

in a sheep cervical spine model. J. Neurosurg. Spine 96, 321–332. https://doi.org/10.3171/spi.2002.96.3.0321

Kanerva, L., Jolanki, R., Estlander, T., 1997. 10 years of patch testing with the (meth)acrylate series. Contact Dermatitis 37, 255–258. https://doi.org/10.1111/j.1600-0536.1997.tb02460.x

Kanno, T., Sukegawa, S., Furuki, Y., Nariai, Y., Sekine, J., 2018. Overview of innovative advances in bioresorbable plate systems for oral and maxillofacial surgery. Jpn. Dent. Sci. Rev. 54, 127–138. https://doi.org/10.1016/j.jdsr.2018.03.003

Kapatkin, A.S., Arbittier, G., Kass, P.H., Gilley, R.S., Smith, G.K., 2007. Kinetic Gait Analysis of Healthy Dogs on Two Different Surfaces. Vet. Surg. 36, 605–608. https://doi.org/10.1111/j.1532-950X.2007.00311.x

Kassen, D., Lath, D., Lach, A., Evans, H., Chantry, A., Rabin, N., Croucher, P., Yong, K.L., 2016. Myeloma impairs mature osteoblast function but causes early expansion of osteo-progenitors: temporal changes in bone physiology and gene expression in the KMS12BM model. Br. J. Haematol. 172, 64–79. https://doi.org/10.1111/bjh.13790

Kelly, B., Heyworth, B., Yen, Y.-M., Hedequist, D., 2013. Adverse Sequelae Due to Plate Retention Following Submuscular Plating for Pediatric Femur Fractures. J. Orthop. Trauma 27, 726–729. https://doi.org/10.1097/BOT.0b013e31829089e1

Kersten, R.F.M.R., van Gaalen, S.M., de Gast, A., Öner, F.C., 2015. Polyetheretherketone (PEEK) cages in cervical applications: a systematic review. Spine J. 15, 1446–1460. https://doi.org/10.1016/j.spinee.2013.08.030

Kettunen, J., Mäkelä, A., Miettinen, H., Nevalainen, T., Heikkilä, M., Törmälä, P., Rokkanen, P., 1999a. Fixation of femoral shaft osteotomy with an intramedullary composite rod: An experimental study on dogs with a two-year follow-up. J. Biomater. Sci. Polym. Ed. 10, 33–45. https://doi.org/10.1163/156856299X00261

Kettunen, J., Mäkelä, A., Miettinen, H., Nevalainen, T., Heikkilä, M., Törmälä, P., Rokkanen, P., 1999b. Fixation of distal femoral osteotomy with an intramedullary rod: Early failure of carbon fibre composite implant in rabbits. J. Biomater. Sci. Polym. Ed. 10, 715–728. https://doi.org/10.1163/156856299x00603

Kim, J.M., Kim, M.H., Kang, S.S., Kim, G., Choi, S.H., 2014. Comparable bone healing capacity of different bone graft matrices in a rabbit segmental defect model. J. Vet. Sci. 15, 289–295. https://doi.org/10.4142/jvs.2014.15.2.289

Kingery, W.D., Bowen, H.K., Uhlmann, D.R., 1976. Introduction to ceramics, 2d ed, Wiley series on the science and technology of materials. Wiley, New York.

Kluess, D., Wieding, J., Souffrant, R., Mittelmeier, W., Bader, R., 2010. Finite Element Analysis in Orthopaedic Biomechanics, in: Moratal, D. (Ed.), Finite Element Analysis. Intechopen, pp. 151–170.

Kohler, R., Tastad, C.A., Creecy, A., Wallace, J.M., 2021. Morphological and mechanical characterization of bone phenotypes in the Amish G610C murine model of osteogenesis imperfecta. PLOS One 16, e0255315. https://doi.org/10.1371/journal.pone.0255315

Kokubo, T., Takadama, H., 2006. How useful is SBF in predicting in vivo bone bioactivity? Biomaterials 27, 2907–2915. https://doi.org/10.1016/j.biomaterials.2006.01.017

Kotz, F., Mader, M., Dellen, N., Risch, P., Kick, A., Helmer, D., Rapp, B., 2020. Fused Deposition Modeling of Microfluidic Chips in Polymethylmethacrylate. Micromachines 11, 873. https://doi.org/10.3390/mi11090873

Kruyt, M.C., Dhert, W.J.A., Yuan, H., Wilson, C.E., van Blitterswijk, C.A., Verbout, A.J., de Bruijn, J.D., 2004. Bone tissue engineering in a critical size defect compared to ectopic implantations in the goat. J. Orthop. Res. 22, 544–551. https://doi.org/10.1016/j.orthres.2003.10.010

Kulkova, J., Moritz, N., Huhtinen, H., Mattila, R., Donati, I., Marsich, E., Paoletti, S., Vallittu, P.K., 2016. Bioactive glass surface for fiber reinforced composite implants via surface etching by Excimer laser. Med. Eng. Phys. 38, 664–670. https://doi.org/10.1016/j.medengphy.2016.04.003

Kulkova, Y., 2020. Bone implant. EP3370792B1.

Kumar, G.S., Rajendran, S., Karthi, S., Govindan, R., Girija, E.K., Karunakaran, G., Kuznetsov, D., 2017. Green synthesis and antibacterial activity of hydroxyapatite nanorods for orthopedic applications. MRS Commun. 7, 183–188. https://doi.org/10.1557/mrc.2017.18

Kunze, C., Freier, T., Helwig, E., Sandner, B., Reif, D., Wutzler, A., Radusch, H.-J., 2003. Surface modification of tricalcium phosphate for improvement of the interfacial compatibility with biodegradable polymers. Biomaterials 24, 967–974. https://doi.org/10.1016/S0142-9612(02)00433-7

Kurtz, S.M. (Ed.), 2019. PEEK Biomaterials Handbook, 2nd ed. Elsevier/William Andrew.

Kusakabe, H., Sakamaki, T., Nihei, K., Oyama, Y., Yanagimoto, S., Ichimiya, M., Kimura, J., Toyama, Y., 2004. Osseointegration of a hydroxyapatite-coated multilayered mesh stem. Biomaterials 25, 2957–2969. https://doi.org/10.1016/j.biomaterials.2003.09.090

Lacroix, D., Prendergast, P.J., 2002. A mechano-regulation model for tissue differentiation during fracture healing: analysis of gap size and loading. J. Biomech. 35, 1163–1171. https://doi.org/10.1016/S0021-9290(02)00086-6

Lassila, L.V.J., Nohrström, T., Vallittu, P.K., 2002. The influence of short-term water storage on the flexural properties of unidirectional glass fiber-reinforced composites. Biomaterials 23, 2221–2229. https://doi.org/10.1016/S0142-9612(01)00355-6

Laux, C.J., Hodel, S.M., Farshad, M., Müller, D.A., 2018. Carbon fibre/polyether ether ketone (CF/PEEK) implants in orthopaedic oncology. World J. Surg. Oncol. 16, 241. https://doi.org/10.1186/s12957-018-1545-9

Lee, J.-H., Kwon, J.-S., Moon, S.-K., Uhm, S.-H., Choi, B.-H., Joo, U.-H., Kim, K.-M., Kim, K.-N., 2016. Titanium-Silver Alloy Miniplates for Mandibular Fixation: In Vitro and In Vivo Study. J. Oral Maxillofac. Surg. 74, 1622.e1-1622.e12. https://doi.org/10.1016/j.joms.2016.04.010

Lee, Y.-C., Chan, Y.-H., Hsieh, S.-C., Lew, W.-Z., Feng, S.-W., 2019. Comparing the Osteogenic Potentials and Bone Regeneration Capacities of Bone Marrow and Dental Pulp Mesenchymal Stem Cells in a Rabbit Calvarial Bone Defect Model. Int. J. Mol. Sci. 20, 5015. https://doi.org/10.3390/ijms20205015

Lehtonen, T., Tuominen, J., Hiekkanen, E., 2013a. Resorbable composites with bioresorbable glass fibers for load-bearing applications. In vitro degradation and degradation mechanism. Acta Biomater. 9, 4868–4877. https://doi.org/10.1016/j.actbio.2012.08.052

Lehtonen, T., Tuominen, J., Hiekkanen, E., 2013b. Dissolution behavior of high strength bioresorbable glass fibers manufactured by continuous fiber drawing. J. Mech. Behav. Biomed. Mater. 20, 376–386. https://doi.org/10.1016/j.jmbbm.2013.01.032

Li, B., Webster, T. (Eds.), 2018. Orthopedic Biomaterials: Progress in Biology, Manufacturing, and Industry Perspectives. Springer International Publishing, Cham. https://doi.org/10.1007/978-3-319-89542-0

Li, J., Habibovic, P., Vandendoel, M., Wilson, C., Dewijn, J., Vanblitterswijk, C., Degroot, K., 2007. Bone ingrowth in porous titanium implants produced by 3D fiber deposition. Biomaterials 28, 2810–2820. https://doi.org/10.1016/j.biomaterials.2007.02.020

Li, S.M., Garreau, H., Vert, M., 1990. Structure-property relationships in the case of the degradation of massive aliphatic poly-(α-hydroxy acids) in aqueous media. Part 1: Poly(DL-lactic acid). J. Mater. Sci. Mater. Med. 1, 123–130. https://doi.org/10.1007/BF00700871

Li, Y., Wu, Z., Li, X., Guo, Z., Wu, S., Zhang, Y., Shi, L., Teoh, S., Liu, Y., Zhang, Z., 2014. A polycaprolactone-tricalcium phosphate composite scaffold as an autograft-free spinal fusion cage in a sheep model. Biomaterials 35, 5647–5659. https://doi.org/10.1016/j.biomaterials.2014.03.075

Liao, C., Li, Y., Tjong, S., 2018. Graphene Nanomaterials: Synthesis, Biocompatibility, and Cytotoxicity. Int. J. Mol. Sci. 19, 3564. https://doi.org/10.3390/ijms19113564

Liao, C., Li, Y., Tjong, S.C., 2020. Polyetheretherketone and Its Composites for Bone Replacement and Regeneration. Polymers 12, 2858. https://doi.org/10.3390/polym12122858

Liesmäki, O., Plyusnin, A., Kulkova, J., Lassila, L.V.J., Vallittu, P.K., Moritz, N., 2019. Biostable glass fibre-reinforced dimethacrylate-based composites as potential candidates for fracture fixation

plates in toy-breed dogs: Mechanical testing and finite element analysis. J. Mech. Behav. Biomed. Mater. 96, 172–185. https://doi.org/10.1016/j.jmbbm.2019.04.016

Lin, A.S.P., Fechter, C.M., Magill, M., Wipf, F., Moore, T., Guldberg, R.E., 2016. The effect of contouring on fatigue resistance of three types of fracture fixation plates. J. Orthop. Surg. 11, 107. https://doi.org/10.1186/s13018-016-0439-1

Lin, A.Y., Kinsella, C.R., Rottgers, S.A., Smith, D.M., Grunwaldt, L.J., Cooper, G.M., Losee, J.E., 2012. Custom Porous Polyethylene Implants for Large-scale Pediatric Skull Reconstruction: Early Outcomes. J. Craniofac. Surg. 23, 67–70. https://doi.org/10.1097/SCS.0b013e318240c876

Lindfors, N.C., Heikkilä, J.T., Koski, I., Mattila, K., Aho, A.J., 2008. Bioactive glass and autogenous bone as bone graft substitutes in benign bone tumors. J. Biomed. Mater. Res. B Appl. Biomater. 90B, 131–136. https://doi.org/10.1002/jbm.b.31263

Liu, X., Feng, S., Wang, X., Qi, J., Lei, D., Li, Y., Bai, W., 2020. Tuning the mechanical properties and degradation properties of polydioxanone isothermal annealing. Turk. J. Chem. 44, 1430–1444. https://doi.org/10.3906/kim-2006-55

Losertová, M., Štamborská, M., Lapin, J., Mareš, V., 2016. Comparison of deformation behavior of 316L stainless steel and Ti6Al4V alloy applied in traumatology. Metalurgija 55, 667–670.

Madanat, R., Moritz, N., Vedel, E., Svedström, E., Aro, H.T., 2009. Radio-opaque bioactive glass markers for radiostereometric analysis. Acta Biomater. 5, 3497–3505. https://doi.org/10.1016/j.actbio.2009.05.038

Majola, A., Vainionpää, S., Rokkanen, P., Mikkola, H.-M., Törmälä, P., 1992. Absorbable self-reinforced polylactide (SR-PLA) composite rods for fracture fixation: strength and strength retention in the bone and subcutaneous tissue of rabbits. J. Mater. Sci. Mater. Med. 3, 43–47. https://doi.org/10.1007/BF00702943

Manchi, G., Brunnberg, M.M., Shahid, M., Al Aiyan, A., Chow, E., Brunnberg, L., Stein, S., 2017. Radial and ulnar fracture treatment with paraosseous clamp-cerclage stabilisation technique in 17 toy breed dogs. Vet. Rec. Open 4, e000194. https://doi.org/10.1136/vetreco-2016-000194

Manteghi, S., Mahboob, Z., Fawaz, Z., Bougherara, H., 2017. Investigation of the mechanical properties and failure modes of hybrid natural fiber composites for potential bone fracture fixation plates. J. Mech. Behav. Biomed. Mater. 65, 306–316. https://doi.org/10.1016/j.jmbbm.2016.08.035

Manzoor, F., Golbang, A., Jindal, S., Dixon, D., McIlhagger, A., Harkin-Jones, E., Crawford, D., Mancuso, E., 2021. 3D printed PEEK/HA composites for bone tissue engineering applications: Effect of material formulation on mechanical performance and bioactive potential. J. Mech. Behav. Biomed. Mater. 121, 104601. https://doi.org/10.1016/j.jmbbm.2021.104601

Mattheij, P., Gliesche, K., Feltin, D., 1998. Tailored fiber placement-mechanical properties and applications. J. Reinf. Plast. Compos. 17, 774–786. https://doi.org/10.1177/073168449801700901

Maurus, P.B., Kaeding, C.C., 2004. Bioabsorbable implant material review. Oper. Tech. Sports Med. 12, 158–160. https://doi.org/10.1053/j.otsm.2004.07.015

May, C., Yen, Y.-M., Nasreddine, A.Y., Hedequist, D., Hresko, M.T., Heyworth, B.E., 2013. Complications of plate fixation of femoral shaft fractures in children and adolescents. J. Child. Orthop. 7, 235–243. https://doi.org/10.1007/s11832-013-0496-5

McKibbin, B., 1978. The biology of fracture healing in long bones. J. Bone Joint Surg. Br. 60-B, 150–162. https://doi.org/10.1302/0301-620X.60B2.350882

Melchels, F.P.W., Feijen, J., Grijpma, D.W., 2009. A poly(d,l-lactide) resin for the preparation of tissue engineering scaffolds by stereolithography. Biomaterials 30, 3801–3809. https://doi.org/10.1016/j.biomaterials.2009.03.055

Melnikov, P., Teixeira, A.R., Malzac, A., Coelho, M. de B., 2009. Gallium-containing hydroxyapatite for potential use in orthopedics. Mater. Chem. Phys. 117, 86–90. https://doi.org/10.1016/j.matchemphys.2009.05.046

Meskinfam, M., 2017. Polymer scaffolds for bone regeneration, in: Tanzi, M., Fare, S. (Eds.), Characterization of Polymeric Biomaterials. Elsevier/Woodhead Publishing, pp. 441–475. https://doi.org/10.1016/B978-0-08-100737-2.00017-0

Meyer, F., Wardale, J., Best, S., Cameron, R., Rushton, N., Brooks, R., 2012. Effects of lactic acid and glycolic acid on human osteoblasts: A way to understand PLGA involvement in PLGA/calcium phosphate composite failure. J. Orthop. Res. 30, 864–871. https://doi.org/10.1002/jor.22019

Miao, S., Zhu, W., Castro, N.J., Nowicki, M., Zhou, X., Cui, H., Fisher, J.P., Zhang, L.G., 2016. 4D printing smart biomedical scaffolds with novel soybean oil epoxidized acrylate. Sci. Rep. 6, 27226. https://doi.org/10.1038/srep27226

Migonney, V. (Ed.), 2014. Biomaterials, Bioengineering and health science series. ISTE/Wiley, London : Hoboken.

Moen, R.A., Duncan, D.R., 1976. Cold work effects: a compilation of data for types 304 and 316 stainless steel (No. HEDL-TI-76005, 7180400). https://doi.org/10.2172/7180400

Mohseni, M., Hutmacher, D., Castro, N., 2018. Independent Evaluation of Medical-Grade Bioresorbable Filaments for Fused Deposition Modelling/Fused Filament Fabrication of Tissue Engineered Constructs. Polymers 10, 40. https://doi.org/10.3390/polym10010040

Moreau, M.F., Chappard, D., Lesourd, M., Montheard, J.P., Basle, M.F., 1998. Free radicals and side products released during methylmethacrylate polymerization are cytotoxic for osteoblastic cells. J. Biomed. Mater. Res. 40, 124–131. https://doi.org/10.1002/(SICI)1097-4636(199804)40:1<124::AID-JBM14>3.0.CO;2-O

Moritz, N., Mattila, R., Vallittu, P.K., 2016. Biomechanical evaluation of the load-bearing fiber-reinforced composite plates intended for the treatment of long bone fractures. Presented at the Advances in Functional Materials, South Korea.

Moritz, N., Strandberg, N., Zhao, D.S., Mattila, R., Paracchini, L., Vallittu, P.K., Aro, H.T., 2014. Mechanical properties and in vivo performance of load-bearing fiber-reinforced composite intramedullary nails with improved torsional strength. J. Mech. Behav. Biomed. Mater. 40, 127–139. https://doi.org/10.1016/j.jmbbm.2014.08.020

Nair, L.S., Laurencin, C.T., 2007. Biodegradable polymers as biomaterials. Prog. Polym. Sci. 32, 762–798. https://doi.org/10.1016/j.progpolymsci.2007.05.017

Nakamura, T., Yamamuro, T., Higashi, S., Kokubo, T., Itoo, S., 1985. A new glass-ceramic for bone replacement: Evaluation of its bonding to bone tissue. J. Biomed. Mater. Res. 19, 685–698. https://doi.org/10.1002/jbm.820190608

Narayan, R. (Ed.), 2019. Encyclopedia of biomedical engineering. Elsevier, Amsterdam.

Naujokat, H., Seitz, J.-M., Açil, A., Damm, T., Möller, I., Gülses, A., 2017. Osteosynthesis of a cranio-osteoplasty with a biodegradable magnesium plate system in miniature pigs. Acta Biomater. 62, 434–445. https://doi.org/10.1016/j.actbio.2017.08.031

Nauwynck, M., Bazrafkan, S., van Heteren, A.H., Beenhouwer, J.D., Sijbers, J., 2020. Ring Artifact Reduction in Sinogram Space Using Deep Learning. Presented at the The 6th International Conference on Image Formation in X-Ray Computed Tomography, Germany, pp. 486–489.

Navarro, M., Michiardi, A., Castaño, O., Planell, J.A., 2008. Biomaterials in orthopaedics. J. R. Soc. Interface 5, 1137–1158. https://doi.org/10.1098/rsif.2008.0151

Niiranen, H., Pyhältö, T., Rokkanen, P., Kellomäki, M., Törmälä, P., 2004. *In vitro* and *in vivo* behavior of self-reinforced bioabsorbable polymer and self-reinforced bioabsorbable polymer/bioactive glass composites: Self-Reinforced Bioabsorbable Polymer. J. Biomed. Mater. Res. A 69A, 699–708. https://doi.org/10.1002/jbm.a.30043

Omidi, M., Fatehinya, A., Farahani, M., Akbari, Z., Shahmoradi, S., Yazdian, F., Tahriri, M., Moharamzadeh, K., Tayebi, L., Vashaee, D., 2017. Characterization of biomaterials, in: Tayebi, L., Moharamzadeh, K. (Eds.), Biomaterials for Oral and Dental Tissue Engineering. Elsevier, pp. 97–115. https://doi.org/10.1016/B978-0-08-100961-1.00007-4

O'Neill, E., Awale, G., Daneshmandi, L., Umerah, O., Lo, K.W.-H., 2018. The roles of ions on bone regeneration. Drug Discov. Today 23, 879–890. https://doi.org/10.1016/j.drudis.2018.01.049

Osborn, E.J., Farnsworth, C.L., Doan, J.D., Edmonds, E.W., 2018. Bioabsorbable plating in the treatment of pediatric clavicle fractures: A biomechanical and clinical analysis. Clin. Biomech. 55, 94–99. https://doi.org/10.1016/j.clinbiomech.2018.04.017

Otsuki, B., Takemoto, M., Fujibayashi, S., Neo, M., Kokubo, T., Nakamura, T., 2006. Pore throat size and connectivity determine bone and tissue ingrowth into porous implants: Three-dimensional micro-CT based structural analyses of porous bioactive titanium implants. Biomaterials 27, 5892–5900. https://doi.org/10.1016/j.biomaterials.2006.08.013

Palierne, S., Mathon, D., Asimus, E., Concordet, D., Meynaud-Collard, P., Autefage, A., 2008. Segmentation of the canine population in different femoral morphological groups. Res. Vet. Sci. 85, 407–417. https://doi.org/10.1016/j.rvsc.2008.02.010

Peltola, M.J., Vallittu, P.K., Vuorinen, V., Aho, A.A.J., Puntala, A., Aitasalo, K.M.J., 2012. Novel composite implant in craniofacial bone reconstruction. Eur. Arch. Otorhinolaryngol. 269, 623–628. https://doi.org/10.1007/s00405-011-1607-x

Pemberton, D.J., Evans, P.D., Grant, A., McKibbin, B., 1994. Fractures of the distal femur in the elderly treated with a carbon fibre supracondylar plate. Injury 25, 317–321. https://doi.org/10.1016/0020-1383(94)90244-5

Pérez, M.A., Nuño, N., Madrala, A., García-Aznar, J.M., Doblaré, M., 2009. Computational modelling of bone cement polymerization: Temperature and residual stresses. Comput. Biol. Med. 39, 751–759. https://doi.org/10.1016/j.compbiomed.2009.06.002

Perren, S.M., 2002. Evolution of the internal fixation of long bone fractures. The scientific basis of biological internal fixation: choosing a new balance between stability and biology. J. Bone Joint Surg. Br. 84, 1093–1110. https://doi.org/10.1302/0301-620x.84b8.13752

Phan, K., Sgro, A., Maharaj, M.M., D'Urso, P., Mobbs, R.J., 2016. Application of a 3D custom printed patient specific spinal implant for C1/2 arthrodesis. J. Spine Surg. 2, 314–318. https://doi.org/10.21037/jss.2016.12.06

Pihlajamäki, H., Böstman, O., Hirvensalo, E., Törmälä, P., Rokkanen, P., 1992. Absorbable pins of self-reinforced poly-L-lactic acid for fixation of fractures and osteotomies. J. Bone Joint Surg. Br. 74-B, 853–857. https://doi.org/10.1302/0301-620X.74B6.1447246

Piitulainen, J.M., Mattila, R., Moritz, N., Vallittu, P.K., 2017. Load-Bearing Capacity and Fracture Behavior of Glass Fiber-Reinforced Composite Cranioplasty Implants. J. Appl. Biomater. Funct. Mater. 15, e356–e361. https://doi.org/10.5301/jabfm.5000375

Piitulainen, J.M., Posti, J.P., Aitasalo, K.M.J., Vuorinen, V., Vallittu, P.K., Serlo, W., 2015. Paediatric cranial defect reconstruction using bioactive fibre-reinforced composite implant: early outcomes. Acta Neurochir. (Wien) 157, 681–687. https://doi.org/10.1007/s00701-015-2363-2s

Piras, L., Cappellari, F., Peirone, B., Ferretti, A., 2011. Treatment of fractures of the distal radius and ulna in toy breed dogs with circular external skeletal fixation: a retrospective study. Vet. Comp. Orthop. Traumatol. 24, 228–235. https://doi.org/10.3415/VCOT-10-06-0089

Plyusnin, A., He, J., Elschner, C., Nakamura, M., Kulkova, J., Spickenheuer, A., Scheffler, C., Lassila, L.V.J., Moritz, N., 2021. A Polymer for Application as a Matrix Phase in a Concept of In Situ Curable Bioresorbable Bioactive Load-Bearing Continuous Fiber Reinforced Composite Fracture Fixation Plates. Molecules 26, 1256. https://doi.org/10.3390/molecules26051256

Plyusnin, A., Kulkova, J., Arthurs, G., Jalava, N., Uppstu, P., Moritz, N., 2020. Biological response to an experimental implant for tibial tuberosity advancement in dogs: A pre-clinical study. Res. Vet. Sci. 128, 183–196. https://doi.org/10.1016/j.rvsc.2019.12.003

Poitout, D.G. (Ed.), 2016. Biomechanics and Biomaterials in Orthopedics, 2nd ed. Springer, London. https://doi.org/10.1007/978-1-84882-664-9

Pountos, I., Giannoudis, P.V., 2018. Fracture Healing: Back to Basics and Latest Advances, in: Giannoudis, P.V. (Ed.), Fracture Reduction and Fixation Techniques. Springer International Publishing, Cham, pp. 3–17. https://doi.org/10.1007/978-3-319-68628-8_1

Prajapati, P., Sethuraman, R., Bector, S., Patel, J.R., 2013. Contact dermatitis due to methyl methacrylate: uncommon and unwanted entity for dentists. BMJ Case Rep. 2013, bcr-2013-200520. https://doi.org/10.1136/bcr-2013-200520

Quan, L., Zhang, Y., Dusad, A., Ren, K., Purdue, P.E., Goldring, S.R., Wang, D., 2016. The Evaluation of the Therapeutic Efficacy and Side Effects of a Macromolecular Dexamethasone Prodrug in the Collagen-Induced Arthritis Mouse Model. Pharm. Res. 33, 186–193. https://doi.org/10.1007/s11095-015-1776-1

Quinn, J., Joyner, C., Triffitt, J.T., Athanasou, N.A., 1992. Polymethylmethacrylate-induced inflammatory macrophages resorb bone. J. Bone Joint Surg. Br. 74, 7. https://doi.org/10.1302/0301-620X.74B5.1527108

Rahaman, M.N., Day, D.E., Sonny Bal, B., Fu, Q., Jung, S.B., Bonewald, L.F., Tomsia, A.P., 2011. Bioactive glass in tissue engineering. Acta Biomater. 7, 2355–2373. https://doi.org/10.1016/j.actbio.2011.03.016

Rajasekharan, A.K., Gyllensten, C., Blomstrand, E., Liebi, M., Andersson, M., 2020. Tough Ordered Mesoporous Elastomeric Biomaterials Formed at Ambient Conditions. ACS Nano 14, 241–254. https://doi.org/10.1021/acsnano.9b01924

Ramot, Y., Haim-Zada, M., Domb, A.J., Nyska, A., 2016. Biocompatibility and safety of PLA and its copolymers. Adv. Drug Deliv. Rev. 107, 153–162. https://doi.org/10.1016/j.addr.2016.03.012

Ratner, B.D., Hoffman, A.S., Schoen, F.J., Lemons, J.E. (Eds.), 2012. Biomaterials Science: An introduction to materials in medicine, 3rd ed. Elsevier/Academic Press.

Regmi, P., Nelson, N., Haut, R.C., Orth, M.W., Karcher, D.M., 2017. Influence of age and housing systems on properties of tibia and humerus of Lohmann White hens: Bone properties of laying hens in commercial housing systems. Poult. Sci. 96, 3755–3762. https://doi.org/10.3382/ps/pex194

Reznikov, N., Buss, D.J., Provencher, B., McKee, M.D., Piché, N., 2020. Deep learning for 3D imaging and image analysis in biomineralization research. J. Struct. Biol. 212, 107598. https://doi.org/10.1016/j.jsb.2020.107598

Rihaczek, G., Klammer, M., Başnak, O., Petrš, J., Grisin, B., Dahy, H., Carosella, S., Middendorf, P., 2020. Curved Foldable Tailored Fiber Reinforcements for Moldless Customized Bio-Composite Structures. Proof of Concept: Biomimetic NFRP Stools. Polymers 12, 2000. https://doi.org/10.3390/polym12092000

Rocchi, M., Affatato, S., Falasca, G., Viceconti, M., 2007. Thermomechanical analysis of ultra-high molecular weight polyethylene-metal hip prostheses. Proc. Inst. Mech. Eng. [H] 221, 561–568. https://doi.org/10.1243/09544119JEIM137

Roeder, R.K., 2013. Mechanical Characterization of Biomaterials, in: Bandyopadhyay, A., Bose, S. (Eds.), Characterization of Biomaterials. Elsevier, pp. 49–104. https://doi.org/10.1016/B978-0-12-415800-9.00003-6

Rosenhain, S., Magnuska, Z.A., Yamoah, G.G., Rawashdeh, W.A., Kiessling, F., Gremse, F., 2018. A preclinical micro-computed tomography database including 3D whole body organ segmentations. Sci. Data 5, 180294. https://doi.org/10.1038/sdata.2018.294

Rowe-Guthrie, K.M., Markel, M.D., Bleedorn, J.A., 2015. Mechanical Evaluation of Locking, Nonlocking, and Hybrid Plating Constructs Using a Locking Compression Plate in a Canine Synthetic Bone Model: Hybrid Plating in a Canine Fracture Model. Vet. Surg. 44, 838–842. https://doi.org/10.1111/vsu.12368

Sacks, M., D'Amore, A., Hobson, C., 2012. Finite element -analysis in -biomechanics, in: Ratner, B.D., Hoffman, A.S., Schoen, F.J., Lemons, J.E. (Eds.), Biomaterials Science: An Introduction to Materials in Medicine. Elsevier/Academic Press.

Saikku-Bäckström, A., Räihä, J.E., Välimaa, T., Tulamo, R.-M., 2005. Repair of Radial Fractures in Toy Breed Dogs with Self-Reinforced Biodegradable Bone Plates, Metal Screws, and Light-Weight External Coaptation. Vet. Surg. 34, 11–17. https://doi.org/10.1111/j.1532-950X.2005.00003.x

Sakai, A., Oshige, T., Zenke, Y., Menuki, K., Murai, T., Nakamura, T., 2012. Mechanical Comparison of Novel Bioabsorbable Plates with Titanium Plates and Small-Series Clinical Comparisons for Metacarpal Fractures. J. Bone Joint Surg. Am. 94, 1597–1604. https://doi.org/10.2106/JBJS.J.01673

Salmon, P., 2020. Application of Bone Morphometry and Densitometry by X-Ray Micro-CT to Bone Disease Models and Phenotypes, in: Orhan, K. (Ed.), Micro-Computed Tomography (Micro-CT) in Medicine and Engineering. Springer International Publishing, Cham.

Sanivada, U.K., Mármol, G., Brito, F.P., Fangueiro, R., 2020. PLA Composites Reinforced with Flax and Jute Fibers—A Review of Recent Trends, Processing Parameters and Mechanical Properties. Polymers 12, 2373. https://doi.org/10.3390/polym12102373

Sawhney, A.S., Pathak, C.P., Hubbell, J.A., 1993. Bioerodible hydrogels based on photopolymerized poly(ethylene glycol)-co-poly(.alpha.-hydroxy acid) diacrylate macromers. Macromolecules 26, 581–587. https://doi.org/10.1021/ma00056a005

Scholz, M.-S., Blanchfield, J.P., Bloom, L.D., Coburn, B.H., Elkington, M., Fuller, J.D., Gilbert, M.E., Muflahi, S.A., Pernice, M.F., Rae, S.I., Trevarthen, J.A., White, S.C., Weaver, P.M., Bond, I.P., 2011. The use of composite materials in modern orthopaedic medicine and prosthetic devices: A review. Compos. Sci. Technol. 71, 1791–1803. https://doi.org/10.1016/j.compscitech.2011.08.017

Schuppli, C.A., Fraser, D., 2005. The Interpretation and Application of the Three Rs by Animal Ethics Committee Members. Altern. Lab. Anim. 33, 487–500. https://doi.org/10.1177/026119290503300511

Schwartz, Z., Raz, P., Zhao, G., Barak, Y., Tauber, M., Yao, H., Boyan, B.D., 2008. Effect of Micrometer-Scale Roughness of the Surface of Ti6Al4V Pedicle Screws in Vitro and in Vivo: J. Bone Joint Surg. Am. 90, 2485–2498. https://doi.org/10.2106/JBJS.G.00499

Scott, G. (Ed.), 2002. Degradable Polymers. Principles and Applications, 2nd ed. Springer Netherlands, Dordrecht. https://doi.org/10.1007/978-94-017-1217-0

Seitz, S., Priemel, M., Zustin, J., Beil, F.T., Semler, J., Minne, H., Schinke, T., Amling, M., 2009. Paget's Disease of Bone: Histologic Analysis of 754 Patients. J. Bone Miner. Res. 24, 62–69. https://doi.org/10.1359/jbmr.080907

Shahar, R., Milgram, J., 2005. Morphometric and anatomic study of the forelimb of the dog. J. Morphol. 263, 107–117. https://doi.org/10.1002/jmor.10295

Shahar, R., Milgram, J., 2001. Morphometric and anatomic study of the hind limb of a dog. Am. J. Vet. Res. 62, 928–933. https://doi.org/10.2460/ajvr.2001.62.928

Shen, L., Zhao, W., Xing, L., 2019. Harnessing the power of deep learning for volumetric CT imaging with single or limited number of projections, in: Angelini, E.D., Landman, B.A. (Eds.), Proceedings of SPIE, Physics of Medical Imaging. Presented at the SPIE Medical Imaging, SPIE, San Diego, US, p. 1094826. https://doi.org/10.1117/12.2513032

Shen, S.C., Peña Fernández, M., Tozzi, G., Buehler, M.J., 2021. Deep learning approach to assess damage mechanics of bone tissue. J. Mech. Behav. Biomed. Mater. 123, 104761. https://doi.org/10.1016/j.jmbbm.2021.104761

Sideridou, I., Achilias, D.S., Kyrikou, E., 2004. Thermal expansion characteristics of light-cured dental resins and resin composites. Biomaterials 25, 3087–3097. https://doi.org/10.1016/j.biomaterials.2003.09.078

Sideridou, I., Tserki, V., Papanastasiou, G., 2003. Study of water sorption, solubility and modulus of elasticity of light-cured dimethacrylate-based dental resins. Biomaterials 24, 655–665. https://doi.org/10.1016/S0142-9612(02)00380-0

Sobajima, A., Okihara, T., Moriyama, S., Nishimura, N., Osawa, T., Miyamae, K., Haniu, H., Aoki, K., Tanaka, M., Usui, Y., Sako, K., Kato, H., Saito, N., 2020. Multiwall Carbon Nanotube Composites as Artificial Joint Materials. ACS Biomater. Sci. Eng. 6, 7032–7040. https://doi.org/10.1021/acsbiomaterials.0c00916

Sod, G.A., Hubert, J.D., Martin, G.S., Gill, M.S., 2005. An In Vitro Biomechanical Comparison of a Prototype Equine Metacarpal Dynamic Compression Plate Fixation with Double Dynamic

Compression Plate Fixation of Osteotomized Equine Third Metacarpal Bones. Vet. Surg. 34, 594–603. https://doi.org/10.1111/j.1532-950X.2005.00093.x

Spencer, R.F., Bullock, R., Cooper, K., Norman, R.J., Becker, P.J., 1990. The effect of a brain lesion on bone healing. J. Orthop. Res. 8, 646–650. https://doi.org/10.1002/jor.1100080505

Spicer, P.P., Kretlow, J.D., Young, S., Jansen, J.A., Kasper, F.K., Mikos, A.G., 2012. Evaluation of bone regeneration using the rat critical size calvarial defect. Nat. Protoc. 7, 1918–1929. https://doi.org/10.1038/nprot.2012.113

Spickenheuer, A., Schulz, M., Gliesche, K., Heinrich, G., 2008. Using tailored fibre placement technology for stress adapted design of composite structures. Plast. Rubber Compos. 37, 227–232. https://doi.org/10.1179/174328908X309448

Staffa, G., Barbanera, A., Faiola, A., Fricia, M., Limoni, P., Mottaran, R., Zanotti, B., Stefini, R., 2012. Custom made bioceramic implants in complex and large cranial reconstruction: A two-year follow-up. J. Cranio-Maxillofac. Surg. 40, e65–e70. https://doi.org/10.1016/j.jcms.2011.04.014

Steinberg, E., Rath, E., Shlaifer, A., Chechik, O., Maman, E., Salai, M., 2013. Carbon fiber reinforced PEEK Optima--a composite material biomechanical properties and wear/debris characteristics of CF-PEEK composites for orthopedic trauma implants. J. Mech. Behav. Biomed. Mater. 17, 221–228. https://doi.org/10.1016/j.jmbbm.2012.09.013

Stoor, P., Frantzen, J., 2017. Influence of bioactive glass S53P4 granules and putty on osteomyelitis associated bacteria in vitro. Biomed. Glas. 3, 79–85. https://doi.org/10.1515/bglass-2017-0007

Storey, R.F., Warren, S.C., Allison, C.J., Wiggins, J.S., Puckett, A.D., 1993. Synthesis of bioabsorbable networks from methacrylate-endcapped polyesters. Polymer 34, 4365–4372. https://doi.org/10.1016/0032-3861(93)90203-M

Su, Y., Fu, J., Lee, W., Du, S., Qin, Y.-X., Zheng, Y., Wang, Y., Zhu, D., 2021. Improved mechanical, degradation, and biological performances of Zn–Fe alloys as bioresorbable implants. Bioact. Mater. 17, 334–343. https://doi.org/10.1016/j.bioactmat.2021.12.030

Sudheer, M., Pradyoth, K.R., Somayaji, S., 2015. Analytical and Numerical Validation of Epoxy/Glass Structural Composites for Elastic Models. Am. J. Mater. Sci. 5, 162–168. https://doi.org/10.5923/c.materials.201502.32

Surmenev, R.A., Surmeneva, M.A., Ivanova, A.A., 2014. Significance of calcium phosphate coatings for the enhancement of new bone osteogenesis – A review. Acta Biomater. 10, 557–579. https://doi.org/10.1016/j.actbio.2013.10.036

Taira, M., Urabe, H., Hirose, T., Wakasa, K., Yamaki, M., 1988. Analysis of Photo-initiators in Visible-light-cured Dental Composite Resins. J. Dent. Res. 67, 24–28. https://doi.org/10.1177/00220345880670010401

Tamada, J.A., Langer, R., 1993. Erosion kinetics of hydrolytically degradable polymers. Proc. Natl. Acad. Sci. 90, 552–556. https://doi.org/10.1073/pnas.90.2.552

Tan, K.H., Chua, C.K., Leong, K.F., Cheah, C.M., Cheang, P., Abu Bakar, M.S., Cha, S.W., 2003. Scaffold development using selective laser sintering of polyetheretherketone–hydroxyapatite biocomposite blends. Biomaterials 24, 3115–3123. https://doi.org/10.1016/S0142-9612(03)00131-5

Tan, K.H., Chua, C.K., Leong, K.F., Naing, M.W., Cheah, C.M., 2005. Fabrication and characterization of three-dimensional poly(ether-ether-ketone)/-hydroxyapatite biocomposite scaffolds using laser sintering. Proc. Inst. Mech. Eng. [H] 219, 183–194. https://doi.org/10.1243/095441105X9345

Tappa, K., Jammalamadaka, U., 2018. Novel Biomaterials Used in Medical 3D Printing Techniques. J. Funct. Biomater. 9, 17. https://doi.org/10.3390/jfb9010017

Tayton, K., Bradley, J., 1983. How stiff should semi-rigid fixation of the human tibia be? A clue to the answer. J. Bone Joint Surg. Br. 65, 312–315. https://doi.org/10.1302/0301-620X.65B3.6841402

Tayton, K., Johnson-Nurse, C., McKibbin, B., Bradley, J., Hastings, G., 1982. The use of semi-rigid carbon-fibre-reinforced plastic plates for fixation of human fractures. Results of preliminary trials. J. Bone Joint Surg. Br. 64, 105–111. https://doi.org/10.1302/0301-620X.64B1.7040407

Timercan, A., Brailovski, V., Petit, Y., Lussier, B., Séguin, B., 2019. Personalized 3D-printed endoprostheses for limb sparing in dogs: Modeling and in vitro testing. Med. Eng. Phys. 71, 17–29. https://doi.org/10.1016/j.medengphy.2019.07.005

Tivesten, Å., Movérare-Skrtic, S., Chagin, A., Venken, K., Salmon, P., Vanderschueren, D., Sävendahl, L., Holmäng, A., Ohlsson, C., 2004. Additive Protective Effects of Estrogen and Androgen Treatment on Trabecular Bone in Ovariectomized Rats. J. Bone Miner. Res. 19, 1833–1839. https://doi.org/10.1359/JBMR.040819

Törmälä, P., 1992. Biodegradable self-reinforced composite materials; Manufacturing structure and mechanical properties. Clin. Mater. 10, 29–34. https://doi.org/10.1016/0267-6605(92)90081-4

Torstrick, F.B., Klosterhoff, B.S., Westerlund, L.E., Foley, K.T., Gochuico, J., Lee, C.S.D., Gall, K., Safranski, D.L., 2018. Impaction durability of porous polyether-ether-ketone (PEEK) and titanium-coated PEEK interbody fusion devices. Spine J. 18, 857–865. https://doi.org/10.1016/j.spinee.2018.01.003

Turunen, T., Peltola, J., Yli-Urpo, A., Happonen, R.-P., 2004. Bioactive glass granules as a bone adjunctive material in maxillary sinus floor augmentation. Clin. Oral Implants Res. 15, 135–141. https://doi.org/10.1111/j.1600-0501.2004.00989.x

Tuusa, S.M.-R., Peltola, M.J., Tirri, T., Lassila, L.V.J., Vallittu, P.K., 2007. Frontal bone defect repair with experimental glass-fiber-reinforced composite with bioactive glass granule coating. J. Biomed. Mater. Res. B Appl. Biomater. 82B, 149–155. https://doi.org/10.1002/jbm.b.30716

Tuusa, S.M.-R., Peltola, M.J., Tirri, T., Puska, M.A., Röyttä, M., Aho, H., Sandholm, J., Lassila, L.V.J., Vallittu, P.K., 2008. Reconstruction of critical size calvarial bone defects in rabbits with glass–fiber-reinforced composite with bioactive glass granule coating. J. Biomed. Mater. Res. B Appl. Biomater. 84B, 510–519. https://doi.org/10.1002/jbm.b.30898

Tuusa, S.M.-R., Puska, M.A., Lassila, L.V.J., Vallittu, P.K., 2005. Residual monomers released from glass-fibre-reinforced composite photopolymerised in contact with bone and blood. J. Mater. Sci. Mater. Med. 16, 15–20. https://doi.org/10.1007/s10856-005-6441-5

Uchida, S., Utsunomiya, H., Taketa, T., Sakoda, S., Hatakeyama, A., Nakamura, T., Sakai, A., 2015. Arthroscopic Fragment Fixation Using Hydroxyapatite/Poly-L-Lactate Acid Thread Pins for Treating Elbow Osteochondritis Dissecans. Am. J. Sports Med. 43, 1057–1065. https://doi.org/10.1177/0363546515570871

Uhthoff, H.K., Dubuc, F.L., 1971. Bone Structure Changes in the Dog Under Rigid Internal Fixation. Clin. Orthop. 81, 165–170. https://doi.org/10.1097/00003086-197111000-00026

Uhthoff, H.K., Poitras, P., Backman, D.S., 2006. Internal plate fixation of fractures: short history and recent developments. J. Orthop. Sci. 11, 118–126. https://doi.org/10.1007/s00776-005-0984-7

Unterhofer, C., Wipplinger, C., Verius, M., Recheis, W., Thomé, C., Ortler, M., 2017. Reconstruction of large cranial defects with poly-methyl-methacrylate (PMMA) using a rapid prototyping model and a new technique for intraoperative implant modeling. Neurol. Neurochir. Pol. 51, 214–220. https://doi.org/10.1016/j.pjnns.2017.02.007

Utzschneider, S., Becker, F., Grupp, T.M., Sievers, B., Paulus, A., Gottschalk, O., Jansson, V., 2010. Inflammatory response against different carbon fiber-reinforced PEEK wear particles compared with UHMWPE in vivo. Acta Biomater. 6, 4296–4304. https://doi.org/10.1016/j.actbio.2010.06.002

Vainionpää, S., Kilpikari, J., Laiho, J., Helevirta, P., Rokkanen, P., Törmälä, P., 1987. Strength and strength retention in vitro, of absorbable, self-reinforced polyglycolide (PGA) rods for fracture fixation. Biomaterials 8, 46–48. https://doi.org/10.1016/0142-9612(87)90028-7

Vallittu, P.K., 2017. Bioactive glass-containing cranial implants: an overview. J. Mater. Sci. 52, 8772–8784. https://doi.org/10.1007/s10853-017-0888-x

Vallittu, P.K., Miettinen, V., Alakuijala, P., 1995. Residual monomer content and its release into water from denture base materials. Dent. Mater. 11, 338–342. https://doi.org/10.1016/0109-5641(95)80031-X

van der Meulen, M.C.H., Morgan, T.G., Yang, X., Baldini, T.H., Myers, E.R., Wright, T.M., Bostrom, M.P.G., 2006. Cancellous bone adaptation to in vivo loading in a rabbit model. Bone 38, 871–877. https://doi.org/10.1016/j.bone.2005.11.026

van der Meulen, M.C.H., Yang, X., Morgan, T.G., Bostrom, M.P.G., 2009. The Effects of Loading on Cancellous Bone in the Rabbit. Clin. Orthop. 467, 2000–2006. https://doi.org/10.1007/s11999-009-0897-4

van Gestel, N.A.P., Schuiringa, G.H., Hennissen, J.H.P.H., Delsing, A.C.A., Ito, K., van Rietbergen, B., Arts, J.J., Hofmann, S., 2019. Resorption of the calcium phosphate layer on S53P4 bioactive glass by osteoclasts. J. Mater. Sci. Mater. Med. 30, 94. https://doi.org/10.1007/s10856-019-6295-x

Variola, F., Yi, J.-H., Richert, L., Wuest, J.D., Rosei, F., Nanci, A., 2008. Tailoring the surface properties of Ti6Al4V by controlled chemical oxidation. Biomaterials 29, 1285–1298. https://doi.org/10.1016/j.biomaterials.2007.11.040

Veiranto, M., Törmälä, P., Suokas, E., 2002. In vitro mechanical and drug release properties of bioabsorbable ciprofloxacin containing and neat self-reinforced P(L/DL)LA 70/30 fixation screws. J. Mater. Sci. Mater. Med. 13, 1259–1263. https://doi.org/10.1023/a:1021187331458

Viateau, V., Guillemin, G., Yang, Y.C., Bensaid, W., Reviron, T., Oudina, K., Meunier, A., Sedel, L., Petite, H., 2004. A technique for creating critical-size defects in the metatarsus of sheep for use in investigation of healing of long-bone defects. Am. J. Vet. Res. 65, 1653–1657. https://doi.org/10.2460/ajvr.2004.65.1653

Voor, M.J., Arts, J.J.C., Klein, S.A., Walschot, L.H.B., Verdonschot, N., Buma, P., 2004. Is hydroxyapatite cement an alternative for allograft bone chips in bone grafting procedures? A mechanical and histological study in a rabbit cancellous bone defect model. J. Biomed. Mater. Res. B Appl. Biomater. 71, 398–407. https://doi.org/10.1002/jbm.b.30109

Wagner, W.R., Sakiyama-Elbert, S.E., Zhang, G., Yaszemski, M.J. (Eds.), 2020. Biomaterials Science: An Introduction to Materials in Medicine, 4th ed. Elsevier/Academic Press.

Waizy, H., Weizbauer, A., Modrejewski, C., Witte, F., Windhagen, H., Lucas, A., Kieke, M., Denkena, B., Behrens, P., Meyer-Lindenberg, A., Bach, F.-W., Thorey, F., 2012. In vitro corrosion of ZEK100 plates in Hank's Balanced Salt Solution. Biomed. Eng. OnLine 11, 12. https://doi.org/10.1186/1475-925X-11-12

Wang, A., Lin, R., Polineni, V.K., Essner, A., Stark, C., Dumbleton, J.H., 1998. Carbon fiber reinforced polyether ether ketone composite as a bearing surface for total hip replacement. Tribol. Int. 31, 661–667. https://doi.org/10.1016/S0301-679X(98)00088-7

Wang, B., Zhang, K., Zhou, C., Ren, M., Gu, Y., Li, T., 2019. Engineering the mechanical properties of CNT/PEEK nanocomposites. RSC Adv. 9, 12836–12845. https://doi.org/10.1039/C9RA01212E

Wang, H., Chu, P.K., 2013. Surface Characterization of Biomaterials, in: Bandyopadhyay, A., Bose, S. (Eds.), Characterization of Biomaterials. Elsevier, pp. 105–174. https://doi.org/10.1016/B978-0-12-415800-9.00004-8

Wang, H., Ji, J., Zhang, W., Zhang, Y., Jiang, J., Wu, Z., Pu, S., Chu, P., 2009. Biocompatibility and bioactivity of plasma-treated biodegradable poly(butylene succinate). Acta Biomater. 5, 279–287. https://doi.org/10.1016/j.actbio.2008.07.017

Wang, Y., Wang, K., Li, X., Wei, Q., Chai, W., Wang, S., Che, Y., Lu, T., Zhang, B., 2017. 3D fabrication and characterization of phosphoric acid scaffold with a HA/β-TCP weight ratio of 60:40 for bone tissue engineering applications. PLOS ONE 12, e0174870. https://doi.org/10.1371/journal.pone.0174870

Wilson, J., Pigott, G.H., Schoen, F.J., Hench, L.L., 1981. Toxicology and biocompatibility of bioglasses. J. Biomed. Mater. Res. 15, 805–817. https://doi.org/10.1002/jbm.820150605

Wong, K.V., Hernandez, A., 2012. A Review of Additive Manufacturing. ISRN Mech. Eng. 2012, 1–10. https://doi.org/10.5402/2012/208760

Woo, S.L.-Y., Lothringer, K.S., Akeson, W.H., Coutts, R.D., Woo, Y.K., Simon, B.R., Gomez, M.A., 1983. Less rigid internal fixation plates: Historical perspectives and new concepts. J. Orthop. Res. 1, 431–449. https://doi.org/10.1002/jor.1100010412

Woodard, L.N., Grunlan, M.A., 2018. Hydrolytic Degradation and Erosion of Polyester Biomaterials. ACS Macro Lett. 7, 976–982. https://doi.org/10.1021/acsmacrolett.8b00424

Wu, C.-H., Lin, Y.-S., Liu, Y.-S., Lin, C.-L., 2017. Biomechanical evaluation of a novel hybrid reconstruction plate for mandible segmental defects: A finite element analysis and fatigue testing. J. Cranio-Maxillofac. Surg. 45, 1671–1680. https://doi.org/10.1016/j.jcms.2017.07.010

Wu, X., Wang, Z., Li, H., Li, Y., Wang, H., Tian, W., 2019. Biomechanical evaluation of osteoporotic fracture: Metal fixation versus absorbable fixation in Sawbones models. Injury 50, 1272–1276. https://doi.org/10.1016/j.injury.2019.05.023

Wypych, G., 2016. Handbook of polymers, 2nd ed. ChemTec Publishing, Toronto.

Xiao, P., Haque, E., Zhang, T., Dong, X.N., Huang, Y., Wang, X., 2021. Can DXA image-based deep learning model predict the anisotropic elastic behavior of trabecular bone? J. Mech. Behav. Biomed. Mater. 124, 104834. https://doi.org/10.1016/j.jmbbm.2021.104834

Xu, L., Qin, H., Tan, J., Cheng, Z., Luo, X., Tan, H., Huang, W., 2021. Clinical study of 3D printed personalized prosthesis in the treatment of bone defect after pelvic tumor resection. J. Orthop. Transl. 29, 163–169. https://doi.org/10.1016/j.jot.2021.05.007

Yamamuro, T., 2016. Bioceramics, in: Poitout, D.G. (Ed.), Biomechanics and Biomaterials in Orthopedics. Springer, London, pp. 21–33. https://doi.org/10.1007/978-1-84882-664-9_3

Yang, H.Y., Yang, S.F., Chi, X.P., Evans, J.R.G., Thompson, I., Cook, R.J., Robinson, P., 2008. Sintering behaviour of calcium phosphate filaments for use as hard tissue scaffolds. J. Eur. Ceram. Soc. 28, 159–167. https://doi.org/10.1016/j.jeurceramsoc.2007.04.013

Yang, P.-F., Sanno, M., Ganse, B., Koy, T., Brüggemann, G.-P., Müller, L.P., Rittweger, J., 2014. Torsion and Antero-Posterior Bending in the In Vivo Human Tibia Loading Regimes during Walking and Running. PLOS ONE 9, e94525. https://doi.org/10.1371/journal.pone.0094525

Ylänen, H.O., 2008. Clinical application of bioactive glasses, in: Kokubo, T. (Ed.), Bioceramics and Their Clinical Applications. Elsevier/Woodhead Publishing, pp. 571–582. https://doi.org/10.1533/9781845694227.3.571

Yoshida, K., Greener, E.H., 1994. Effect of photoinitiator on degree of conversion of unfilled light-cured resin. J. Dent. 22, 296–299. https://doi.org/10.1016/0300-5712(94)90064-7

Yu, X., Tang, X., Gohil, S.V., Laurencin, C.T., 2015. Biomaterials for Bone Regenerative Engineering. Adv. Healthc. Mater. 4, 1268–1285. https://doi.org/10.1002/adhm.201400760

Yuan, B., Cheng, Q., Zhao, R., Zhu, X., Yang, Xiao, Yang, Xi, Zhang, K., Song, Y., Zhang, X., 2018. Comparison of osteointegration property between PEKK and PEEK: Effects of surface structure and chemistry. Biomaterials 170, 116–126. https://doi.org/10.1016/j.biomaterials.2018.04.014

Zhang, D., Leppäranta, O., Munukka, E., Ylänen, H., Viljanen, M.K., Eerola, E., Hupa, M., Hupa, L., 2010. Antibacterial effects and dissolution behavior of six bioactive glasses. J. Biomed. Mater. Res. A 93, 475–483. https://doi.org/10.1002/jbm.a.32564

Zhang, K., Qian, Y., Wang, H., Fan, L., Huang, C., Yin, A., Mo, X., 2010. Genipin-crosslinked silk fibroin/hydroxybutyl chitosan nanofibrous scaffolds for tissue-engineering application. J. Biomed. Mater. Res. A 95A, 870–881. https://doi.org/10.1002/jbm.a.32895

Zhang, Y., 2012. Clinical epidemiology of orthopedic trauma. Thieme, Stuttgart.

Zhao, D.S., Moritz, N., Laurila, P., Mattila, R., Lassila, L.V.J., Strandberg, N., Mäntylä, T., Vallittu, P.K., Aro, H.T., 2009. Development of a multi-component fiber-reinforced composite implant for load-sharing conditions. Med. Eng. Phys. 31, 461–469. https://doi.org/10.1016/j.medengphy.2008.11.006

Zheng, H., Bai, Y., Shih, M.-S., Hoffmann, C., Peters, F., Waldner, C., Hu, W.-D., 2014. Effect of a b-TCP collagen composite bone substitute on healing of drilled bone voids in the distal femoral condyle of rabbits. J. Biomed. Mater. Res. B Appl. Biomater. 102, 8. https://doi.org/10.1002/jbm.b.33016

Zheng, J., Chen, X., Jiang, W., Zhang, S., Chen, M., Yang, C., 2019. An innovative total temporomandibular joint prosthesis with customized design and 3D printing additive fabrication: a prospective clinical study. J. Transl. Med. 17, 4. https://doi.org/10.1186/s12967-018-1759-1

Zhou, H., Lawrence, J.G., Bhaduri, S.B., 2012. Fabrication aspects of PLA-CaP/PLGA-CaP composites for orthopedic applications: A review. Acta Biomater. 8, 1999–2016. https://doi.org/10.1016/j.actbio.2012.01.031

Zimina, A., Senatov, F., Choudhary, R., Kolesnikov, E., Anisimova, N., Kiselevskiy, M., Orlova, P., Strukova, N., Generalova, M., Manskikh, V., Gromov, A., Karyagina, A., 2020. Biocompatibility and Physico-Chemical Properties of Highly Porous PLA/HA Scaffolds for Bone Reconstruction. Polymers 12, 2938. https://doi.org/10.3390/polym12122938

Zoccali, C., Soriani, A., Rossi, B., Salducca, N., Biagini, R., 2016. The Carbofix™ "Piccolo Proximal femur nail": A new perspective for treating proximal femur lesion. A technique report. J. Orthop. 13, 343–346. https://doi.org/10.1016/j.jor.2016.07.001

TURUN
YLIOPISTO
UNIVERSITY
OF TURKU

Painosalama, Turku, Finland 2022

ISBN 978-951-29-8951-5 (Print)
ISBN 978-951-29-8952-2 (PDF)
ISSN 0355-9483 (Print)
ISSN 2343-3213 (Online)